



Cite this: *Chem. Sci.*, 2025, **16**, 13966

All publication charges for this article have been paid for by the Royal Society of Chemistry

## Photoelectrochemical valorisation of organic waste for the cogeneration of solar fuels and value-added chemicals†

Fitri Nur Indah Sari,<sup>a</sup> Ping-Chang Chuang,<sup>b</sup> Shih-Ching Huang,<sup>ID</sup><sup>a</sup> Chia-Yu Lin<sup>ID</sup>\*<sup>ac</sup> and Yi-Hsuan Lai<sup>ID</sup>\*<sup>bc</sup>

Rapid industrialisation has resulted in severe greenhouse gas emissions through extensive fossil fuel extraction and an increasing volume of solid waste disposal. This perspective review examines the photoelectrochemical (PEC) valorisation of organic waste as a promising solution for addressing the energy crisis and environmental pollution. The current stage of PEC organic valorisation has yet to meet industrial requirements, hindered by its relatively low efficiency, limited robustness, and poor scalability compared to conventional technologies. A better understanding of the working principle of the PEC reaction mechanism, the properties of state-of-the-art photoelectrodes, and the organic waste pre-treatment process is required to pave the path toward practical implementation. In this perspective review, we demonstrate that the strategies employed in the design of photoanodes, including doping, heterojunction formation, co-catalyst modification, nanostructuring, and crystal facet engineering, have different effects on activity, selectivity, and stability. In addition to the hydrogen evolution reaction, selected organic reduction reactions for the synthesis of value-added chemicals in a PEC cell are also discussed, followed by recent progress on integrated PEC cells and their practical assessment for solar fuel and value-added chemical production. Since stability and scalability are also essential parameters beyond efficiency for assessing the techno-economic feasibility of a PEC organic valorisation system, we additionally addressed stability, scalability and the compatibility of photoelectrodes in organic waste valorisation. Finally, conclusions and future

Received 30th April 2025  
Accepted 30th June 2025

DOI: 10.1039/d5sc03146j  
[rsc.li/chemical-science](http://rsc.li/chemical-science)

<sup>a</sup>Department of Chemical Engineering, National Cheng Kung University, No. 1, University Road, Tainan City 701, Taiwan. E-mail: cyl44@mail.ncku.edu.tw

<sup>b</sup>Department of Materials Science and Engineering, National Cheng Kung University, No. 1, University Road, Tainan City 701, Taiwan. E-mail: yhlai@g.s.ncku.edu.tw

<sup>c</sup>Hierarchical Green-Energy Materials (Hi-GEM) Research Center, National Cheng Kung University, Tainan City 70101, Taiwan

† Electronic supplementary information (ESI) available. See DOI: <https://doi.org/10.1039/d5sc03146j>



Fitri Nur Indah Sari

Fitri Nur Indah Sari received her PhD degree from the Department of Materials Science and Engineering at National Cheng Kung University in 2018. She is currently a postdoctoral fellow at the Department of Chemical Engineering, National Cheng Kung University. Her research interests focus on the design and synthesis of advanced organic and inorganic nanomaterials, including graphene and its composite,  $\text{MoS}_2$ , ceramics, and high entropy material. These materials have been explored for functional applications, especially in energy conversion, energy storage, and environmental remediation.



Ping-Chang Chuang

Ping-Chang Chuang obtained a BS in Chemical and Materials Engineering from the National University of Kaohsiung in 2018, followed by an MS in Materials and Optoelectronic Science from National Sun Yat-Sen University in 2020. Since then, he has been working towards his PhD in the Department of Materials Science and Engineering at National Cheng-Kung University, mentored by Prof. Yi-Hsuan Lai. His current research focuses on electrocatalytic biomass valorisation and artificial photosynthesis.



perspectives on feasible strategies for PEC valorisation are discussed. We hope this review will serve as a helpful guide in designing effective, robust, and scalable PEC organic waste valorisation systems, making it a viable technology for real-world applications.

## 1. Introduction

Meeting the energy demand sustainably to alleviate greenhouse gas (GHG) emissions has reached a global consensus.<sup>1–3</sup> Over the past few centuries, overdependence on fossil fuels has resulted in irreparable climate change due to the greenhouse effects. On the other hand, rapid technological development has led to a significant increase in the generation of solid waste, such as biomass and plastics, which also contribute to non-negligible GHG emissions.<sup>4,5</sup> In addition, the predominant waste processing methodologies, landfilling and incineration, have caused severe environmental pollution and the loss of valuable resources. The exploration of technologies that align



Shih-Ching Huang

catalytic materials for sustainable applications.

*Shih-Ching Huang received her BSc, MSc, and PhD degrees in Chemical Engineering from National Cheng Kung University in 2024, under the supervision of Prof. Chia-Yu Lin. She is currently a postdoctoral research fellow at the National Synchrotron Radiation Research Centre, Taiwan. Her research focuses on (photo-)electrochemical energy conversion, electrosynthesis, environmental remediation, and the development of advanced*



Chia-Yu Lin

*National Cheng Kung University, Taiwan, as an Assistant Professor in 2013. Currently, he is a full Professor in the Department of Chemical Engineering, National Cheng Kung University, Taiwan. His research interests include the development of functional nanomaterials for chemical sensors, (photo-)electrocatalysis, and energy-conversion devices.*

with the principles of a carbon circular economy for sustainable energy production and waste valorisation is therefore highly promising and urgently needed.<sup>6,7</sup>

Photoelectrochemical (PEC) valorisation has been demonstrated to be one of the most promising technologies for addressing energy and environmental pollution issues. It supports carbon-neutral sustainability by converting organic waste into value-added chemicals using sustainable energy sources (Fig. 1).<sup>8–11</sup> In particular, PEC reactions generally operate at room temperature under ambient conditions, thereby eliminating the substantial energy demands associated with the high temperatures and pressures typically required in conventional waste valorisation methods.<sup>12,13</sup> In addition, PEC valorisation utilises solar energy, the most abundant renewable energy resource, to drive chemical reactions using organic waste as feedstock. Therefore, solar energy can be stored in the form of solar fuels in the co-production of value-added chemicals through PEC valorisation. Compared to water splitting, one of the most extensively studied reactions in PEC systems, organic waste valorisation offers an alternative pathway for generating more economically valuable products. For example, oxygen ( $O_2$ ) is the oxidation product in water splitting and has an economic value of only 0.04 USD per kg.<sup>8</sup> In contrast, formic acid (FA), which can be generated from various organic oxidation processes, possesses an economic value approximately ten times higher than that of  $O_2$ .<sup>14</sup>

Decreasing the energy demand in PEC reactions and enhancing the production rate of products are additional advantages of replacing water oxidation with organic oxidation.



Yi-Hsuan Lai

*Yi-Hsuan Lai received her PhD degree from the University of Cambridge in 2015. She started her independent career in 2016 as an assistant professor at National Sun Yat-sen University. In 2019, she moved to National Cheng Kung University as an assistant professor and was promoted to associate professor in 2024. Her research interests include photoelectrochemistry, photocatalysis, electrocatalysis, and sustainability, with a special focus on water splitting and organic waste valorisation.*

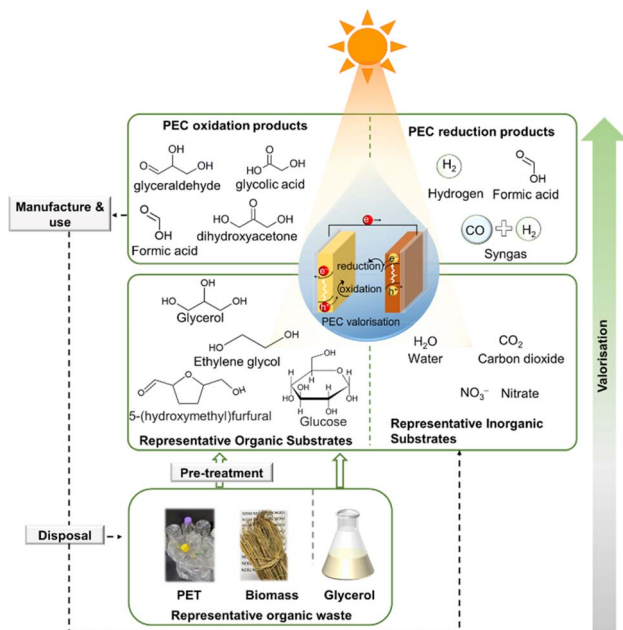
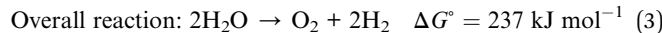
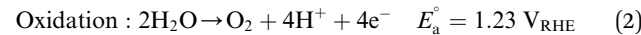


Fig. 1 Overview of PEC organic waste valorisation to drive value-added chemical and solar fuels production in a circular economy.

Water splitting consists of an oxygen evolution reaction (OER) and a hydrogen evolution reaction (HER):<sup>15,16</sup>



As shown in eqn (3), water splitting requires a high endothermic free energy change ( $\Delta G^\circ$ ) of  $237 \text{ kJ mol}^{-1}$ , which corresponds to  $\Delta E_{\text{rxn}}^\circ = -1.23 \text{ V}$  per electron transferred.<sup>17</sup>

On the other hand, replacing the OER with organic oxidation, *i.e.*, coupling HER with organic oxidation, results in a thermodynamically favourable or marginally endothermic reaction (Table 1). For example, the HER coupled with glycerol valorisation to dihydroxyacetone (DHA) requires a marginal endothermic  $\Delta G^\circ$  of only  $10.3 \text{ kJ mol}^{-1}$ . The potential required to oxidise glycerol to DHA is approximately at  $0.05 \text{ V}$  *vs.* the reversible hydrogen electrode ( $\text{V}_{\text{RHE}}$ ). Another example is ethylene glycol (EG), a monomeric unit of polyethylene terephthalate (PET), whose valorisation to FA coupled with the HER constitutes a thermodynamically favourable reaction. The potential required to oxidise EG to FA is located at a  $-0.25 \text{ V}_{\text{RHE}}$  (Table 1).

Therefore, using a PEC system to drive a PEC organic valorisation reaction coupled with  $\text{H}_2$  evolution generally results in a higher product formation rate than using the same PEC system to drive water splitting. Fig. 2a and b show that the photogenerated holes can provide greater kinetic energy, *i.e.*, a higher overpotential ( $\eta_{\text{ox}}$ ), to drive organic oxidation, as organic oxidation requires less thermodynamic energy than the

Table 1 Standard molar Gibbs free energy change ( $\Delta G^\circ$ ), standard half-cell potentials ( $E_a^\circ$  and  $E_c^\circ$ ) and standard electromotive force of the cell ( $\Delta E_{\text{rxn}}^\circ$ ) for the reaction of organics valorisation couple with  $\text{H}_2$  production

Overall reaction	Cathodic half-cell reaction	Anodic half-cell reaction
$\text{C}_6\text{H}_6\text{O}_3 \text{ (HMF)} + 2\text{H}_2\text{O} \leftrightarrow \text{C}_6\text{H}_4\text{O}_5 \text{ (FDCA)} + 3\text{H}_2$ ${}^a\Delta G^\circ = 173.7 \text{ kJ mol}^{-1}$ , ${}^b\Delta E_{\text{rxn}}^\circ = -0.30 \text{ V}$	$6\text{H}^+ + 6\text{e}^- \leftrightarrow 3\text{H}_2$ $E_c^\circ = 0.00 \text{ V}_{\text{RHE}}$	$\text{C}_6\text{H}_6\text{O}_3 \text{ (HMF)} + 2\text{H}_2\text{O} \rightarrow \text{C}_6\text{H}_4\text{O}_5 \text{ (FDCA)} + 6\text{H}^+ + 6\text{e}^-$ ${}^aE_a^\circ = 0.30 \text{ V}_{\text{RHE}}$
$\text{C}_2\text{H}_6\text{O}_2 \text{ (EG)} + 2\text{OH}^- \leftrightarrow 2 \text{HCOO}^- \text{ (FA)} + 3\text{H}_2$ ${}^c\Delta G^\circ = -147.5 \text{ kJ mol}^{-1}$ , ${}^d\Delta E_{\text{rxn}}^\circ = 0.25 \text{ V}$	$6\text{H}_2\text{O} + 6\text{e}^- \leftrightarrow 3\text{H}_2 + 6\text{OH}^-$ $E_c^\circ = 0.00 \text{ V}_{\text{RHE}}$	$\text{C}_2\text{H}_6\text{O}_2 \text{ (EG)} + 8\text{OH}^- \rightarrow 2 \text{HCOO}^- \text{ (FA)} + 6\text{H}_2\text{O} + 6\text{e}^-$ ${}^bE_a^\circ = -0.25 \text{ V}_{\text{RHE}}$
$\text{C}_2\text{H}_6\text{O}_2 \text{ (EG)} + \text{H}_2\text{O} \leftrightarrow \text{C}_2\text{H}_4\text{O}_3 \text{ (GLA)} + 2\text{H}_2$ ${}^c\Delta G^\circ = 105.2 \text{ kJ mol}^{-1}$ , ${}^d\Delta E_{\text{rxn}}^\circ = -0.27 \text{ V}$	$4\text{H}_2\text{O} + 4\text{e}^- \leftrightarrow 2\text{H}_2 + 4\text{OH}^-$ $E_c^\circ = 0.00 \text{ V}_{\text{RHE}}$	$\text{C}_2\text{H}_6\text{O}_2 \text{ (EG)} + 4\text{OH}^- \rightarrow \text{C}_2\text{H}_4\text{O}_3 \text{ (GLA)} + 3\text{H}_2\text{O} + 4\text{e}^-$ ${}^bE_a^\circ = 0.27 \text{ V}_{\text{RHE}}$
$\text{C}_3\text{H}_8\text{O}_3 \text{ (glycerol)} \leftrightarrow \text{C}_3\text{H}_6\text{O}_3 \text{ (DHA)} + \text{H}_2$ ${}^c\Delta G^\circ = 10.3 \text{ kJ mol}^{-1}$ , ${}^d\Delta E_{\text{rxn}}^\circ = -0.05 \text{ V}$	$2\text{H}^+ + 2\text{e}^- \leftrightarrow \text{H}_2$ $E_c^\circ = 0.00 \text{ V}_{\text{RHE}}$	$\text{C}_3\text{H}_8\text{O}_3 \text{ (glycerol)} \rightarrow \text{C}_3\text{H}_6\text{O}_3 \text{ (DHA)} + 2\text{H}^+ + 2\text{e}^-$ ${}^bE_a^\circ = 0.05 \text{ V}_{\text{RHE}}$
$\text{C}_3\text{H}_8\text{O}_3 \text{ (glycerol)} \leftrightarrow \text{C}_3\text{H}_6\text{O}_3 \text{ (GLAD)} + \text{H}_2$ ${}^c\Delta G^\circ = 37.3 \text{ kJ mol}^{-1}$ , ${}^d\Delta E_{\text{rxn}}^\circ = -0.19 \text{ V}$	$2\text{H}^+ + 2\text{e}^- \leftrightarrow \text{H}_2$ $E_c^\circ = 0.00 \text{ V}_{\text{RHE}}$	$\text{C}_3\text{H}_8\text{O}_3 \text{ (glycerol)} \rightarrow \text{C}_3\text{H}_6\text{O}_3 \text{ (GLAD)} + 2\text{H}^+ + 2\text{e}^-$ ${}^bE_a^\circ = 0.19 \text{ V}_{\text{RHE}}$
$\text{C}_3\text{H}_8\text{O}_3 \text{ (glycerol)} + 3\text{OH}^- \leftrightarrow 3 \text{HCOO}^- \text{ (FA)} + 4\text{H}_2$ ${}^c\Delta G^\circ = 65.6 \text{ kJ mol}^{-1}$ , ${}^d\Delta E_{\text{rxn}}^\circ = -0.09 \text{ V}$	$8\text{H}_2\text{O} + 8\text{e}^- \leftrightarrow 4\text{H}_2 + 8\text{OH}^-$ $E_c^\circ = 0.00 \text{ V}_{\text{RHE}}$	$\text{C}_3\text{H}_8\text{O}_3 \text{ (glycerol)} + 11\text{OH}^- \rightarrow 3 \text{HCOO}^- \text{ (FA)} + 8\text{H}_2\text{O} + 8\text{e}^-$ ${}^bE_a^\circ = 0.09 \text{ V}_{\text{RHE}}$
$\text{C}_6\text{H}_{12}\text{O}_6 \text{ (glucose)} + 6\text{OH}^- \leftrightarrow 6 \text{HCOO}^- \text{ (FA)} + 6\text{H}_2$ ${}^c\Delta G^\circ = 47.9 \text{ kJ mol}^{-1}$ , ${}^d\Delta E_{\text{rxn}}^\circ = -0.04 \text{ V}^\circ$	$12\text{H}_2\text{O} + 12\text{e}^- \leftrightarrow 6\text{H}_2 + 12\text{OH}^-$ $E_c^\circ = 0.00 \text{ V}_{\text{RHE}}$	$\text{C}_6\text{H}_{12}\text{O}_6 \text{ (glucose)} + 18\text{OH}^- \rightarrow 6 \text{HCOO}^- \text{ (FA)} + 12\text{H}_2\text{O} + 12\text{e}^-$ ${}^bE_a^\circ = 0.04 \text{ V}_{\text{RHE}}$
$\text{C}_6\text{H}_{12}\text{O}_6 \text{ (glucose)} + \text{H}_2\text{O} \leftrightarrow \text{C}_6\text{H}_{12}\text{O}_7 \text{ (GNA)} + \text{H}_2$ ${}^c\Delta G^\circ = 70.9 \text{ kJ mol}^{-1}$ , ${}^d\Delta E_{\text{rxn}}^\circ = -0.37 \text{ V}$	$2\text{H}^+ + 2\text{e}^- \leftrightarrow \text{H}_2$ $E_c^\circ = 0.00 \text{ V}_{\text{RHE}}$	$\text{C}_6\text{H}_{12}\text{O}_6 \text{ (glucose)} + \text{H}_2\text{O} \rightarrow \text{C}_6\text{H}_{12}\text{O}_7 \text{ (GNA)} + 2\text{H}^+ + 2\text{e}^-$ ${}^bE_a^\circ = 0.37 \text{ V}_{\text{RHE}}$
$\text{C}_6\text{H}_{12}\text{O}_6 \text{ (glucose)} + 2\text{H}_2\text{O} \leftrightarrow \text{C}_6\text{H}_{10}\text{O}_8 \text{ (GRA)} + 3\text{H}_2$ ${}^c\Delta G^\circ = 179.1 \text{ kJ mol}^{-1}$ , ${}^d\Delta E_{\text{rxn}}^\circ = -0.31 \text{ V}$	$6\text{H}^+ + 6\text{e}^- \leftrightarrow 3\text{H}_2$ $E_c^\circ = 0.00 \text{ V}_{\text{RHE}}$	$\text{C}_6\text{H}_{12}\text{O}_6 \text{ (glucose)} + 2\text{H}_2\text{O} \rightarrow \text{C}_6\text{H}_{10}\text{O}_8 \text{ (GRA)} + 6\text{H}^+ + 6\text{e}^-$ ${}^bE_a^\circ = 0.31 \text{ V}_{\text{RHE}}$

<sup>a</sup> Derived from ref. 6. <sup>b</sup> Obtained by  $\Delta E_{\text{rxn}}^\circ = E_c^\circ - E_a^\circ$ . <sup>c</sup> Obtained by  $\Delta G^\circ = \sum m\Delta G_f^\circ(\text{product}) - m\Delta G_f^\circ(\text{reactant})$ , where  $m$  is the respective coefficient in the balanced chemical reaction and  $\Delta G_f^\circ$  is the standard molar Gibbs free energy of formation (Table S1). <sup>d</sup>  $\Delta E_{\text{rxn}}^\circ = -\frac{\Delta G^\circ}{nF}$ , where  $n$  is the number of electrons transferred (mol) and  $F$  is the Faraday constant of  $96\,485 \text{ C mol}^{-1}$ . HMF: 5-hydroxymethylfurfural; FDCA: 2,5-furandicarboxylic acid; FA: formate; EG: ethylene glycol; GLA: glycolic acid; DHA: dihydroxyacetone; GLAD: glyceraldehyde; GNA: gluconic acid; and GRA: glucaric acid.



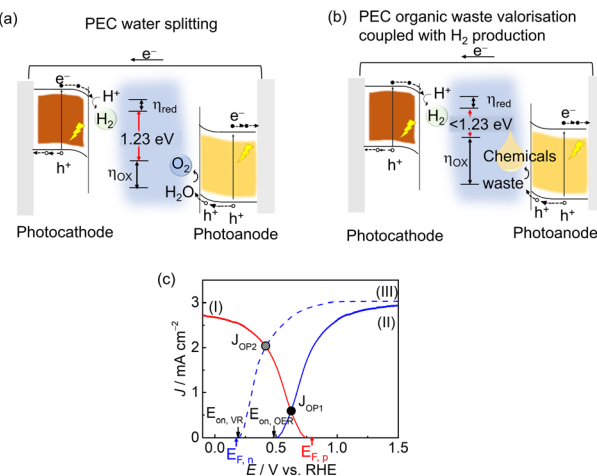


Fig. 2 Tandem PEC cells for (a) water splitting and (b) organic waste valorisation. (c) Overlaid current ( $J$ ) potential ( $E$ ) curves measured in a three-electrode system with a photocathode (red) and a photoanode (blue) in water with (dash) or without (solid) organic substrates under light irradiation. The operating photocurrent of a two-electrode tandem PEC cell can be predicted by the intersection of the oxidation and reduction photocurrents.  $E_{F,n}$  and  $E_{F,p}$  represent the flat band edge of the n-type (photoanode) and p-type (photocathode) semiconductor, respectively, under light illumination.

OER. Severe surface charge recombination caused by the sluggish kinetics of the OER would result in the onset potential for OER ( $E_{on,OER}$ ) deviating significantly from the flat band potential of the photoanode ( $E_{F,n}$ ), as shown in Fig. 2c. In contrast, surface charge recombination can generally be mitigated by replacing the OER with a suitable organic oxidation reaction, in which the onset potential of organic valorisation ( $E_{on,VR}$ ) can be negatively shifted toward the  $E_{F,n}$  of the photoanode. Taking  $\alpha$ -Fe<sub>2</sub>O<sub>3</sub> as an example, the onset potential shifted from 1.1 V<sub>RHE</sub> to 0.85 V<sub>RHE</sub> by replacing the OER with the EG oxidation reaction,<sup>9</sup> while it shifted from 1.0 V<sub>RHE</sub> to 0.7 V<sub>RHE</sub> by replacing the OER with the glucose oxidation reaction.<sup>18</sup> The deviation range between the onset potential and the  $E_{F,n}$  of the photoanode is crucial in determining the overall PEC cell performance. If an integrated PEC system comprising a photocathode and a photoanode is employed, the operating photocurrent ( $J_{OP}$ ) is determined by the intersection of the photocurrents of the two half-reactions (oxidation and reduction) (Fig. 2c). The difference between  $E_{on,OER}$  and  $E_{on,VR}$  for the same photoanode resulted in the  $J_{OP}$  of PEC water splitting ( $J_{OP1}$ ) being lower than that of PEC organic valorisation coupled with the same reduction reaction ( $J_{OP2}$ ).

PEC organic waste valorisation may also provide an alternative approach to mitigate the instability of photoelectrodes in PEC water splitting. The thermodynamic stability of a photoelectrode depends on the relative thermodynamic potential of the semiconductor and the potential of the target redox reaction. Taking water oxidation as an example, if the thermodynamic oxidation potential ( $E_{ox}$ ) of a photoanode is more negative than the potential of the OER (1.23 V<sub>RHE</sub>), the photoanode would undergo photocorrosion by its photogenerated

holes.<sup>19</sup> Most non-oxide semiconductors, such as ZnS, CdS, ZnSe, etc., and some oxide semiconductors, such as ZnO, are susceptible to oxidation based on thermodynamic predictions.<sup>19</sup> However, if these photoanodes are used for glycerol valorisation, for example, they are thermodynamically resistant to photocorrosion, as their  $E_{ox}$  is more positive than the potential for glycerol valorisation to DHA (0.05 V<sub>RHE</sub>). Given these advantages, research on PEC organic waste valorisation has rapidly increased in recent years. This perspective review focuses on PEC organic waste valorisation. Organic waste substrates, including biomass, its derivatives, and plastics, are particularly highlighted in this review, since biomass derived from food and lignocellulosic sources accounts for the majority composition (~60%) of solid waste. Although plastics represent a smaller fraction (12%) compared to plant-derived materials, their non-biodegradability poses a significantly detrimental effect on soil, water, marine life, and human health. Beyond the substrate used in PEC valorisation, variables such as solution pH, operation duration, and light intensity also influence PEC performance (Fig. 3). In particular, the properties of the photoelectrode represent the most crucial factor determining the upper limit of PEC valorisation system performance. Hence, in this perspective review, the working principle of a PEC reaction is introduced, followed by an overview of the materials and optical properties of the state-of-the-art photoelectrodes applied in PEC organic valorisation. Recent progress in designing efficient photoanode strategies for organic waste oxidation to generate value-added chemicals is subsequently discussed. Value-added chemical synthesis through reduction reactions using PEC cells is then covered, although the reported research in this area remains relatively limited compared to oxidation. Finally, recent developments in integrated PEC cells and their practical evaluation for solar fuel and value-added chemical production are reviewed, followed by a discussion of perspectives. Efficiency, stability, and scalability are the three key system requirements for the successful deployment of PEC systems.<sup>20</sup> Long-term stability is an essential criterion for the practical implementation of PEC technologies. Without sustained performance over long-term operation, even highly efficient PEC devices cannot satisfy the economic, safety, and reliability standards required for commercialisation. Therefore, unlike most recent review papers, this work not only focuses on

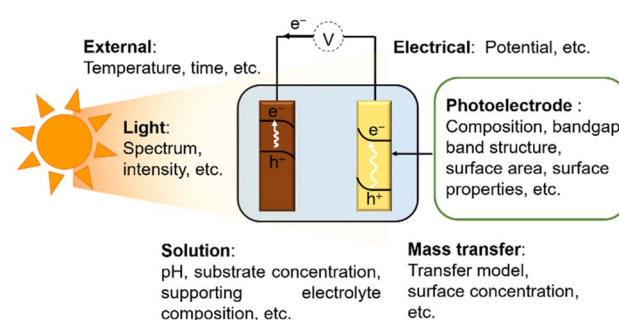


Fig. 3 Parameters affecting the performance of a PEC cell for organic waste valorisation.



efficiencies but also addresses stability, scalability, and the compatibility of photoelectrodes and co-catalysts in integrated PEC cells. Finally, conclusions and future perspectives on feasible strategies for PEC valorisation are discussed. We hope this will guide readers in designing effective, robust, and scalable PEC systems for organic waste valorisation, particularly in the context of integrated PEC cells.

## 2. PEC valorisation

### 2.1 Working principle of PEC reactions

PEC devices directly employ the solid-liquid junction to drive desired reactions under light illumination. When the photoelectrode is immersed in the electrolyte, charge transfer occurs between the semiconductor and the electrolyte until equilibrium is reached between the Fermi level of the semiconductor and the redox potential of the electrolyte. The built-in electric field at the surface of an n-type semiconductor resulted in upward band bending, favouring photo-driven oxidation reactions. In contrast, the built-in electric field at the surface of a p-type semiconductor resulted in downward band bending, favouring photo-driven reduction reactions. Upon light

irradiation,  $e^-/h^+$  pairs are photo-generated within the photoelectrode, as indicated by route (i) in Fig. 4. The photo-generated minority charge carriers, *i.e.*, holes for n-type semiconductors and electrons for p-type semiconductors, are then transported to the electrode surface, driven by the built-in electric field at the semiconductor/liquid interface, and subsequently transferred into the electrolyte to carry out the redox reaction, as shown in routes (ii) and (iii). However, it should also be noted that to drive a desired oxidation reaction, the holes from the valence band ( $E_{VB}$ ) of a photoelectrode must possess sufficient driving force to overcome both the thermodynamic and kinetic barriers of the oxidation process. Conversely, the photogenerated electrons from the conduction band ( $E_{CB}$ ) must have adequate energy to drive the reduction reaction.

The performance of a photoelectrode in terms of photocurrent density ( $J_{PEC}$ ) can be described by eqn (4):

$$J_{PEC} = J_{\max} \times \eta_{LHE} \times \eta_{sep} \times \eta_{int} \quad (4)$$

Here,  $J_{\max}$  is the maximum theoretical photocurrent density, determined by the bandgap of the photoelectrode, and can be estimated by assuming 100% incident photon-to-current conversion for photons with energies exceeding the bandgap. On the other hand,  $\eta_{LHE}$  represents the light-harvesting efficiency of the photoelectrode, while the charge separation efficiency of  $\eta_{sep}$  and charge transfer efficiency of  $\eta_{int}$  are the yields of minority carrier transport to the photoelectrode surface and interfacial charge transfer, respectively. It is therefore known that an ideal photoelectrode should have (i) suitable band positions to provide enough driving force for a desired reaction, (ii) as narrow bandgap as possible to have a high  $J_{\max}$ , (iii) a sufficient material thickness to harvest all incident photons, (iv) effective charge separation to prevent charge recombination within the semiconductor, (v) excellent surface catalytic activity, and (vi) last but not least, stability and scalability, for the successful development of a PEC technology.

**2.1.1 Band structure.** The first step in the PEC reaction is to harvest solar light, and therefore, the ability to utilise energy in the solar spectrum determines the  $J_{\max}$  of a semiconductor. Therefore, a semiconductor with a smaller bandgap results in a higher  $J_{\max}$ , as shown in Fig. 5a. However, appropriate band

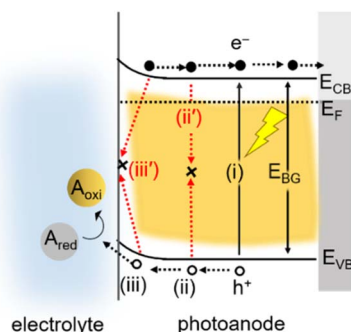


Fig. 4 Schematic of a photoanode performing a PEC reaction under light illumination. The process can be decoupled into three major steps: (i) light absorption to generate electron–hole pairs, (ii) transport of photogenerated holes to the photoanode surface, and (iii) interfacial charge transfer to oxidise  $A_{\text{red}}$  to  $A_{\text{oxi}}$  in the electrolyte. Unfavourable recombination paths, including (ii') bulk recombination and (iii') surface recombination, are also shown.

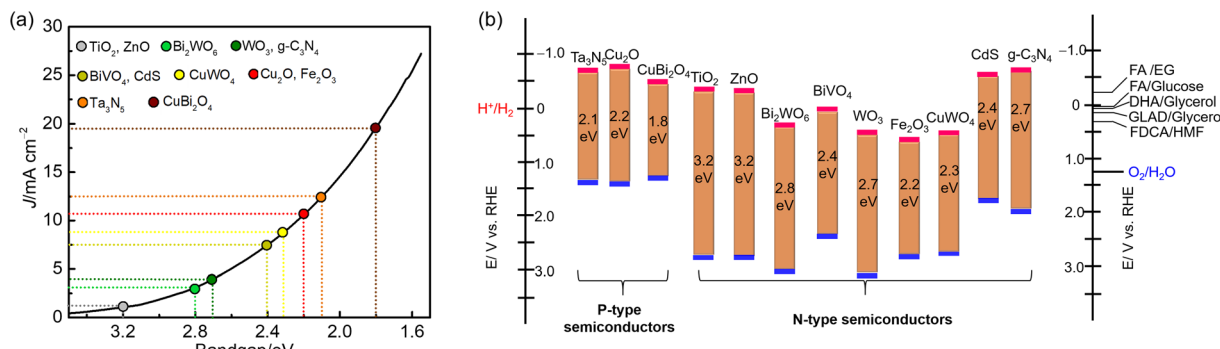


Fig. 5 (a) Maximum theoretical photocurrent of different bandgap semiconductors under one-sun illumination based on the air mass (AM) 1.5 G spectrum. (b) Band structure of representative photoelectrodes.



alignment is essential to carry out the PEC reactions effectively. The  $E_{CB}$  of the semiconductor should be more negative than the potential of a reduction reaction to provide sufficient reductive power for a desired reaction by the photo-generated electrons. For example, to perform  $H_2$  evolution, the  $E_{CB}$  of a photocathode must be more negative than 0 V<sub>RHE</sub>, which is the redox potential of  $H^+/H_2$ . Well-known photocathodes for  $H_2$  evolution include  $Cu_2O$ ,<sup>21–23</sup>  $CuBi_2O_4$ ,<sup>24,25</sup> and  $CuFeO_2$ .<sup>26,27</sup> Although the photo-driven electrons of those Cu-based photocathodes might have sufficient driving force for some organic reduction reactions, such as 5-hydroxymethylfurfural (HMF) reduction to 2,5-bis(hydroxymethyl)furan (BHMF),<sup>28</sup> their use in PEC organic valorisation is still limited.

On the other hand, the  $E_{VB}$  of the semiconductor should be more positive than the potential of an oxidation reaction, such as water oxidation or organic oxidation. This ensures that the holes created by light absorption possess sufficient oxidative power to oxidise water or organic waste.<sup>29–32</sup> In PEC water splitting, the state-of-the-art photoanode includes  $TiO_2$ ,<sup>33–35</sup>  $ZnO$ ,<sup>35–37</sup>  $BiVO_4$ ,<sup>38,39</sup>  $WO_3$ ,<sup>38,40–43</sup>  $\alpha\text{-Fe}_2O_3$ .<sup>44–46</sup> Those photoanodes have an  $E_{VB}$  located at  $\geq 2.5$  V<sub>RHE</sub> (Fig. 5b), providing significant overpotential for water oxidation. As previously mentioned, the redox potential of most organic oxidations in organic valorisation research is less positive than that of the OER. Most of the photoanodes used in PEC water oxidation can be utilised and have been investigated as effective photoanodes in PEC organic oxidation. However, the photo-driven holes have a sufficient driving force for both the oxidation of water and organics. The selectivity of organic valorisation might remain an issue, as the parasitic reaction of the OER could occur.

**2.1.2 Light harvesting, charge separation, and charge transfer.** The three indicators of  $\eta_{LHE}$ ,  $\eta_{sep}$ , and  $\eta_{inj}$  determine the efficiency of a given photoelectrode. The thickness of a photoelectrode must be greater than its absorption length to absorb all incident photons that have energy greater than the bandgap of the photoelectrode. The absorption length can be estimated by the inverse of the absorption coefficient of the semiconductor near its band edge.<sup>17</sup> The lifetime and diffusion length of the charge carriers in a given electrode govern its  $\eta_{sep}$ . The transportation length for minority charge carriers must be shorter than the diffusion length of the charge carriers, or severe charge recombination will occur. It is worth noting that contradictory requirements exist in obtaining promising  $\eta_{LHE}$  and  $\eta_{sep}$  in a planar electrode, as the light-harvesting direction is the same as that of charge carrier transport. Nanostructuring a photoelectrode is generally an effective strategy for decoupling the direction of light harvesting and minority charge carrier transport, thereby achieving high yields in both  $\eta_{LHE}$  and  $\eta_{sep}$ .<sup>17</sup> However, nanostructuring also leads to a decrease in photovoltage.<sup>17</sup> Other efforts, including heterojunction and doping, have been devoted to enhancing  $\eta_{LHE}$  and  $\eta_{sep}$ . The third indicator,  $\eta_{inj}$ , is closely related to the activity of surface catalysts for the chemical reactions. Some photoelectrodes themselves act as efficient catalysts for a desired reaction, while others do not. In the latter case, an efficient co-catalyst must be applied to the surface of a photoelectrode to improve its  $\eta_{inj}$ .

**2.1.3 Stability.** Meeting the criterion of long-term stability is crucial for the PEC system to be implemented for practical applications. To be applicable for practical use and compete with other technologies, a techno-economic analysis of PEC cells for  $H_2$  production has shown that a PEC cell should have a solar-to- $H_2$  efficiency of over 26% and a PEC cell lifetime of over 2 years.<sup>47</sup> The relative potential between the redox couple and the oxidation/reduction potential ( $E_{ox}/E_{red}$ ) of the semiconductor provides a first prediction of the stability of a photoelectrode in carrying out a particular reaction.<sup>19</sup> Taking PEC  $H_2$  evolution as an example, a photocathode is susceptible to photocorrosion if its  $E_{red}$  is more positive than the hydrogen evolution potential ( $E_{(H^+/H_2)}$ ). A typical example is  $Cu_2O$ , which is readily reduced to Cu by its photo-generated electrons during the HER. Surface modification has been demonstrated to be an effective strategy for enhancing the photochemical stability of semiconductors.<sup>48–51</sup> For instance, the application of a  $TiO_2$  protection layer on a  $Cu_2O$  photocathode enabled stable operation for over 100 h in PEC water splitting.<sup>22</sup> Conversely, a photoanode resists photocorrosion during water splitting if its  $E_{ox}$  is more positive than the potential of the OER (1.23 V<sub>RHE</sub>).  $TiO_2$  and  $WO_3$  are examples of such materials and are widely used as photoanodes for water splitting. However, in addition to the thermodynamic considerations during PEC, chemical and kinetic factors must also be accounted for when evaluating the robustness of a photoelectrode. For example, the presence of  $OH^-$  ions in the electrolyte results in the dissolution of  $WO_3$ , making it chemically unstable in a solution with pH  $\geq 7$ .<sup>52</sup> In addition, due to the sluggish kinetics of water oxidation, by-products such as  $H_2O_2$  may form and subsequently corrode  $WO_3$  during the OER.

The replacement of water oxidation with less energy-demanding organic oxidation, at least, partially alleviates the thermodynamic and kinetic constraints in selecting photoanodes. For example, nanosheet-structured  $WO_3$  lost 50% of its initial photoactivity during water splitting in a neutral solution within a few minutes.<sup>53</sup> However, the nanosheet-structured  $WO_3$  does not lose 50% of its initial photoactivity until 12 h of operation in the glycerol valorisation reaction.<sup>54</sup> The stability difference between water oxidation and glycerol valorisation on  $WO_3$  possibly resulted from difference in their reaction kinetics. Peroxo-species are readily formed during sluggish water oxidation, which leads to the corrosion of  $WO_3$ . In contrast, peroxo-species are possibly eliminated during glycerol valorisation. Similar results have also been reported for  $BiVO_4$ .<sup>55</sup> However, the mechanisms by which photocorrosion is alleviated when replacing water oxidation with organic valorisation might vary among different photoanodes. Eliminating surface charge recombination may be another contributing factor to why a photoanode, such as  $BiVO_4$ , typically exhibits better stability for organic (e.g., EG, glycerol) valorisation than for water oxidation. To date, PEC organic valorisation in the half-cell has achieved a maximum operation time of up to 150 h,<sup>56</sup> and 80 h has been reported for an integrated cell.<sup>18</sup> This highlights that the current progress in stability remains significantly below the criteria required for practical implementation and warrants





Table 2 Selected publications with important parameters for PEC organic waste valorisation using state-of-the-art photoelectrodes

Photoelectrode	Modification	Substrate	Spectrum and intensity of light	Supporting electrolyte	FE [%] of main product@E	$J [\text{mA cm}^{-2}] \phi_{\text{PE}} @ E$	$t_{0.6} [\text{h}] @ E$	Ref.
<b>TiO<sub>2</sub>-based photoelectrode</b>								
TiO <sub>2</sub>	N/A	Glycerol (0.1 M)	385 nm, 10 mW cm <sup>-2</sup>	Na <sub>2</sub> SO <sub>4</sub> (0.5 M, pH 7)	FA: ≈ 33@1 V <sub>RHE</sub>	≈ 2/N.A. @ 1.3 V <sub>RHE</sub>	N/A	102
TiO <sub>2</sub>	N/A	Cellulose (0.15 M)	λ < 500 nm	NaOH (2 M)	Malonic acid: ≈ 4.5 at 1 V <sub>RHE</sub>	≈ 5/N.A. @ 0.5 V <sub>RHE</sub>	>3@0 V <sub>RHE</sub>	103
TiO <sub>2</sub>	Nanostructure	Glycerol (0.1 M)	AM 1.5 G, 100 mW cm <sup>-2</sup>	Na <sub>2</sub> SO <sub>4</sub> (1 M, pH 2)	GLAD: 32@1.23 V <sub>RHE</sub>	≈ 0.9/0.84@0.5 V <sub>RHE</sub>	>10@1.23 V <sub>RHE</sub>	104
TiO <sub>2</sub> /Bi <sub>2</sub> O <sub>3</sub>	Heterojunction	Cellulose	AM 1.5 G, 100 mW cm <sup>-2</sup>	NaOH (0.1 M)	FA: 83.9 ± 4.9 at 0.5 V <sub>RHE</sub>	≈ 0.36/0.34@0.5 V <sub>RHE</sub>	>6@0.5 V <sub>RHE</sub>	64
Bi <sub>2</sub> O <sub>3</sub> /TiO <sub>2</sub>	Heterojunction/Co-catalyst	Glycerol (0.1 M)	AM 1.5 G, 100 mW cm <sup>-2</sup>	Na <sub>2</sub> SO <sub>4</sub> (0.5 M, pH 2)	DHA: 62.2@1.0 V <sub>RHE</sub>	≈ 2.4/2.2@1.2 V <sub>RHE</sub>	N/A	56
Ag@LDH@TiO <sub>2</sub>	Co-catalyst	Glycerol (0.1 M)	AM 1.5 G, 100 mW cm <sup>-2</sup>	Na <sub>2</sub> SO <sub>4</sub> (0.5 M, pH 7)	DHA: 55@1.2 V <sub>RHE</sub>	≈ 2.3/2.1@1.2 V <sub>RHE</sub>	>4@1.2 V <sub>RHE</sub>	105
TiO <sub>2</sub> /nanoNiP	Co-catalyst	PET lysate	AM 1.5 G, 100 mW cm <sup>-2</sup>	KOH (1 M, pH 14)	FA: 57.1 ± 1.7@0.5 V	≈ 0.6/0.57@1.2 V <sub>RHE</sub>	>2@0.5 V <sub>RHE</sub>	106
<b>WO<sub>3</sub>-based photoelectrode</b>								
WO <sub>3</sub>	N/A	HMF (5 mM)	100 mW cm <sup>-2</sup>	NaPi (0.1 M, pH 4)	N/A	≈ 1.5/N.A. @ 1.2 V <sub>RHE</sub>	N/A	67
WO <sub>3</sub>	N/A	Cyclohexane (18 mL)	100 mW cm <sup>-2</sup>	tBuOH (12 mL) and HNO <sub>3</sub> (2 mL)	KA oil: 76@0.5 V	≈ 2/N.A. @ 1.2 V <sub>RHE</sub>	N/A	65
WO <sub>3</sub>	N/A	Glycerol (0.1 M)	350 mW cm <sup>-2</sup>	Na <sub>2</sub> SO <sub>4</sub> (0.5 M, pH 5.5)	GLAD: ≈ 30, DHA: ≈ 20@1.2 V <sub>RHE</sub>	≈ 0.35/N.A. @ 1.2 V <sub>RHE</sub>	>5@1.2 V <sub>RHE</sub>	66
WO <sub>3</sub>	Nanostructure	Glucose (0.1 M)	AM 1.5 G, 100 mW cm <sup>-2</sup>	NaCl (0.5 M, pH 4)	Glucogenic acid: 20@1.2 V <sub>RHE</sub>	6/1.5@1.2 V <sub>RHE</sub>	>20@1.23 V <sub>RHE</sub>	107
m-WO <sub>3</sub>	Crystal phase	HMF (5 mM)	AM 1.5 G, 100 mW cm <sup>-2</sup>	NaBi (0.1 M, pH 4)	N/A	≈ 0.9/0.23@1.2 V <sub>RHE</sub>	≈ 1@1.1 V <sub>RHE</sub>	68
WO <sub>3</sub>	Crystal facet	Glycerol (2 M)	AM 1.5 G, 100 mW cm <sup>-2</sup>	Na <sub>2</sub> SO <sub>4</sub> (0.1 M, pH 2)	GLAD: ≈ 75, DHA: ≈ 20@1.2 V <sub>RHE</sub>	3.4@0.85@1.2 V <sub>RHE</sub>	>12@1.2 V <sub>RHE</sub>	69
WO <sub>3</sub>	Crystal facet	Methane	100 mW cm <sup>-2</sup>	Na <sub>2</sub> SO <sub>4</sub> (0.1 M, pH 2)	EG: 23.9@1.3 V <sub>RHE</sub>	≈ 3/N.A. @ 1.2 V <sub>RHE</sub>	>12@0.9 V <sub>RHE</sub>	108
WO <sub>3</sub> /TiO <sub>2</sub>	Heterojunction	Glycerol (0.1 M)	AM 1.5 G, 100 mW cm <sup>-2</sup>	Na <sub>2</sub> SO <sub>4</sub> (0.5 M, pH 6)	GLAD&DHA: 70@1.2 V <sub>RHE</sub>	2.89@0.72@1.23 V <sub>RHE</sub>	>1@1.23 V <sub>RHE</sub>	109
N-WO <sub>3</sub>	Dopant	Glycerol (0.1 M)	365 nm	Na <sub>2</sub> SO <sub>4</sub> (0.5 M, pH 1)	CO: 40@0.6 V <sub>RHE</sub>	1.5/N.A. @ 0.7 V <sub>RHE</sub>	>30 V	110
<b>BiVO<sub>4</sub>-based photoelectrode</b>								
BiVO <sub>4</sub>	N/A	Glycerol (2 M)	AM 1.5 G, 100 mW cm <sup>-2</sup>	Na <sub>2</sub> B <sub>4</sub> O <sub>7</sub> (0.1 M, pH 9.4)	N/A	1.3/0.17@1.2 V <sub>RHE</sub>	≈ 7@0.7 V <sub>RHE</sub>	76
BiVO <sub>4</sub>	N/A	Lignin (5 mg mL <sup>-1</sup> )	λ > 400 nm, 100 mW cm <sup>-2</sup>	KHCO <sub>3</sub> buffer (10 mM, pH 8.2)	N/A	≈ 0.53/N.A. @ 0.6 V <sub>Ag/AgCl</sub>	N/A	71
BiVO <sub>4</sub>	N/A	HMF (5 mM)	AM 1.5 G, 100 mW cm <sup>-2</sup>	Borate buffer (0.5 M, pH 9.2) containing 7.5 mM TEMPO	FDCA: 93-94@1.54 V <sub>RHE</sub>	N/A	N/A	70
Mo:BiVO <sub>4</sub> /NiCo- LDH	Dopant/Co-catalyst	EG (1 M)	100 mW cm <sup>-2</sup>	KOH (0.1 M)	FA: ≈ 100@1.2 V <sub>RHE</sub>	≈ 2.3/N.A. @ 1.2 V <sub>RHE</sub>	>3@1.0 V <sub>RHE</sub>	111
Ta:BiVO <sub>4</sub>	Dopant	Glycerol (0.1 M)	λ > 422 nm, AM 1.5 G, 100 mW cm <sup>-2</sup>	H <sub>2</sub> SO <sub>4</sub> (25 mM)	DHA: 61@1.0 V <sub>RHE</sub>	3.07@0.4@1.23 V <sub>RHE</sub>	>2@1.0 V <sub>RHE</sub>	112
NiO <sub>x</sub> (OH) <sub>y</sub> / W:BiVO <sub>4</sub>	Co-catalyst	Glycerol (0.1 M)	AM 1.5 G, 100 mW cm <sup>-2</sup>	KBi (0.5 M, pH 9.3)	FA: ≈ 30, DHA: ≈ 19@1.2 V <sub>RHE</sub>	3.5/0.49@1.2 V <sub>RHE</sub>	>24@0.8 V <sub>RHE</sub>	55



Table 2 (Contd.)

Photoelectrode	Modification	Substrate	Spectrum and intensity of light	Supporting electrolyte	FE [%] of main product@E	$J [\text{mA cm}^{-2}] / \phi_{\text{PE}}^a @ E$	$t_{0.6}^b [\text{h}] @ E$	Ref.
$\text{BiVO}_4$	Structural	Glycerol (0.1 M)	AM 1.5 G, 100 mW $\text{cm}^{-2}$	$\text{Na}_2\text{SO}_4$ (0.5 M, pH 2)	DHA: 29.1@1.23 $\text{V}_{\text{RHE}}$ DHA: $\approx$ 30@0.6 $\text{V}_{\text{RHE}}$	6/0.8@1.23 $\text{V}_{\text{RHE}}$	>4@1.23 $\text{V}_{\text{RHE}}$	74
$\text{BiVO}_4$	Nanostructure	Glycerol (0.1 M)	AM 1.5 G, 100 mW $\text{cm}^{-2}$	$\text{Na}_2\text{SO}_4$ (0.5 M, pH 2)	DHA: $\approx$ 45@1.23 $\text{V}_{\text{RHE}}$	3.7/0.49@1.2 $\text{V}_{\text{RHE}}$	>5@1.0 $\text{V}_{\text{RHE}}$	75
Bi-rich $\text{BiVO}_{4-x}$	Surface atom engineered	Glycerol (0.1 M)	AM 1.5 G, 100 mW $\text{cm}^{-2}$	$\text{Na}_2\text{SO}_4$ (0.5 M, pH 2)	DHA: $\approx$ 45@1.23 $\text{V}_{\text{RHE}}$	4.26/0.57@1.2 $\text{V}_{\text{RHE}}$	>5@1.23 $\text{V}_{\text{RHE}}$	113
$\text{BiVO}_4(010)$	Crystal facet	Glycerol (0.1 M)	AM 1.5 G, 100 mW $\text{cm}^{-2}$	$\text{Na}_2\text{B}_4\text{O}_7$ (0.1 M, pH 2)	N/A	$\approx$ 1.2/0.16@1.2 $\text{V}_{\text{RHE}}$	>2@1.1 $\text{V}_{\text{RHE}}$	114
Mo:BiVO <sub>4</sub> (001)	Crystal facet/ dopant/ nanostructure	Glycerol (0.5 M)	AM 1.5 G, 100 mW $\text{cm}^{-2}$	$\text{Na}_2\text{SO}_4$ (0.1 M, pH 2)	DHA: 23@1.23 $\text{V}_{\text{RHE}}$	7.45/0.99@1.23 $\text{V}_{\text{RHE}}$	>100@0.8 $\text{V}_{\text{RHE}}$	115
<b>Fe<sub>2</sub>O<sub>3</sub>-based photoelectrode</b>								
Fe <sub>2</sub> O <sub>3</sub>	N/A	Cyclohexene (10 mM)	AM 1.5 G, 100 mW $\text{cm}^{-2}$	CH <sub>3</sub> CN (20% H <sub>2</sub> O) containing 0.1 M tetrabutylammonium tetrafluoroborate	Cyclohexene oxide: 35.2 $\pm$ 1.6@0.8 $\text{V}_{\text{Ag}/\text{AgCl}}$	$\approx$ 0.20/0.017@1.2 $\text{V}_{\text{Ag}/\text{AgCl}}$	>2@0.8 $\text{V}_{\text{Ag}/\text{AgCl}}$	116
Fe <sub>2</sub> O <sub>3</sub>	Ni/Pi/ $\alpha$ -Fe <sub>2</sub> O <sub>3</sub>	Glycerol (2 M)	AM 1.5 G, 100 mW $\text{cm}^{-2}$	NaOH (1 M)	FA: $\approx$ 46@1.1 $\text{V}_{\text{RHE}}$	2.01/0.17@1.23 $\text{V}_{\text{RHE}}$	>36@1.23 $\text{V}_{\text{RHE}}$	117
NiOOH/ $\alpha$ -Fe <sub>2</sub> O <sub>3</sub>	Co-catalyst	PET hydrolysate	AM 1.5 G, 100 mW $\text{cm}^{-2}$	NaOH (1 M, pH 13.6)	FA: $\approx$ 87@1.1 $\text{V}_{\text{RHE}}$	$\approx$ 2/0.17@1.2 $\text{V}_{\text{RHE}}$	>12@1.1 $\text{V}_{\text{RHE}}$	9
	Co-catalyst	Sawdust-derived sugar	AM 1.5 G, 100 mW $\text{cm}^{-2}$	KOH (1 M)	FA: $\approx$ 90@1 $\text{V}_{\text{RHE}}$	$\approx$ 2/0.17@1.1 $\text{V}_{\text{RHE}}$	>100@1.0 $\text{V}_{\text{RHE}}$	18
Fe <sub>2</sub> O <sub>3</sub> /Ni(OH) <sub>x</sub>	Co-catalyst	PET hydrolysate (50 mM)	N/A	KOH (1 M)	FA: $\approx$ 100@1.2 $\text{V}_{\text{RHE}}$	$\approx$ 4/0.34@1.2 $\text{V}_{\text{RHE}}$	N/A	118
Fe <sub>2</sub> O <sub>3</sub> /m-CuO	Co-catalyst/ heterojunction	Glucose (20 mM)	AM 1.5 G, 100 mW $\text{cm}^{-2}$	NaOH (0.1 M)	FA: 97.3 $\pm$ 2.8@1.0 $\text{V}_{\text{RHE}}$	$\approx$ 0.8/0.07@1.2 $\text{V}_{\text{RHE}}$	>2@1.0 $\text{V}_{\text{RHE}}$	119
Fe <sub>2</sub> O <sub>3</sub>	N/A	Methanol (95% vol in water)	365 nm, 100 mW $\text{cm}^{-2}$	NaOH (0.1 M)	Formaldehyde: $\approx$ 100%@1.1 $\text{V}_{\text{RHE}}$	0.7/N.A. @0.55 $\text{V}_{\text{Ag}/\text{AgCl}}$	N/A	99
Ti-doped Fe <sub>2</sub> O <sub>3</sub>	Dopant	Polyimide ( $\approx$ 60 mg mL <sup>-1</sup> )	AM 1.5 G, 100 mW $\text{cm}^{-2}$	KOH (1 M)	N/A	$\approx$ 1.5/0.13@1.2 $\text{V}_{\text{RHE}}$	>4@1.2 $\text{V}_{\text{RHE}}$	120
<b>Other photoelectrodes</b>								
Bi <sub>2</sub> WO <sub>6</sub>	N/A	Glycerol (10% v/v)	$\lambda > 350$ nm, 120 mW cm <sup>-2</sup>	$\text{K}_2\text{SO}_4$ (0.1 M, pH 6)	N/A	0.69/0.22@1.3 $\text{V}_{\text{RHE}}$	N/A	121
CuWO <sub>4</sub>	Nanostructure	Glycerol (1 M)	AM 1.5 G, 100 mW $\text{cm}^{-2}$	Pi (0.1 M, pH 7)	GLAD: 60 $\pm$ 6, DHA: 30 $\pm$ 1@1.23 $\text{V}_{\text{RHE}}$	$\approx$ 0.6/0.07@1.23 $\text{V}_{\text{RHE}}$	>38 h@1.23 $\text{V}_{\text{RHE}}$	54
CoNiFe-LDH/ Ta <sub>3</sub> N <sub>5</sub>	Nanostructure/ Co-catalyst	Glycerol	AM 1.5 G, 100 mW $\text{cm}^{-2}$	NaOH (1.0 M)	FA: 60@ <sup>d</sup> 0 V	3.59/0.29@1.23 $\text{V}_{\text{RHE}}$	>0.5 h@ <sup>d</sup> 0 V	122

<sup>a</sup>  $\phi_{\text{PE}}$  is defined by the ratio of  $J_{\text{PE}}/J_{\text{max}}$ , where  $J$  is the measured photocurrent and  $J_{\text{max}}$  is the calculated theoretical photocurrent under 1 sun and AM 1.5 G, revealed in Fig. 5. <sup>b</sup> Defined as the time needed for the photocurrent to reach 60% of its respective initial photocurrent. <sup>c</sup> Operating at an external bias in a two-electrode system. <sup>d</sup> Operating at bias-free in a two-electrode system.

further effort. The long-term stability of PEC valorisation based on recently reported studies is further discussed in a later section.

**2.1.4 Scalability and earth-abundance.** Scalability is an essential factor in the practical consideration of a new technology.<sup>20</sup> Meeting scalability criteria should encompass material compositions, synthetic procedures and system designs. The ready accessibility of earth-abundant materials ensures a reliable supply chain, which is critical for scaling up production to meet global energy demands.<sup>57</sup> Rare elements in the earth's crust, including Pt, Re, Ru, Rh, Ir, Pd, Au, Ag, Ga, and In, are recommended for exclusion from PEC cells, as their scarcity might hinder scalability.<sup>58</sup> For example, the availability of Fe in the earth's crust is  $41 \times 10^3$  ppm, which is substantially higher than that of Pt ( $1 \times 10^{-3}$  ppm).<sup>59,60</sup> Therefore, the prices of precious metals are typically quoted per gram, whereas the cost of Fe is quoted per kilogram.<sup>61</sup> Furthermore, the use of abundant materials reduces dependence on intensive mining practices associated with precious metals, which are often environmentally damaging.<sup>62</sup>

**2.1.5 State-of-the-art photoelectrodes for PEC organic valorisation.** Since Honda and Fujishima demonstrated that TiO<sub>2</sub> could perform PEC water splitting under UV irradiation in 1972,<sup>15</sup> immense efforts have been devoted to exploring other materials for PEC reactions. Except for TiO<sub>2</sub>, the most widely investigated photoelectrode materials include WO<sub>3</sub>, BiVO<sub>4</sub>, and  $\alpha$ -Fe<sub>2</sub>O<sub>3</sub>. Their progress in PEC organic valorisation is briefly summarised in the following section.

TiO<sub>2</sub> has been widely investigated in PEC water splitting; however, the application of simple TiO<sub>2</sub> in PEC organic valorisation is relatively limited. TiO<sub>2</sub> generally exhibits low selectivity toward selected value-added chemicals in PEC organic valorisation (Table 2). Surface modification with a secondary material is generally required to achieve high selectivity. Inspiring examples include Bi<sub>2</sub>O<sub>3</sub> heterojunction with TiO<sub>2</sub> for glycerol valorisation to DHA,<sup>56</sup> ultrathin BiO<sub>x</sub>-covered TiO<sub>2</sub> converting succinic acid into C<sub>2</sub>H<sub>4</sub>,<sup>63</sup> and Bi<sub>2</sub>O<sub>3</sub>-modified TiO<sub>2</sub> converting cellulose into FA.<sup>64</sup>

Owing to its widespread application in the OER, the WO<sub>3</sub> photoanode has also been intensively studied in PEC organic valorisation in recent years (Table 2). Examples include the conversion of cyclohexane to KA oil (a mixture of cyclohexanol and cyclohexanone),<sup>65</sup> glycerol into value-added C<sub>3</sub> products,<sup>66</sup> and HMF to furandicarboxaldehyde (DFF) and FDCA.<sup>67</sup> The crystal structure and predominantly exposed facets of WO<sub>3</sub> also significantly affect the selectivity of PEC organic valorisation,<sup>68,69</sup> which are also discussed in a later section.

Like TiO<sub>2</sub> and WO<sub>3</sub>, BiVO<sub>4</sub> has been intensively investigated for PEC organic valorisation. Pioneering work on BiVO<sub>4</sub> for PEC biomass valorisation was reported by K.-S. Choi's group.<sup>70</sup> In the presence of 2,2,6,6-tetramethylpiperidine 1-oxyl (TEMPO), a faradaic efficiency (FE) of over 90% toward FDCA from HMF is achievable using BiVO<sub>4</sub> as the photoanode.<sup>70</sup> Beyond the valorisation of HMF, BiVO<sub>4</sub> has also been investigated for the PEC valorisation of lignin<sup>71,72</sup> and methanol,<sup>73</sup> and has been particularly well explored for glycerol valorisation (Table 2).<sup>55,74-76</sup>

$\alpha$ -Fe<sub>2</sub>O<sub>3</sub> has also shown great potential and has attracted considerable attention in PEC organic valorisation.  $\alpha$ -Fe<sub>2</sub>O<sub>3</sub> has been investigated in glycerol, glucose, cyclohexene, methanol, and EG valorisation (Table 2). In addition,  $\alpha$ -Fe<sub>2</sub>O<sub>3</sub> is particularly suitable for polymer-waste valorisation. Because depolymerisation of plastics by alkaline hydrolysis is generally required prior to PEC valorisation, the high stability of  $\alpha$ -Fe<sub>2</sub>O<sub>3</sub> in strongly alkaline solutions makes it the most frequently applied photoanode for plastic valorisation.

As mentioned in the previous section, most work on PEC organic valorisation has focused on earth-abundant photoanodes such as TiO<sub>2</sub>, WO<sub>3</sub>, and  $\alpha$ -Fe<sub>2</sub>O<sub>3</sub>. Given its extensive investigation in PEC reactions, BiVO<sub>4</sub> is also reviewed here, though Bi and V are not highly earth-abundant elements. Other earth-abundant photoelectrodes beyond those mentioned above, including CuWO<sub>4</sub>,<sup>77-79</sup> Ta<sub>3</sub>N<sub>5</sub>,<sup>80,81</sup> n-Si,<sup>82,83</sup> ZnO,<sup>84</sup> Cu<sub>2</sub>O,<sup>49,84</sup> and CuBi<sub>2</sub>O<sub>4</sub>,<sup>85-87</sup> have also been intensively studied for PEC water splitting; nevertheless, they have received significantly less, or no, attention in PEC valorisation (Table 2). For instance, CuWO<sub>4</sub>, an n-type semiconductor with a bandgap of 2.2 eV, is capable of utilising visible light up to approximately 550 nm to drive PEC oxidation reactions and exhibits chemical stability from acidic to slightly alkaline conditions.<sup>88,89</sup> Only recently has CuWO<sub>4</sub> been demonstrated as a versatile photoelectrode for converting glucose, fructose, and glycerol into several value-added chemicals, including FA, glycolate (the conjugate base of GLA), DHA, and GLAD.<sup>54</sup>

## 2.2 System and half-cell figures of merit

Solar-to-fuel energy conversion efficiency ( $\eta_{\text{STF}}$ ) is a critical performance indicator for systems used in solar water splitting and CO<sub>2</sub> reduction reactions, as it is broadly applicable to various designs of artificial photosynthesis systems.  $\eta_{\text{STF}}$  is determined by the ratio of the output energy of the solar fuel to the incident solar energy, as described in the following equation. Measurements are generally conducted under one-sun solar irradiation ( $1000 \text{ W m}^{-2}$ ) with a solar spectrum of Air Mass 1.5 Global (AM 1.5 G):

$$\eta_{\text{STF}} = \frac{R_{\text{product}}(\text{mol s}^{-1}) \times \Delta G(\text{J mol}^{-1})}{P_{\text{in}}(\text{W m}^{-2}) \times A(\text{m}^2)} \quad (5)$$

In eqn (5),  $R_{\text{product}}$  is the product generation rate,  $\Delta G$  is the Gibbs free energy change,  $P_{\text{in}}$  is the incident solar energy, and  $A$  is the geometric illuminated area. Specifically, for water splitting,  $\Delta G$  is  $237 \text{ kJ mol}^{-1}$  at  $25^\circ\text{C}$ , and the solar-to-hydrogen conversion efficiency ( $\eta_{\text{STH}}$ ) can be calculated using eqn (5) with this  $\Delta G$  value.

However, in PEC organic waste valorisation,  $\eta_{\text{STF}}$  values are generally low, regardless of  $R_{\text{product}}$ , due to the typically small  $\Delta G$ . In particular, some organic waste reactions have a negative  $\Delta G$ , which limits the applicability of  $\eta_{\text{STF}}$ . Given the substantial variation in  $\Delta G$  across different organic waste valorisation reactions, relying on  $\eta_{\text{STF}}$  would result in inequitable comparisons among solar-driven valorisation systems. As an alternative, areal activity ( $R_{\text{areal}}$ ) can serve as another indicator, providing



a unified quantification of product generation per unit of illuminated area and reaction time.<sup>1</sup>

$$R_{\text{areal}} = \frac{n_{\text{product}}(\text{mol})}{A(\text{m}^2) \times t(\text{h})} \quad (6)$$

Here,  $n_{\text{product}}$ ,  $A$ , and  $t$  represent the amount of product, the irradiated area, and the reaction time, respectively.

To recognize the economic value of each type of organic waste valorisation process, the solar-to-value (STV) creation rate ( $r_{\text{STV}}$ ) proposed by E. Reisner's group has been introduced:<sup>1</sup>

$$r_{\text{STV}} = \frac{\sum_i^n (C_i)(\text{£ per mol}) \times n_i(\text{mol}) - \sum_j^n (C_j + C_{\text{pt},j})(\text{£ per mol}) \times n_j(\text{mol})}{A(\text{m}^2) \times t(\text{h})} \quad (7)$$

where  $C_i$ ,  $C_j$ , and  $C_{\text{pt},j}$  are the costs of product  $i$ , substrate  $j$ , and its pre-treatment, respectively.

However, the cost of PEC cells should also be considered and is not negligible, particularly when noble metals are used in the composition of the photoelectrodes or when the synthesis of photoelectrodes involves arduous procedures. Therefore,  $r_{\text{STV}}$  is further modified as follows:

$$r_{\text{STV}} = \frac{\sum_i^n (C_i)(\text{£ per mol}) \times n_i(\text{mol}) - \sum_j^n (C_j + C_{\text{pt},j})(\text{£ per mol}) \times n_j(\text{mol}) - \sum_k^n (C_k + C_{\text{synth},k})(\text{£ per mol}) \times n_k(\text{mol})}{A(\text{m}^2) \times t(\text{h})} \quad (8)$$

In eqn (8),  $C_k$  and  $C_{\text{synth},k}$  refer to the cost of photoelectrode component and its synthesis, respectively. Although the  $r_{\text{STV}}$  might vary depending on the market conditions, it provides an essential indication of the economic value of PEC valorisation processes.

Although the  $\eta_{\text{STV}}$ ,  $R_{\text{areal}}$ , and  $r_{\text{STV}}$  parameters can be used to estimate the overall performance of an integrated PEC cell, additional indicators are necessary to evaluate half-cell performance. Since half-cell performance is predominantly governed by the intrinsic properties of the photoelectrodes, the inherent performance of a photoelectrode ( $\varphi_{\text{PE}}$ ) using the following equation is suggested for the assessment of the half-cell performance of a PEC cell:

$$\varphi_{\text{PE}} = \eta_{\text{LHE}} \times \eta_{\text{sep}} = \frac{J_{\text{PEC}}}{J_{\text{max}} \times \eta_{\text{int}}} \quad (9)$$

The  $\varphi_{\text{PE}}$  allows for the assessment of the intrinsic performance of a photoelectrode by neglecting reaction substrates in a PEC system. It could be a promising indicator for comparing the performance of a PEC cell using the same photoelectrode for

different organic valorisation reactions. The  $\eta_{\text{int}}$  generally deviates from unity during water oxidation due to its sluggish kinetics. However,  $\eta_{\text{int}}$  can be assumed to be unity, as most photoelectrodes provide significantly greater driving force than that required for water oxidation. Table 2 summarises the key parameters of reported PEC organic valorisation systems and categories of photoelectrodes based on their composition and modification methods. The  $\varphi_{\text{PE}}$  in Table 2 is calculated using eqn (9) and assuming  $\eta_{\text{int}}$  is unity.

The FE and power-saved metrics are advantageous for comparing the performance of different photoelectrodes under the same PEC organic valorising reaction. FE, defined as the percentage of passed charge used in the desired reaction, is an essential metric for evaluating selectivity in both EC and PEC systems. FE can be described by the following reaction:

$$\text{FE}(\%) = \frac{z \times 96\,485(\text{C mol}^{-1}) \times n_i(\text{mol})}{Q(\text{C})} \times 100 \quad (10)$$

where  $z$  is the electron transfer number required per mole of the specific product, 96 485 is the Faraday constant,  $n_i$  is the number of moles of the generated specific product ( $i$ ), and  $Q$  is the amount of charge passed during the PEC reaction.

Some literature presents selectivity using the ratio of the amount of a desired product to the total amount of product or the ratio of the amount of a desired product to the amount of substrate. If there is an unknown product, it will lead to a deviation using the former method, while the selectivity can be enhanced within a specific reaction time by lowering the initial amount of substrate using the latter method. Therefore, these two types of selective presentations may not be sufficiently objective, and FE will be used primarily in the discussion about selectivity.

Power-saved metrics enable the evaluation of the effects of input solar illumination on a half-cell.<sup>90</sup> In a three-electrode system, the power stored at a specific current density  $I$  ( $P_{\text{save}}(-I)$ ,  $\text{W m}^{-2}$ ) is derived by the product of the current density  $I$  and



the potential difference of driving a half-reaction at current density  $I$  between a selected working electrode in the dark and a photoelectrode in the light:

$$P_{\text{saved}}(I) = I(\text{A m}^{-2}) \times (E_{\text{dark}}(I) - E_{\text{light}}(I)(\text{V})) \quad (11)$$

The  $E_{\text{dark}}(I)$  and  $E_{\text{light}}(I)$  are the potential of driving a half-reaction at current density  $I$  of the dark electrode and photoelectrode, respectively.

### 2.3 Comparison of electrochemical (EC) and PEC organic valorisation

In addition to PEC organic valorisation, EC organic valorisation has also been demonstrated to convert organic waste into fuel and value-added chemicals. In EC systems, the energy required to drive the reaction relies on the external bias, and the catalytic current increases monotonically with the applied overpotential until it becomes limited by mass transfer. In contrast, in PEC systems, the photocurrent reaches a saturation plateau at a certain potential when the photogenerated electrons are fully extracted. Thus, EC systems typically achieve higher current

densities at high overpotentials compared to PEC systems, particularly if PEC systems are operated under low photon flux conditions, such as one-sun illumination. For example, the EC system of nickel-modified cobalt phosphide on nickel foam ( $\text{CoNi}_{0.25}\text{P}/\text{NF}$ ) has been demonstrated to exhibit an electrocatalytic current for EG oxidation with an onset potential of approximately  $1.2 \text{ V}_{\text{RHE}}$ , and its current significantly increases with the applied potential, reaching approximately  $180 \text{ mA cm}^{-2}$  at  $1.35 \text{ V}_{\text{RHE}}$  (Fig. 6a).<sup>91</sup> On the other hand, a  $\text{BiVO}_4/\text{NiCo-LDH}$  photoanode exhibits a much lower saturation photocurrent of approximately  $2 \text{ mA cm}^{-2}$  for EG oxidation under one-sun illumination, *i.e.*  $100 \text{ mW cm}^{-2}$  (Fig. 6b).<sup>92</sup> However, the external bias required in the PEC system is typically smaller than that of the EC system due to the presence of a light-induced photovoltage, resulting lower energy consumption in the PEC system at low overpotential regions. In the case of  $\text{BiVO}_4/\text{NiCo-LDH}$ , the photocurrent for EG valorisation starts from  $0.2 \text{ V}_{\text{RHE}}$ , which is much lower than the onset potential ( $1.2 \text{ V}_{\text{RHE}}$ ) of the  $\text{CoNi}_{0.25}\text{P}/\text{NF}$  EC system. The amount of energy saved by using a photoelectrode can be readily evaluated using eqn (11). In addition, the drawback of the low saturation photocurrent density of a photoelectrode can potentially be mitigated by using concentrated solar light as the light source<sup>93</sup> or by incorporating the thermoelectric effects.<sup>93,94</sup>

The advantages of using a PEC system over an EC system can be highlighted by the work on glycerol valorisation in a membrane-separated continuous-flow PEC cell reported in 2024.<sup>95</sup> In this work, direct PEC oxidation of glycerol paired with the dark  $\text{H}_2$  evolution or  $\text{CO}_2$  reduction was achieved using a Si photoanode coupled with a silver nanoparticle-coated carbon cloth cathode. On the other hand, in the EC system, a Ni sheet was used as the anode. Intense sunlight of up to 10 suns was applied to the PEC cell, and a photocurrent exceeding  $110 \text{ mA cm}^{-2}$  was achieved for glycerol oxidation (Fig. 7a). Compared to the EC cell, the PEC cell required less energy input from the external voltage source to attain the same current density (Fig. 7b). Approximately 1 V less cell voltage was needed for the PEC cell compared to the EC cell to generate a current density of  $100 \text{ mA cm}^{-2}$  (Fig. 7b). Notably, this study also demonstrated

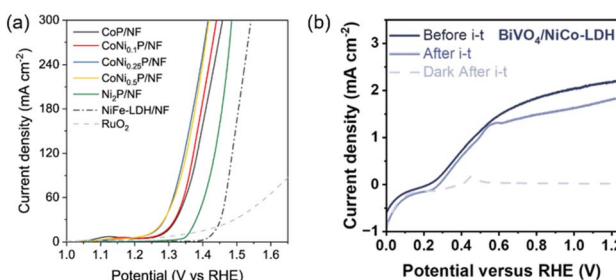


Fig. 6 (a) Linear sweep voltammetry (LSV) curves for EC oxidation using  $\text{CoNi}_{0.25}\text{P}/\text{NF}$  and other electrocatalysts. Reproduced with permission under the terms of a CC BY 4.0 license.<sup>91</sup> Copyright 2021, The Author(s), published by Springer Nature. (b) Photocurrent (solid lines) of  $\text{BiVO}_4/\text{NiCo-LDH}$  before and after  $i$ - $t$  measurements in an EG containing KOH solution. Reproduced with permission.<sup>92</sup> Copyright 2024, John Wiley and Sons.

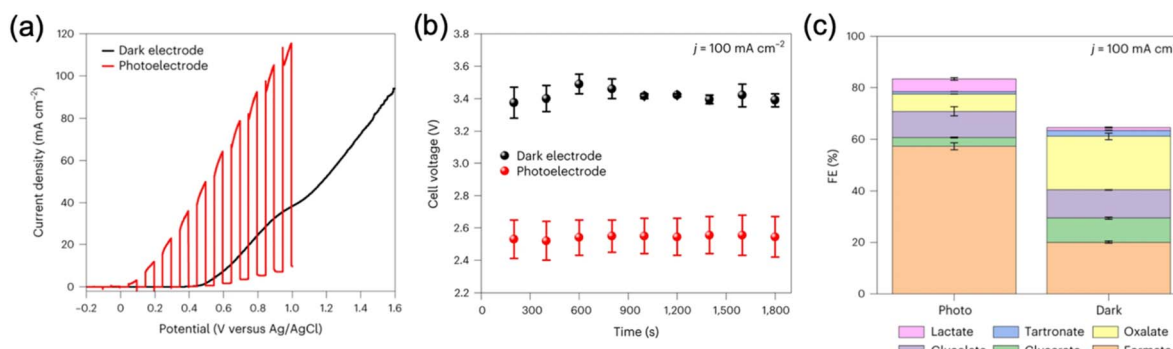


Fig. 7 (a) LSV of a Ni/Si photoanode under chopped light illumination and a Ni sheet-based electrode in the dark for glycerol oxidation. (b) Cell voltage difference between the Ni/Si photoanode and the Ni sheet-based anode at a current density of  $100 \text{ mA cm}^{-2}$  for glycerol oxidation. (c) FE of glycerol oxidation products after 30 min at a current density of  $100 \text{ mA cm}^{-2}$ . Reproduced with permission under the terms of a CC BY 4.0 license.<sup>95</sup> Copyright 2024, The Author(s), published by Springer Nature.



that the product distribution of glycerol oxidation in the PEC cell differs from that of the EC cell at the same current density (Fig. 7c). The FE for value-added products was higher in the PEC cell than in the EC cell ( $\approx 82\% \text{ vs. } \approx 63\%$ ). Oxygen quantification experiments confirmed that the PEC system can effectively suppress the parasitic OER. This difference may arise from the inherent discrepancy in potential dependence between PEC and EC systems. The oxidative force in the EC system depends on the applied potential, whereas in the PEC system, it is determined and fixed by the  $E_{VB}$  position and is independent of the applied potential.

Nonetheless, the PEC system undergoes complex charge transfer processes, beginning with the extraction of photo-generated charges, followed by hole transfer to the semiconductor surface, and subsequently to the organic reactant. Therefore, an effective photoelectrode design that facilitates rapid charge transfer is necessary for PEC organic valorisation.

#### 2.4 Kinetics of PEC reactions

PEC reactions that involve multiple steps of charge transfer are typically kinetically challenging, and the reaction kinetics play a critical role in determining both efficiency and selectivity. For example, OER in water splitting is generally considered the bottleneck, as it involves a four-electron transfer process, and its sluggish kinetics constrain the overall efficiency of water splitting. Many organic valorisation reactions listed in Table 1 also involve multiple charge transfer steps, and various products may be formed during the process. Research into PEC reaction kinetics is therefore essential for advancing the development of PEC organic valorisation.

The rate law analysis on  $\alpha\text{-Fe}_2\text{O}_3$  for PEC water oxidation was first demonstrated by Le Formal *et al.*<sup>96</sup> Photoinduced absorption (PIA) spectroscopy combined with transient photocurrent (TPC) measurements was employed to elucidate the quantitative relationship between the reaction rate and the accumulation of photogenerated holes on the  $\alpha\text{-Fe}_2\text{O}_3$  surface.<sup>96</sup> PIA enables monitoring of long-lived photogenerated charge carriers, *i.e.*, surface hole density for the photoanode, while TPC monitors the net flux of holes transferred to the electrolyte. The reaction kinetics under steady-state PEC oxidation conditions was then estimated by rate law analysis (eqn (12)).<sup>96–98</sup>

$$J = k_r[\text{hole}]^\beta \quad (12)$$

where  $J$  represents the photocurrent density,  $k_r$  represents the reaction rate constant,  $[\text{hole}]$  is the density of accumulated surface holes, and  $\beta$  represents the reaction order.

It was found that a transition occurs from a first-order reaction at low densities of accumulated surface holes (slow reaction) to a third-order reaction at high densities of accumulated surface holes (fast reaction), indicating that the accumulation of multiple holes is required to drive water oxidation efficiently over  $\alpha\text{-Fe}_2\text{O}_3$ .<sup>96</sup>

In addition to PIA, the rate law analysis can also be conducted using EC impedance spectroscopy (EIS) measurement. Zhang *et al.* determined the surface hole density on the  $\alpha\text{-Fe}_2\text{O}_3$  photoanode using this EIS measurement and subsequently

correlated it with the photocurrent density to calculate the reaction order of water oxidation.<sup>97</sup> They found that the reaction order was approximately 1 and 2 for water oxidation in near-neutral and alkaline conditions, respectively, highlighting the dependency of the water oxidation reaction order on the solution pH.

Shifting the focus toward PEC organic valorisation, PIA coupled with TPC measurements has also been applied to derive the kinetic parameters and elucidate the mechanism of PEC alcohol oxidation.<sup>99,100</sup> Mesa *et al.* found that methanol, when PEC oxidised to formaldehyde on  $\alpha\text{-Fe}_2\text{O}_3$  photoanodes, followed a second-order reaction with rate orders of 1.88 and 1.89 at applied potentials of 0 V *vs.* Ag/AgCl ( $V_{\text{Ag/AgCl}}$ ) and 0.55 V  $V_{\text{Ag/AgCl}}$ , respectively (Fig. 8a).<sup>99</sup> They confirmed that the rate order on  $\alpha\text{-Fe}_2\text{O}_3$  is determined solely by the density of holes accumulated at the surface of the photoelectrode and is independent of the applied potential. This observation corresponds to the earlier discussion comparing EC and PEC systems. In contrast to EC systems (Section 2.3), in which the oxidative force varies with the applied potential, the energy, *i.e.*, the oxidative force of the holes, in a PEC system is determined by the  $E_{VB}$  of photoanodes.

It has been found that  $\alpha\text{-Fe}_2\text{O}_3$  exhibits highly selective aldehyde production through PEC alcohol oxidation.<sup>99,100</sup> The underlying reason was also elucidated by *operando* spectroelectrochemical PIA coupled with TPC, in parallel with the Arrhenius analyses.<sup>100</sup> Rate law analyses suggest that  $\alpha\text{-Fe}_2\text{O}_3$  exhibits a second-order reaction for ethanol oxidation, while the reaction order of PEC acetaldehyde oxidation on  $\alpha\text{-Fe}_2\text{O}_3$  is only 0.5 (Fig. 8b). Temperature-dependent rate law analyses further demonstrated that activation energy for ethanol oxidation by photogenerated holes in  $\alpha\text{-Fe}_2\text{O}_3$  is much lower than that for acetaldehyde oxidation (195 vs. 398 meV). These results indicate that the high selectivity for aldehyde production on  $\alpha\text{-Fe}_2\text{O}_3$  results from its much more facile kinetics toward ethanol oxidation compared to acetaldehyde oxidation, which suppresses the overoxidation of acetaldehyde. Compared to  $\alpha\text{-Fe}_2\text{O}_3$ ,  $\text{TiO}_2$  exhibits only a modest selectivity toward

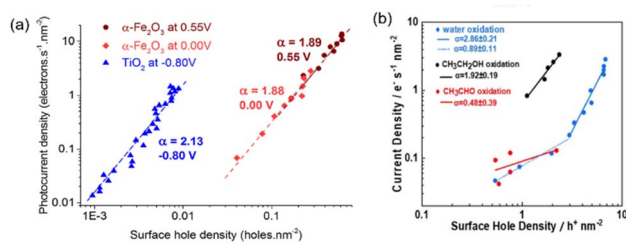


Fig. 8 (a) Rate law analyses showing the reaction order of PEC methanol oxidation on  $\alpha\text{-Fe}_2\text{O}_3$  at 0.55 V<sub>Ag/AgCl</sub> (dark red) and 0.00 V<sub>Ag/AgCl</sub> (light red), and on  $\text{TiO}_2$  at  $-0.80$  V<sub>Ag/AgCl</sub> (blue). Reproduced with permission under the terms of a CC BY 4.0 license.<sup>99</sup> Copyright 2017, American Chemical Society. (b) Rate law analyses showing the reaction order of PEC water oxidation at 1.3 V<sub>RHE</sub> (blue), ethanol oxidation at 1.2 V<sub>RHE</sub> (black), and acetaldehyde oxidation at 1.1 V<sub>RHE</sub> (red) on  $\alpha\text{-Fe}_2\text{O}_3$ . Reproduced with permission.<sup>100</sup> Copyright 2022, John Wiley and Sons.



acetaldehyde production, and overoxidation of acetaldehyde was observed. The disparate selectivity toward acetaldehyde production from ethanol over different metal oxide photo-electrodes is correlated with their varying  $E_{VB}$ .<sup>101</sup> The measured acetaldehyde oxidation activation energies are 45 and 427 meV, respectively, for photogenerated holes in  $TiO_2$  and  $\alpha\text{-Fe}_2\text{O}_3$ . The study highlights the significance of band potential in determining the selectivity of PEC organic valorisation.

Understanding reaction kinetics in PEC systems can guide the design of photoanodes for PEC organic valorisation, emphasising the importance of achieving a high density of accumulated holes and ensuring the suitability of the  $E_{VB}$  for a photoanode. This can be achieved by designing photo-electrodes with a suitable electronic band structure, increasing the intensity of illumination using concentrated solar light, tuning hole densities through doping, modifying co-catalysts, nanostructuring, and creating heterojunctions. Strategies for enhancing the performance of photoanodes for organic valorisation is further discussed in Section 4.

### 3. Polymeric organic waste and pre-treatment process

Biomass and plastic are the major organic substrates of interest in PEC valorisation. Glycerol, glucose, and HMF are among the most widely studied biomass-derived platform molecules in PEC organic valorisation, while EG is the most extensively investigated plastic-derived molecule. However, some of these molecules originate from the depolymerisation of natural and synthetic polymeric waste. A pre-treatment process of reducing crystallinity or depolymerising polymeric organic waste is generally required to enhance reforming efficiency.

#### 3.1 Natural polymer waste

Biomass is a naturally synthesised polymer that primarily contains lignocellulose, proteins, and lipids, with lignocellulose being its main constituent and an earth-abundant resource.<sup>123,124</sup> Lignocellulose is the most abundant biomass and is readily found in wood stems, nut shells, corn cobs, grasses, and rice husks,<sup>125,126</sup> consisting of three major components: cellulose, hemicellulose, and lignin. Cellulose and hemicellulose are composed of long chains of sugars. The general chemical formula for cellulose is  $(C_6H_{12}O_5)_n$ , in which glucose-based monomers are linked *via*  $\beta\text{-}1,4$ -glycosidic bonds.<sup>127</sup> Hemicellulose is a copolymer composed of five sugar monomers: D-xylose, L-arabinose, D-galactose, D-glucose, and D-mannose.<sup>128</sup> In contrast, lignin is composed of three hydrophobic units: *p*-coumaryl, coniferyl alcohol, and sinapyl alcohol.<sup>129</sup> The polar nature and high hydroxyl content of cellulose and hemicellulose enable their application in reforming reactions following a depolymerisation pre-treatment, whereas lignin presents a challenge due to its recalcitrant structure. On the other hand, proteins such as amino acids and lipids such as glyceride and fatty acid are found in algae and wood wastes.<sup>124</sup>

#### 3.2 Synthetic polymer waste

Affordability, lightweight nature, and versatility make plastics indispensable in human life. However, the high stability and durability of plastics result in prolonged degradation times. Significant “white pollution” is caused by the widespread use of plastics without a proper circular economy. Polyethylene (PE), PET, polystyrene (PS), polypropylene (PP), poly (vinyl chloride) (PVC), polylactic acid (PLA), and polyurethane (PU) are the primary types of plastics employed in daily life.<sup>30,130</sup> These plastics are classified into two groups based on the type of bond in the main chain and the synthetic methods used.<sup>30,130</sup>

(a) The first group, PE, PS, PP, and PVC, is composed of C–C bonds in the main chain and is synthesised *via* addition polymerisation. The high stability of these hydrocarbon chains limits their applicability in reforming reactions.

(b) The second group, comprising PET, PLA, and PU, features C–O or C–N bonds in the backbone chain and is synthesised *via* condensation polymerisation. Oxygenated plastics account for approximately 15% of global primary plastic production.<sup>131</sup> Owing to their polarity and ester bonds, they are typically the target substrates in solar-driven plastic reforming.<sup>7,132</sup>

#### 3.3 Pre-treatment of polymeric organic waste

The hydrogen bonding or crosslinking features within polymeric waste restricts their solubility in aqueous solution. A pre-treatment process that reduces crystallinity or depolymerises polymeric organic waste is generally required to enhance reforming efficiency. An effective pre-treatment method must be scalable, cost-effective, and capable of yielding a high amount of monomer components. Various pre-treatment technologies, ranging from conventional to green approaches, are used to solubilise organic waste. However, the scope of this section is to summarise the primary pre-treatment technologies used in solar-driven valorisation and to discuss their respective advantages and challenges. The pre-treatment processes are categorised into three major types.

**3.3.1 Physical pre-treatment.** Physical pre-treatment is principally a mechanical approach employed to reduce the size and crystallinity of the polymer. This increases porosity and creates additional surface area for polymers undergoing hydrolysis. Physical pre-treatment includes milling, grinding, refining, ultrasonication, and extrusion.<sup>133</sup> The application of physical pre-treatment in solar-driven polymer waste reforming is relatively limited compared to chemical pre-treatment. A rare example demonstrates that ball milling effectively decreases the crystallinity of  $\alpha$ -cellulose, which significantly enhances the efficiency of the subsequent photocatalytic cellulose reforming.<sup>134</sup> The advantage of physical pre-treatment is that it does not require the use of corrosive chemicals, and it can be applied across a wide range of reforming environments. However, physical pre-treatments only reduce the size and crystallinity of polymers rather than depolymerising wastes into monomers, which may limit their efficiency in the subsequent solar-driven valorisation process.

**3.3.2 Chemical pre-treatment.** Chemical hydrolysis in alkaline or acidic solutions, steam explosion, and biological

treatment have been demonstrated to facilitate C–C cleavage.<sup>30,32,132</sup> Among these, alkaline and acid hydrolysis have a more straightforward setup than the others. Alkaline hydrolysis is a suitable method to convert some plastic polymers into their monomers.<sup>31,135</sup> For example, PET can be depolymerised into terephthalate and EG monomers in 10 M NaOH solution.<sup>32</sup> PLA has been depolymerised into lactate in 10 M KOH.<sup>136</sup> Meanwhile, acid hydrolysis, such as with dilute nitric acid, is used to depolymerise PE into glutaric and succinic acids.<sup>136</sup> Nonetheless, these chemical hydrolysis pre-treatments in biomass and waste plastic involve harsh operating conditions, such as the use of corrosive solutions, either strong bases (*i.e.*, the concentration of OH<sup>–</sup> (5–10 M)) or strong acids (*i.e.*, sulfuric and nitric acids). This results in high energy consumption for separation, safety hazards for handling, and the generation of toxic secondary pollutants. Moreover, the use of extreme pH in the pre-treatment process is frequently incompatible with the subsequent steps, *i.e.*, the photoelectro-oxidation or photoelectro-reduction, which require benign operating conditions. Very recently, catalyst-assisted depolymerisation has been demonstrated under much lesser corrosive conditions. For example, PET was depolymerised in 0.1 M NaOH solution containing binuclear zinc molecular (Zn<sub>2</sub>-complex) catalyst at 60 °C, achieving approximately 100% conversion within 48 h.<sup>137</sup>

**3.3.3 Biological pre-treatment.** Beyond synthesized catalysts, natural catalysts, *i.e.*, enzymes, have also been investigated and applied in solar-driven polymer waste valorisation. Reisner and co-workers demonstrated enzyme-pretreated cellulose under mild conditions in sodium acetate (pH 5)<sup>138,139</sup> or sodium bicarbonate solution (pH 6.5)<sup>140</sup> at 37 °C for 24 h to generate glucose and cellobiose. In addition, their group also demonstrated depolymerisation of polycaprolactone and PET using enzyme, *i.e.*, DuraPETase (Dura) and leaf-compost cutinase (LCC), in carbonate buffer solutions (pH 8) at 37 °C (Dura) and 65 °C (LCC) for 2 days.<sup>141</sup> Biological pre-treatments generally operate under environmentally benign conditions and do not require toxic chemicals. However, the challenges of biological pre-treatment include prolonged reaction time and the vulnerability of some enzymes to environmental conditions.

## 4. PEC oxidation for organic electrosynthesis: strategies to enhance the performance of photoanodes

Optimising the design of photoelectrode is essential not only for enhancing the conversion rate of solar energy into chemical energy but also for achieving efficient, selective, and robust PEC valorisation of organic waste. Several photoelectrodes are constrained by limited light absorption and high recombination of photo-generated electrons and holes. The limitation in light absorption is due to the wide bandgap. Photo-generated charge recombination primarily results from the intrinsic low conductivity and short minority carrier diffusion length of the semiconducting materials. Sluggish interfacial transfer of photo-generated holes further contributes to surface recombination.<sup>142,143</sup> Several key strategies have been demonstrated to

mitigate recombination without compromising the light-harvesting capability of the photoelectrodes. These strategies include doping, heterojunction, and nanostructuring. On the other hand, co-catalyst modification and crystal facet engineering effectively enhance the selectivity of the target products in organic waste valorisation. The aforementioned strategies used in PEC oxidation for organic electrosynthesis are summarised and discussed in the following sections.

### 4.1 Doping

Doping offers a viable method for effectively modulating the electronic structure and properties of photoelectrodes.<sup>144</sup> Doping may regulate the bandgap structure by altering the positions of  $E_{VB}$  and  $E_{CB}$ , thereby extending light absorption into the visible range. Additionally, electronic states are introduced, including donor levels below the  $E_{CB}$  and/or acceptor levels above the  $E_{VB}$ .<sup>145</sup> In particular, doping is an effective strategy to eliminate significant charge recombination by enhancing carrier mobility and density or internal electric field in a photoelectrode.

The suppression of charge recombination by enhancing the internal electric field has been recently demonstrated to boost the performance of a photoelectrode in organic valorisation. Kong *et al.* introduced nitrogen into WO<sub>3</sub> (N-WO<sub>3</sub>) to enhance the PEC valorisation of polyol biomass into CO.<sup>110</sup> Density functional theory (DFT) calculation revealed that nitrogen doping regulates the electronic structure polarity by creating an asymmetric distribution of charge (Fig. 9a). The asymmetric distribution of charge enhances the internal electric field, effectively preventing the recombination of charge carriers. As a result, N-WO<sub>3</sub> exhibited a higher photocurrent density in PEC glycerol valorisation than pristine WO<sub>3</sub> (Fig. 9b). N-WO<sub>3</sub> presented a higher CO evolution rate than WO<sub>3</sub> at a similar CO selectivity throughout the voltage range of 0.4–0.9 V<sub>RHE</sub> (Fig. 9c and d). N-WO<sub>3</sub> also exhibited promising long-term stability in an acidic solution (0.5 M Na<sub>2</sub>SO<sub>4</sub>, pH 1), with around 80% selectivity towards CO, 40% CO FE, and 10% carbon yield after 50 h (Fig. 9e). The excellent stability was attributed to the absence of any phase or structural changes during the PEC process. Similarly, Kim *et al.* demonstrated an enhancement in PET microplastic valorisation over  $\alpha$ -Fe<sub>2</sub>O<sub>3</sub> by Zr doping (Zr: $\alpha$ -Fe<sub>2</sub>O<sub>3</sub>).<sup>146</sup> PET microplastic was obtained by grinding commercial PET into microplastic ( $\leq 5$  mm), followed by immersion in 5 M NaOH for 3 days at 80 °C to obtain EG. Zr doping served as an electron donor, accelerating electron transport kinetics and promoting more upward band bending. Zr: $\alpha$ -Fe<sub>2</sub>O<sub>3</sub> exhibited a faster production rate of FA and acetate compared to  $\alpha$ -Fe<sub>2</sub>O<sub>3</sub>. Moreover, Zr: $\alpha$ -Fe<sub>2</sub>O<sub>3</sub> demonstrated excellent long-term stability over seven cycles, each lasting 12 h. Notably, there was no change in phase or surface oxidation state after the cycling test, and no metal leaching was observed, indicating excellent structural and chemical stability.

Beyond regulating the photocurrent of the pristine photoelectrode, increasing the selectivity for the target product and enhancing stability can also be realised by incorporating a suitable dopant. The enhancement of photocurrent, selectivity



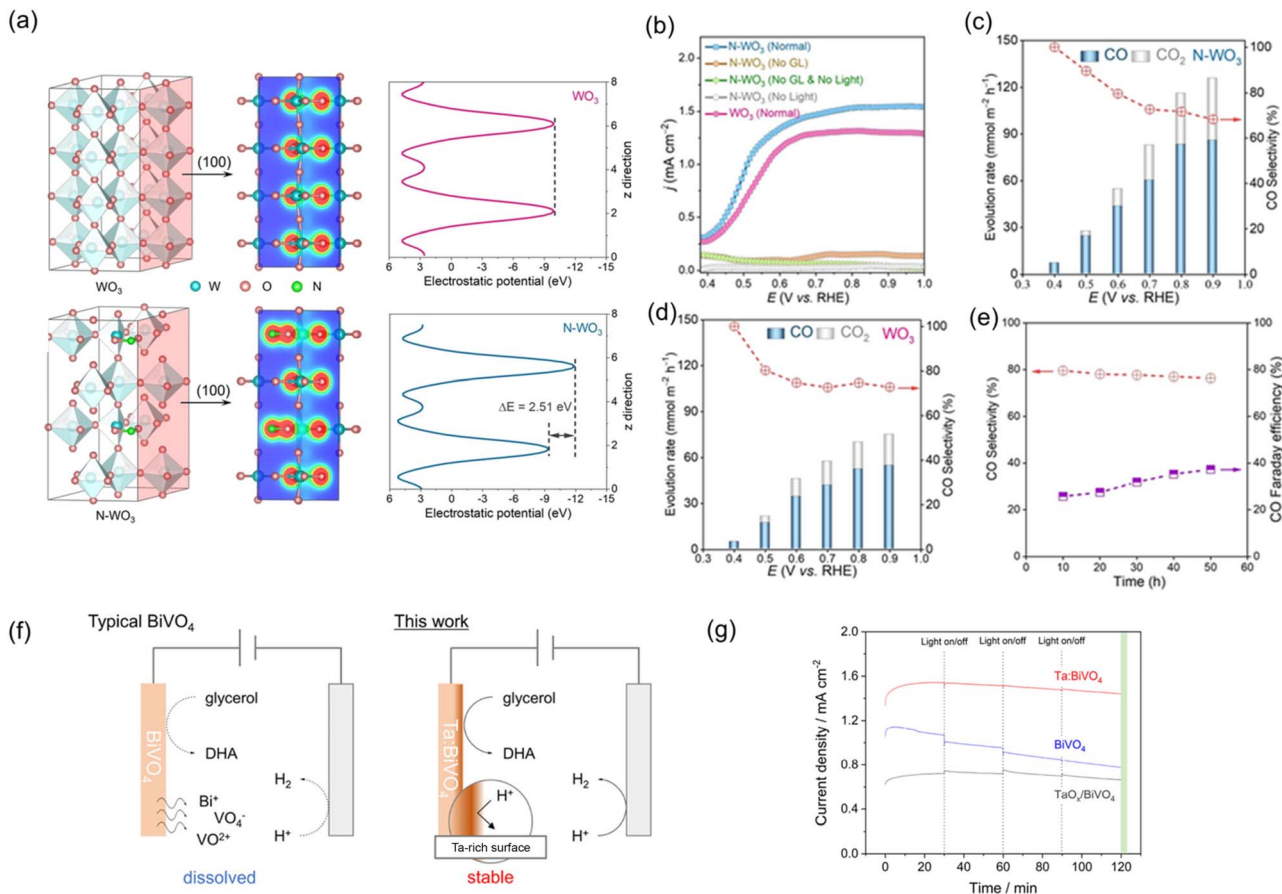


Fig. 9 (a) Calculated isosurface of electron density and electrostatic potential of  $\text{WO}_3$  and  $\text{N-WO}_3$ . (b) LSV curves of  $\text{N-WO}_3$  in the absence and presence of glycerol under dark or light irradiation. Evolution rate and CO selectivity of (c)  $\text{N-WO}_3$  and (d)  $\text{WO}_3$ . (e) Long-term stability of PEC glycerol oxidation toward CO generation at  $0.6 \text{ V}_{\text{RHE}}$ . Reproduced with permission.<sup>110</sup> Copyright 2022, John Wiley and Sons. (f) Schematic of PEC glycerol oxidation over  $\text{BiVO}_4$  and  $\text{Ta:BiVO}_4$  in acidic medium. (g) Long-term stability of PEC glycerol oxidation over  $\text{BiVO}_4$ ,  $\text{Ta:BiVO}_4$ , and  $\text{TaO}_x/\text{BiVO}_4$  at  $1.0 \text{ V}_{\text{RHE}}$ . Reproduced with permission.<sup>112</sup> Copyright 2022, American Chemical Society.

of DHA in PEC glycerol oxidation, and immunity to the dissolution in an acidic medium were achieved through Ta doping of  $\text{BiVO}_4$  ( $\text{Ta:BiVO}_4$ ), as shown in Fig. 9f and g.<sup>112</sup> Doping with Ta in  $\text{BiVO}_4$  was found to effectively enhance the photocurrent density and FE of DHA from  $1.70$  to  $3.07 \text{ mA cm}^{-2}$  at  $1.23 \text{ V}_{\text{RHE}}$  and from  $41\%$  to  $61\%$ , respectively. In terms of stability,  $\text{BiVO}_4$  retained only approximately  $70\%$  of the photocurrent in the acidic solution after  $2 \text{ h}$  of operation during glycerol oxidation. In contrast, both  $\text{Ta:BiVO}_4$  and  $\text{TaO}_x$ -coated  $\text{BiVO}_4$  ( $\text{TaO}_x/\text{BiVO}_4$ ) remained stable in photocurrent during  $2 \text{ h}$  PEC glycerol valorisation. These results confirm that the presence of Ta or  $\text{TaO}_x$  on the surface of  $\text{BiVO}_4$  protects  $\text{BiVO}_4$  from dissolution in an acidic medium, thus providing high stability.

## 4.2 Heterojunction

The concept of a semiconductor-semiconductor heterojunction configuration is employed to prevent the recombination of photo-generated charges and accelerate the charge transfer driven by a built-in electric field.<sup>147,148</sup> In some cases, the guest semiconductor is selected to have a narrower bandgap than the host semiconductor to extend the utilisation of photons in the

solar light spectrum. The selectivity might also be tuned by altering the catalytic kinetics, oxidation potentials, or reaction routes through the appropriate selection of the heterojunction layer. Heterojunctions can be categorised into three conventional types according to their band alignment between the two semiconductors: straddling-gap (type-I), staggered-gap (type-II), and broken-gap heterojunctions (type-III).<sup>149</sup> However, only type-II heterojunction can promote spatial charge separation, thereby eliminating charge recombination.<sup>150</sup> The charge separation in a type-II heterojunction is realised by the photo-generated electrons in semiconductor B transporting to semiconductor A, while the photo-generated holes follow the reverse route. The junctions can be further divided into n-n junctions, p-p junctions, or p-n junctions based on the conductivity features of the semiconductors.

PEC organic waste valorisation is typically performed in water, and the OER inevitably occurs as a side reaction if the photo-generated holes possess sufficient oxidative force toward OER. As previously mentioned, organic oxidation in common valorisation studies generally requires less oxidative force than OER. Selecting a guest semiconductor with insufficient  $E_{\text{VB}}$  to oxidise water can eliminate the OER side reaction during PEC



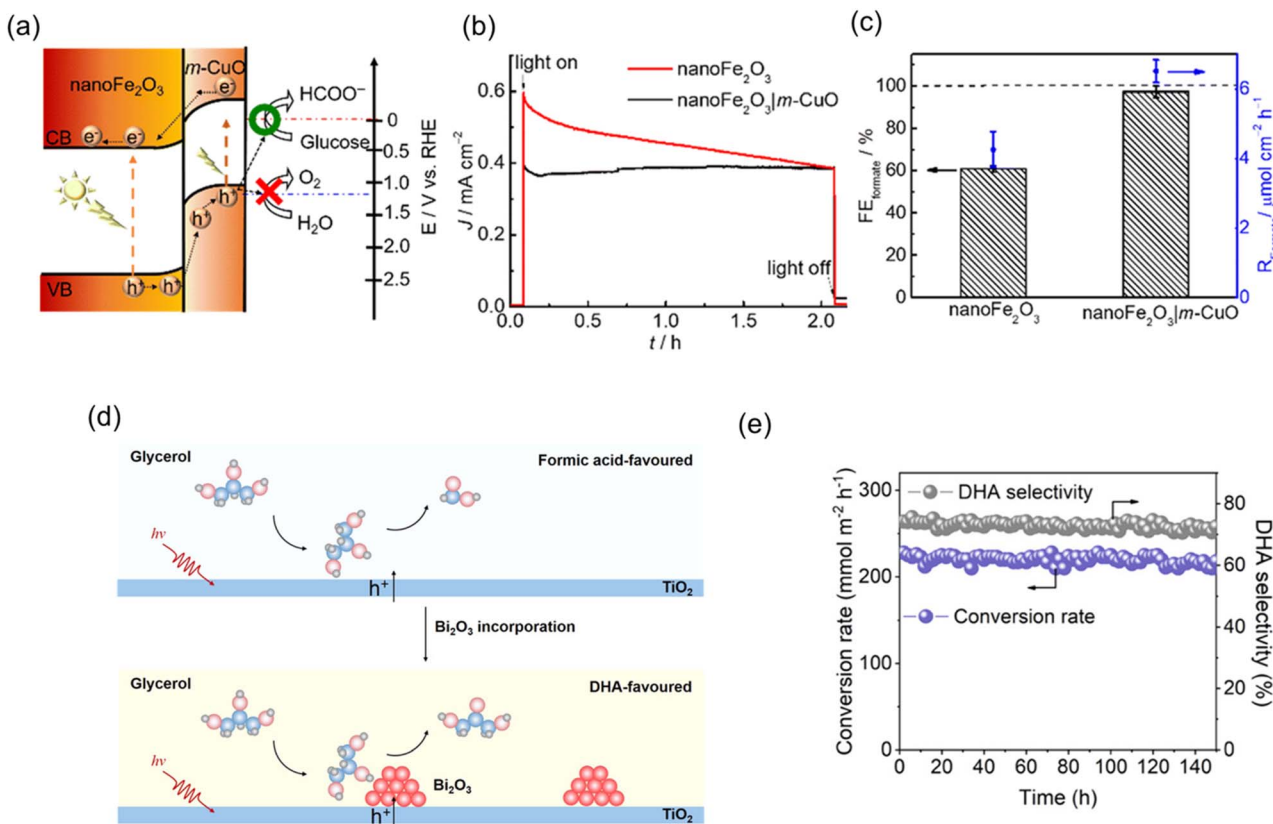


Fig. 10 (a) Band diagram of the  $\text{nanoFe}_2\text{O}_3|m\text{-CuO}$ . (b) CPE measurements of  $\text{nanoFe}_2\text{O}_3$  and  $\text{nanoFe}_2\text{O}_3|m\text{-CuO}$ , and (c) their corresponding FE and production rate of FA in 0.1 M NaOH with 20 mM glucose under solar light irradiation (AM 1.5 G, 100  $\text{mW cm}^{-2}$ ). Reproduced with permission.<sup>119</sup> Copyright 2022, Royal Society of Chemistry. (d) Schematic of PEC glycerol oxidation over  $\text{TiO}_2$  and  $\text{Bi}_2\text{O}_3/\text{TiO}_2$  heterojunction and (e) long-term stability test of  $\text{Bi}_2\text{O}_3/\text{TiO}_2$  photoanode for PEC glycerol oxidation. Reproduced with permission.<sup>56</sup> Copyright 2022, American Chemical Society.

organic compound valorisation. Chuang *et al.* constructed a type-II p-n heterojunction of  $\text{nanoFe}_2\text{O}_3$  and CuO as a  $\text{nanoFe}_2\text{O}_3|\text{CuO}$  photoanode for PEC glucose oxidation into FA.<sup>119</sup> With regard to the  $E_{\text{VB}}$  position of  $\text{nanoFe}_2\text{O}_3$ , there is competition between OER and glucose oxidation. The incorporation of CuO effectively inhibits the OER side reaction because of the insufficient driving force of holes on its  $E_{\text{VB}}$ . Additionally, CuO is an efficient catalyst for glucose valorisation to FA and also acts as a co-catalyst in the  $\text{nanoFe}_2\text{O}_3|\text{CuO}$  heterojunction photoelectrode, promoting FA formation (Fig. 10a). The  $\text{nanoFe}_2\text{O}_3|\text{CuO}$  outperformed  $\text{nanoFe}_2\text{O}_3$  by exhibiting a stable photocurrent density, while  $\text{nanoFe}_2\text{O}_3$  exhibited a 33% decay photocurrent density after 2 h of operation (Fig. 10b). Furthermore,  $\text{nanoFe}_2\text{O}_3|\text{CuO}$  also exhibited nearly 100% of FE for FA production at 1.0  $V_{\text{RHE}}$  (Fig. 10c). Another analogous case was presented by Luo *et al.*, showing that the addition of a p-type semiconductor of  $\text{Bi}_2\text{O}_3$  to n-type  $\text{TiO}_2$  ( $\text{Bi}_2\text{O}_3/\text{TiO}_2$ ) significantly enhanced charge separation, transfer, and light absorption, thereby promoting larger photocurrent density in the PEC glycerol oxidation.<sup>56</sup> The  $\text{Bi}_2\text{O}_3/\text{TiO}_2$  exhibited a higher DHA selectivity than  $\text{TiO}_2$  alone (65.7% vs. 8.2%). In particular, DFT calculation also revealed that  $\text{Bi}_2\text{O}_3$  tends to adsorb the middle hydroxyl of glycerol, selectively generating DHA rather than formic acid (Fig. 10d). Meanwhile, the  $\text{Bi}_2\text{O}_3/\text{TiO}_2$

maintained a high conversion rate ( $>200 \text{ mmol m}^{-2} \text{ h}^{-1}$ ) and FE of DHA for 150 h (Fig. 10e) due to its excellent structural and chemical stability.

n-n heterojunctions have also been employed to promote the reaction rate for PEC organic valorisation. The formation of a type-II heterojunction between defective  $\text{WO}_3$  (m-H-WO<sub>3</sub>) and  $\text{TiO}_2$ , coupled with interfacial and defect engineering, effectively accelerates charge separation and mass transfer.<sup>109</sup> A photocurrent of 2.89  $\text{mA cm}^{-2}$  was achieved at 1.23  $V_{\text{RHE}}$  for the heterojunction photoelectrode, which is more than 1.5 times higher than that of  $\text{WO}_3$ . Likewise, the improved photocurrent stability of m-H-WO<sub>3</sub>/ $\text{TiO}_2$ , 3 times higher than that of m-WO<sub>3</sub>, was demonstrated over 60 min. m-WO<sub>3</sub> exhibited poor photocurrent stability, with a 60% decay occurring within only 35 min. The superior photocurrent stability in m-H-WO<sub>3</sub>/ $\text{TiO}_2$  was attributed to its massive oxygen vacancies, which acted as electron mediators. The production rate of GLYAD and DHA reached 353  $\text{mmol m}^{-2} \text{ h}^{-1}$  at 1.2  $V_{\text{RHE}}$  for the heterojunction photoelectrode, whereas  $\text{WO}_3$  achieved only 133  $\text{mmol m}^{-2} \text{ h}^{-1}$ .

#### 4.3 Co-catalyst modification

Oxidation of organic waste in the absence of a soluble redox mediator generally involves an inner-sphere electron transfer

process. For this process, the reaction kinetics is significantly influenced by the interaction between the electrode material and the reactant/product.<sup>151,152</sup> In this circumstance, the nature of electrode surface is crucial. In other words, to improve the selectivity of the desired products during organic waste conversion, the surface modification of the photoelectrodes with suitable co-catalysts is often necessary. The charge separation and overall activity of a photoelectrode are also possibly enhanced by accelerating charge transfer from the photoelectrode to the co-catalyst.<sup>29,153</sup> For example, Huang *et al.* successfully transformed an inactive  $\text{BiVO}_4$  photoanode into a highly efficient photoanode toward FA production from methanol by nanoFe:Ni-Bi co-catalyst modification (Fig. 11a–c).<sup>154</sup> nanoFe:Ni-Bi was synthesized by pulse-current electrodeposition and was found to be an active catalyst for methanol oxidation, in which the catalytic activity is controlled by the amount of iron species. Cooperating nanoFe:Ni–Bi with  $\text{BiVO}_4$  resulted in remarkable FA production with an FE of  $94.6\% \pm 12.3\%$  through PEC methanol oxidation at  $0.55\text{ V}_{\text{RHE}}$  at neutral pH, while negligible FA formation was observed in pristine  $\text{BiVO}_4$ . In addition,  $\text{BiVO}_4|\text{nanoFe:Ni-Bi}$  exhibited a stable photocurrent density over 2 h. A co-catalyst modification strategy has also been revealed for glycerol valorisation

using tungsten-doped  $\text{BiVO}_4$  (W:BiVO<sub>4</sub>).<sup>55</sup> The co-catalyst of  $\text{NiO}_x(\text{OH})_y$  not only enhanced the production rate but also altered the product distribution. The most valuable product, DHA, was not observed during glycerol valorisation using W:BiVO<sub>4</sub> without the presence of  $\text{NiO}_x(\text{OH})_y$  in a mild alkaline solution (Fig. 11d–f). Upon addition of  $\text{NiO}_x(\text{OH})_y$  co-catalyst, W:BiVO<sub>4</sub> generated DHA with an FE of approximately 20% at  $1.2\text{ V}_{\text{RHE}}$ . However, continuous decay in photocurrent due to the gradual dissolution of the  $\text{NiO}_x(\text{OH})_y$  co-catalyst in alkaline conditions remains a challenge requiring further investigation.

Co-catalyst modification has also been widely adopted for  $\alpha\text{-Fe}_2\text{O}_3$  in the valorisation of organic waste. For instance, CuO acts both as a heterojunction and co-catalyst in  $\text{nanoFe}_2\text{O}_3|\text{CuO}$  for PEC glucose valorisation, as discussed in the heterojunction section (Fig. 10a–c). Taking advantage of the corrosion-resistant properties of  $\alpha\text{-Fe}_2\text{O}_3$  in alkaline solutions, this material is of particular interest in polymer waste valorisation. However, the FE of some target products, such as FA, is often limited. Li *et al.* demonstrated that surface modification of  $\text{Fe}_2\text{O}_3$  photoanode with  $\text{Ni}(\text{OH})_x$  co-catalyst significantly enhanced the FE of FA from PET valorisation, increasing it from 10% to nearly 100% (Fig. 12a–c).<sup>118</sup> In this study,  $\text{Ni}(\text{OH})_x$  co-catalyst was loaded on

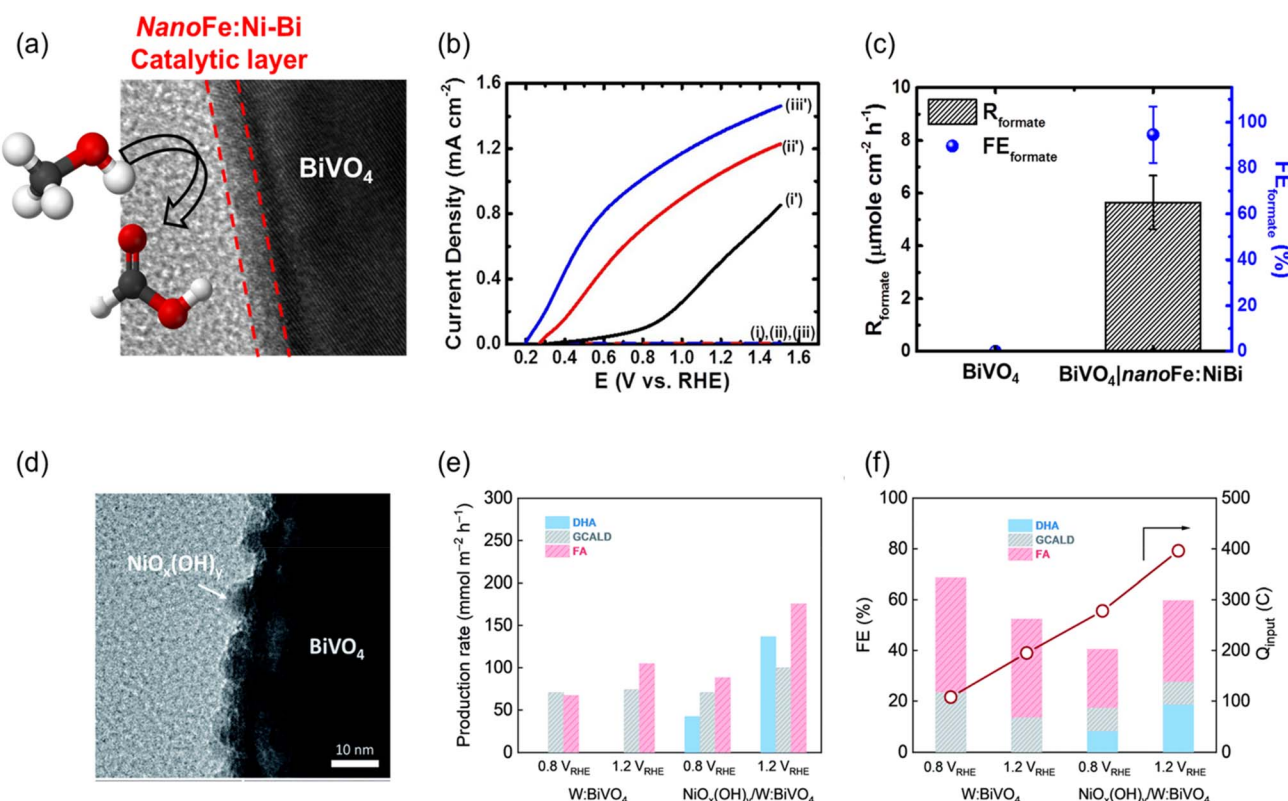


Fig. 11 (a) High-resolution transition electron microscopy (HRTEM) image shows the surface modification of the  $\text{BiVO}_4$  photoanode with nanoFe:Ni-Bi. (b) LSV curves at a scan rate of  $10\text{ mV s}^{-1}$  of (i and i') the pristine  $\text{BiVO}_4$ , (ii and ii')  $\text{BiVO}_4|\text{nanoFe:Ni-Bi}$ , and (iii and iii')  $\text{BiVO}_4|\text{nanoFe:Ni-Bi}$  photoanodes in near-neutral pH containing  $0.1\text{ M}$  methanol in the dark (i'–iii') and under light illumination (i–iii). (c) Production rate of formate ( $R_{\text{formate}}$ ) and  $\text{FE}_{\text{formate}}$  from PEC methanol oxidation using the pristine  $\text{BiVO}_4$  and  $\text{BiVO}_4|\text{nanoFe:Ni-Bi}$  photoanodes. Reproduced with permission.<sup>154</sup> Copyright 2020, Elsevier. (d) HRTEM image illustrating  $\text{NiO}_x(\text{OH})_y$  co-catalyst incorporation on the surface of the W:BiVO<sub>4</sub> electrode. (e) Production rate and (f) FE with total charge passed ( $Q_{\text{input}}$ ) obtained in  $0.5\text{ M}$  KBr. Reproduced with permission under the terms of a CC BY-NC 3.0 license.<sup>55</sup> Copyright 2021, Royal Society of Chemistry.



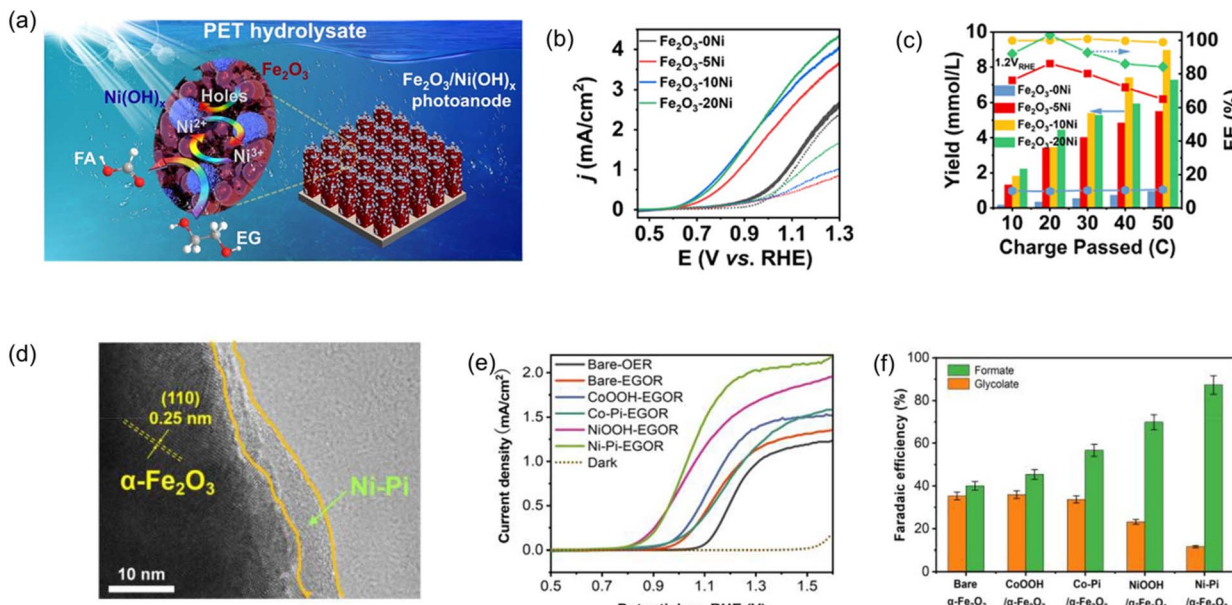


Fig. 12 (a) Schematic of the surface modification of the  $\text{Fe}_2\text{O}_3$  photoanode with  $\text{Ni}(\text{OH})_x$  for selective oxidation of EG into FA. Enhancement of (b) photocurrent and (c) the yield and FE of FA with the charge passed using  $\text{Fe}_2\text{O}_3/\text{Ni}(\text{OH})_x$  photoanodes modified with different concentrations of  $\text{Ni}(\text{OH})_x$ . Reproduced with permission.<sup>118</sup> Copyright 2022, American Chemical Society. (d) TEM image of the Ni-Pi/ $\alpha$ - $\text{Fe}_2\text{O}_3$  photoanode. (e) LSV curves and (f) FE for  $\alpha$ - $\text{Fe}_2\text{O}_3$  with different co-catalysts. FE was derived at 1.1 V for 2 h. Reproduced with permission.<sup>9</sup> Copyright 2023, Elsevier.

the surface of  $\alpha$ - $\text{Fe}_2\text{O}_3$  using a hydrothermal method under a mild temperature.  $\text{Ni}^{2+}$  in  $\text{Ni}(\text{OH})_x$  is proposed to be first oxidized to the higher valence of  $\text{Ni}^{3+}$  by the photo-generated holes from  $\text{Fe}_2\text{O}_3$  and then reduced back to  $\text{Ni}^{2+}$  by oxidising EG, a monomer of PET, to FA. A similar result was observed with a Ni phosphate (Ni-Pi) co-catalyst modified  $\alpha$ - $\text{Fe}_2\text{O}_3$  for EG and PET valorisation.<sup>9</sup> Monomer EG was also obtained by grinding waste PET bottles into micro-sized powder, followed by alkaline hydrolysis in 1 M NaOH at 90 °C for 24 h. Ni phosphate (Ni-Pi) co-catalyst was deposited on  $\alpha$ - $\text{Fe}_2\text{O}_3$  using a simple photo-deposition method (Fig. 12d–f), and the Ni-Pi-modified  $\alpha$ - $\text{Fe}_2\text{O}_3$  (Ni-Pi/ $\alpha$ - $\text{Fe}_2\text{O}_3$ ) photoanode demonstrated an enhancement of FE (87%) toward FA production from EG valorisation compared to unmodified  $\alpha$ - $\text{Fe}_2\text{O}_3$  (40%). The experimental results confirmed that the enhanced PEC performance accounted for the enhancement in charge separation and charge transfer kinetics by Ni-Pi. This study also compared the performance of Ni-Pi-modified  $\alpha$ - $\text{Fe}_2\text{O}_3$  with  $\alpha$ - $\text{Fe}_2\text{O}_3$  modified by other co-catalysts. Ni-Pi demonstrated the highest activity and FE on  $\alpha$ - $\text{Fe}_2\text{O}_3$  compared to CoOOH, NiOOH, and Co-Pi. DFT also revealed that Ni-Pi exhibits a stronger absorption ability toward the EG and promotes efficient desorption of the product of FA compared to NiOOH. Ni-Pi/ $\alpha$ - $\text{Fe}_2\text{O}_3$  photoanode also successfully oxidised waste PET plastic bottle, achieving a high FA FE (82%) and functioned stably for 12 h (6 cycles) due to its structural and chemical stability.

#### 4.4 Nanostructuring

As revealed in eqn (4), the activity in terms of photocurrent in a PEC reaction is determined by three factors,  $\eta_{\text{LHE}}$ ,  $\eta_{\text{sep}}$ , and

$\eta_{\text{int}}$ , for a photoelectrode. Among them,  $\eta_{\text{LHE}}$  and  $\eta_{\text{sep}}$  have contradictory requirements regarding film thickness for a planar photoelectrode. Nanostructuring the photoelectrode can resolve the contradictory issues, thereby enhancing the photocurrent by decoupling the light-harvesting and charge-transport directions. Therefore, it is essential for photoelectrode materials with short charge carrier diffusion lengths, such as  $\alpha$ - $\text{Fe}_2\text{O}_3$ . In addition, the surface area and number of active sites of a photoelectrode can also be enhanced by nanostructuring. Nanostructuring has, therefore, also been demonstrated as a practical approach to boost the reaction rates in PEC organic valorisation.

$\text{V}_2\text{O}_5$  has been demonstrated as an example of the effect of nanostructuring on the performance of methanol oxidation over  $\text{V}_2\text{O}_5$  (Fig. 13a–d).<sup>10</sup> Exfoliation of  $\text{V}_2\text{O}_5$  into nanosheet bundles can be readily achieved by direct top-down exfoliation of sub-micron  $\text{V}_2\text{O}_5$  plates using formamide as the exfoliation agent. The photocurrent for methanol oxidation doubled at 1.3 V<sub>RHE</sub> if the  $\text{V}_2\text{O}_5$  microplate was exfoliated. An impedance study confirms that exfoliating  $\text{V}_2\text{O}_5$  reduces charge transport resistance, owing to a shorter travel distance for photo-generated holes. In addition, the oxygen vacancy ( $\text{V}_\text{O}$ ) increases upon exfoliation, thereby enhancing the conductivity and active sites of  $\text{V}_2\text{O}_5$ .

As mentioned in the previous section, the majority of work in PEC organic valorisation focuses on state-of-the-art photoanodes such as  $\text{TiO}_2$ ,  $\text{WO}_3$ ,  $\text{Fe}_2\text{O}_3$ , and  $\text{BiVO}_4$ . However, except for  $\text{TiO}_2$ , the application of these photoelectrodes is limited to specific reactions due to the narrow operational range in which they can function stably. Most recently, nanosheet-structured  $\text{CuWO}_4$  ( $\text{nanoCuWO}_4$ ) has been investigated across a wide

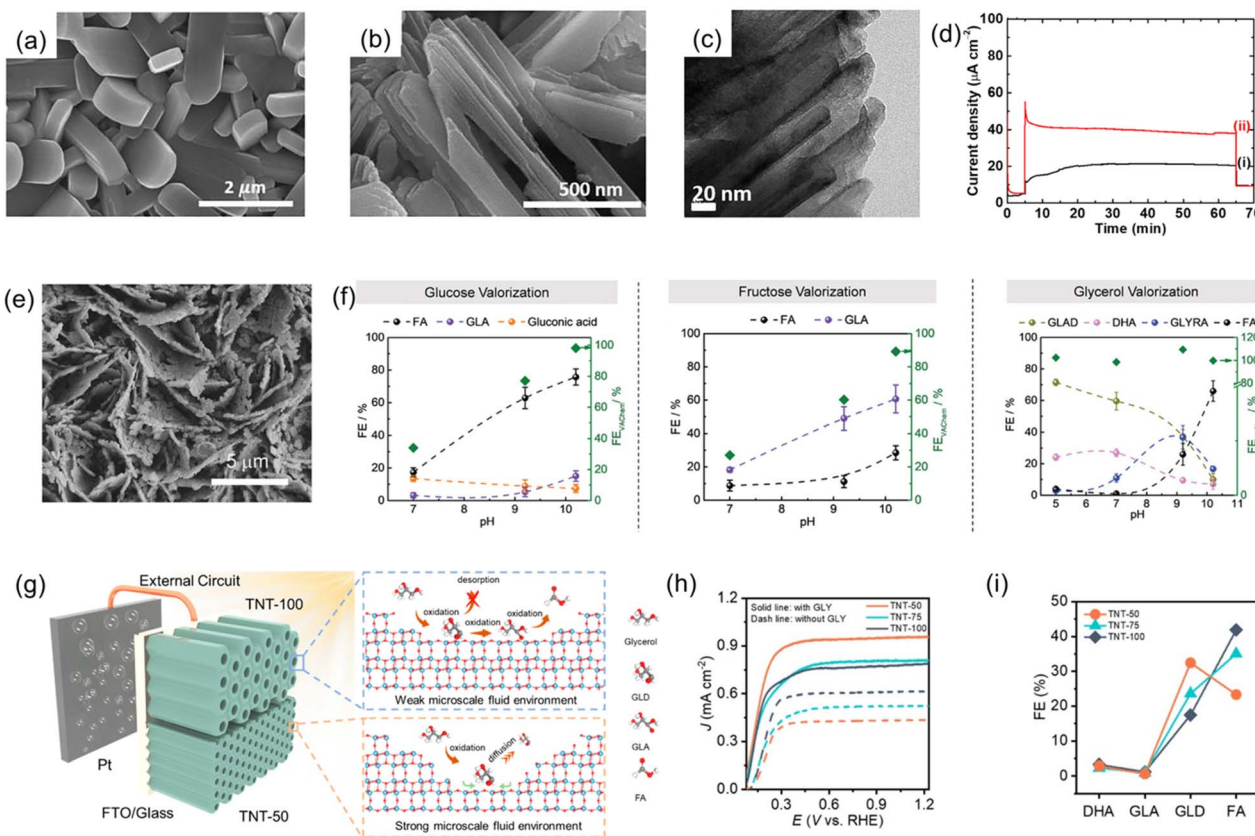


**Fig. 13** SEM images of (a) micro $\text{V}_2\text{O}_5$  and (b) exfoliated  $\text{V}_2\text{O}_5$ . (c) TEM image of the exfoliated  $\text{V}_2\text{O}_5$ . (d) Photocurrent density recorded at 1.3 V<sub>RHE</sub> of (i) micro $\text{V}_2\text{O}_5$  and (ii) exfoliated  $\text{V}_2\text{O}_5$  in 0.1 M  $\text{Na}_2\text{SO}_4$  electrolyte containing 0.1 M methanol. Reproduced with permission under the terms of a CC BY 4.0 license.<sup>10</sup> Copyright 2022, The Author(s), published by Elsevier. (e) SEM image of nanosheet structured  $\text{CuWO}_4$  (f) FE derived from PEC valorisation of glucose (0.8 M), fructose (0.8 M) and glycerol (1.0 M) at 1.23 V<sub>RHE</sub> at the variation of pH. Reproduced with permission.<sup>54</sup> Copyright 2024, John Wiley and Sons. (g) Schematic of the effect of microscale fluid in the PEC glycerol valorisation. (h) LSV curves of the different pore size of  $\text{TiO}_2$  nanotube in  $\text{Na}_2\text{SO}_4$  (0.5 M, pH = 2) with and without the addition of glycerol. (i) FE of the main products formed from glycerol oxidation using  $\text{TiO}_2$  nanotube photoanodes with different pore sizes. Reproduced with permission.<sup>104</sup> Copyright 2024, American Chemical Society.

range of PEC valorisation systems, including glucose, fructose, and glycerol, owing to its broad operational stability (Fig. 13e and f).<sup>54</sup> FE of  $76\% \pm 5\%$  for FA and  $61\% \pm 8\%$  for GLA were achieved at pH 10.2 over  $\text{CuWO}_4$  from PEC glucose and fructose valorisation, respectively. Notably, the FEs of the primary products, GLAD and DHA, were over 85% at neutral and slightly acidic pH using  $\text{CuWO}_4$  for PEC glycerol valorisation. Nano $\text{CuWO}_4$  exhibited a significantly higher photocurrent at 1.23 V<sub>RHE</sub> than a planar  $\text{CuWO}_4$  for PEC water oxidation and glycerol valorisation, demonstrating that nano $\text{CuWO}_4$  provides more active sites in PEC reactions. Notably, the nano $\text{CuWO}_4$  maintained a high total FE of value-added chemicals (100%) over 72 h of photoelectrolysis and retained 60% of its initial photocurrent density after prolonged operation of more than 38 h. This excellent stability was attributed to the preservation of phase properties following long-term operation.

Tuning product selectivity has also been reported to be achieved through nanoconfinement. Lu *et al.* introduced a nanoconfined environment into the glycerol valorisation process using one-dimensional  $\text{TiO}_2$  nanotubes (Fig. 13g–i).<sup>104</sup>

Nanotubes with three pore sizes, 50 nm (TNT-50), 75 nm (TNT-75) and 100 nm (TNT-100), were investigated, among which TNT-50 exhibited the highest photocurrent for PEC glycerol oxidation. The nanoconfined environment accelerated the mass transfer process by the microscale fluid effects. The diffusion rate of glycerol on  $\text{TiO}_2$  nanotubes increased almost fivefold when the tube diameter was reduced from 100 to 50 nm. The faster diffusion rate inhibited the overoxidation of glycerol and enhanced the selectivity of  $\text{C}_3$  products, such as GLAD. The  $\text{TiO}_2$  nanotube also demonstrated promising stability, with no significant photocurrent degradation observed during 10 h of operation.

#### 4.5 Crystal facet and crystal phase engineering

Beyond doping, co-catalyst addition, or heterojunction formation, crystal facet and crystal phase engineering have also been demonstrated to enhance the performance of photoelectrodes for organic valorisation. These crystalline and phase properties influence surface reactivity by promoting favourable adsorption or facilitating the activation of specific reactants. These



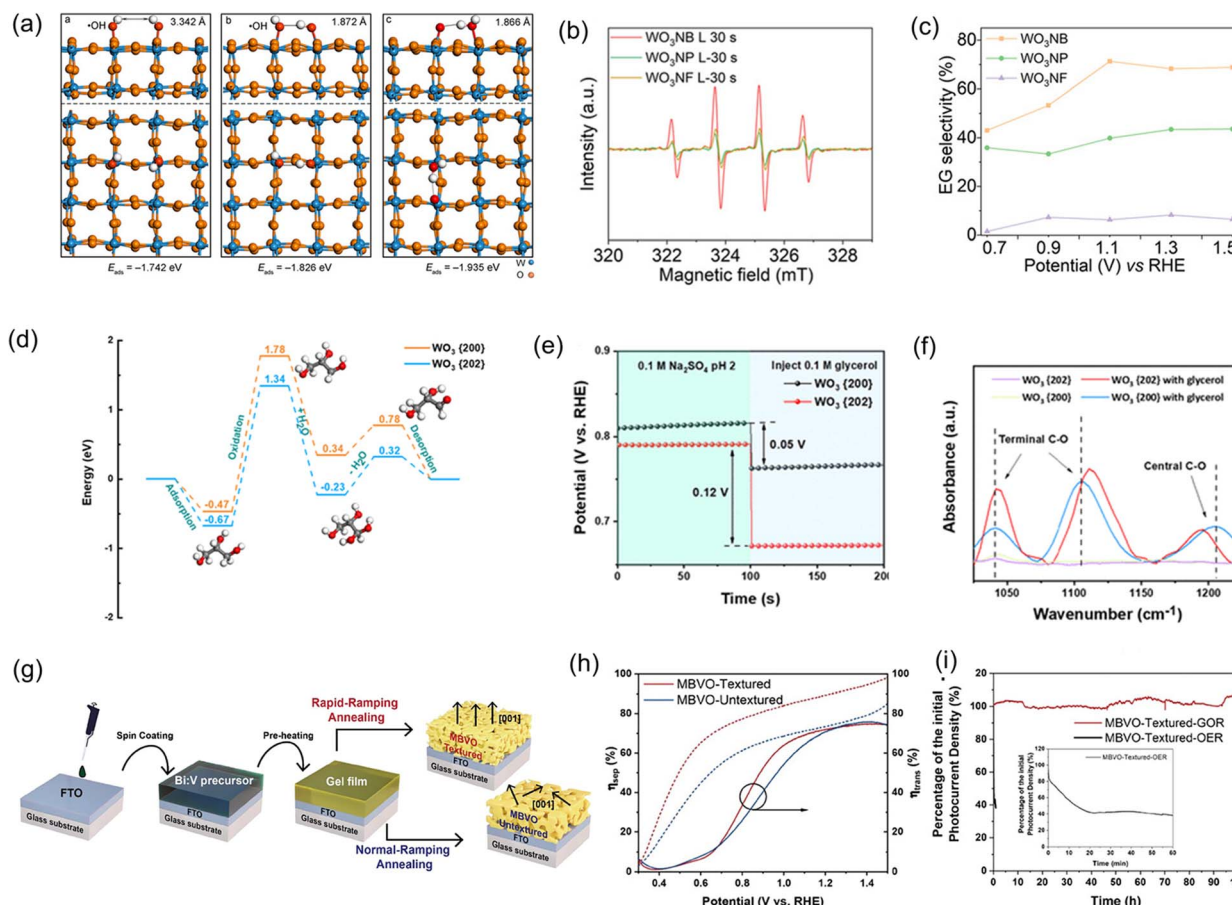


**Fig. 14** (a) Representation of the atomic structures of the lowest-energy ·OH adsorption on twinning W atoms of different facets, in which, from left to right, the sequence is facets of (010), (100), and (001). The corresponding adsorption energy is presented at the bottom. (b) EPR analyses of ·OH in the presence of  $\text{WO}_3$  NB,  $\text{WO}_3$  NP or  $\text{WO}_3$  NF after light illumination (c) PEC  $\text{CH}_4$ -to-EG conversion selectivity at various potential using the photoanode of  $\text{WO}_3$  NB,  $\text{WO}_3$  NP or  $\text{WO}_3$  NF. Reproduced with permission.<sup>108</sup> Copyright 2021, John Wiley and Sons. (d) Energy profiles derived from DFT calculation of glycerol oxidation on  $\text{WO}_3$  at the facets of (200) and (202). (e) The comparison of  $\text{WO}_3$  in OCP change between facets of (200) and (202) in a supporting electrolyte with subsequent injection of 0.1 M glycerol. (f) FT-IR absorbance spectra of the C–O bond vibration peaks of  $\text{WO}_3$  photoanodes with predominant facets of (200) and (202) in a  $\text{Na}_2\text{SO}_4$  solution with or without glycerol. Reproduced with permission.<sup>69</sup> Copyright 2022, American Chemical Society. (g) Schematic representation of the process of synthesising textured and untextured MBVO. (h) The  $\eta_{\text{sep}}$  and  $\eta_{\text{int}}$  ( $\eta_{\text{trans}}$ ) of textured and untextured MBVO. (i) The PEC stability of textured MBVO under glycerol oxidation and OER (inset) conditions. Reproduced with permission.<sup>115</sup> Copyright 2024, John Wiley and Sons.

strategies have been applied on both  $\text{WO}_3$  and  $\text{BiVO}_4$  to improve the activity and selectivity for organic valorisation. Ma *et al.* optimised the reactivity of hydroxyl radicals (·OH) by tuning the crystal facet of  $\text{WO}_3$  to achieve efficient EG production from  $\text{CH}_4$  (Fig. 14a–c).<sup>108</sup> The photo-generated ·OH radicals played a significant role in  $\text{CH}_4$  activation and subsequent EG formation. Their DFT calculations revealed that (010) facet exhibited the highest presence of ·OH on the surface compared to the (100) and (001) facets. This was attributed to the spatial proximity of adsorbed ·OH radicals on the (100) and (001) surfaces, which led to their disappearance *via* the formation of surface-bound O and  $\text{H}_2\text{O}$ . As a result,  $\text{WO}_3$  nanobar ( $\text{WO}_3$  NB), which had the highest proportion of the (010) facet, showed superior EG production rate and selectivity compared to  $\text{WO}_3$  nanoplate ( $\text{WO}_3$ NP) and  $\text{WO}_3$  nanoflake ( $\text{WO}_3$ NF), both of which had lower (010) facet ratios. This trend was corroborated by electron paramagnetic resonance (EPR) measurements, which showed that

$\text{WO}_3$  NB exhibited the strongest signal of DMPO-·OH among the three morphologies. The  $\text{WO}_3$  NB also exhibited stable photocurrent density during 12 h of photoelectrolysis, confirming its promising stability for  $\text{CH}_4$  conversion.

Engineering the  $\text{WO}_3$  facet for optimising the generation of GLAD has also been reported (Fig. 14d–f).<sup>69</sup> The production of GLAD originates from the two-electron oxidation of the primary hydroxyl group of glycerol. A  $\text{WO}_3$  photoanode with predominant (202) facets, denoted as  $\text{WO}_3$  (202), exhibited a higher production rate and selectivity for GLAD than  $\text{WO}_3$  with predominated (200) facets ( $\text{WO}_3$  (200)). This was attributed to the superior light absorption properties and higher carrier concentration of  $\text{WO}_3$  with predominated (202) facet. In addition, the DFT calculations revealed that the crystal facet of (202) showed stronger glycerol adsorption and facilitated its activation more effectively than the (200) facet. The (202) facet also exhibited easier desorption of GLAD. The stronger glycerol

absorption tendency on  $\text{WO}_3$  (202) was evidenced by a more pronounced cathodic shift in open-circuit potential (OCP) after the addition of glycerol. Furthermore, Fourier-transform infrared (FT-IR) spectra indicated that, compared to  $\text{WO}_3$  (200), the C–O bond vibration peaks of the primary and secondary hydroxyl groups shifted to higher and lower wave-numbers, respectively, on  $\text{WO}_3$  (202). Both OCP and FT-IR studies experimentally demonstrated that  $\text{WO}_3$  (202) had a higher tendency for PEC GLAD production from glycerol. Notably,  $\text{WO}_3$  (202) also exhibited excellent photocurrent stability without any decay for 12 h, while the photocurrent density of  $\text{WO}_3$  (200) remained at approximately 70% of its initial photocurrent density at 1.2 V<sub>RHE</sub>.

In addition to the crystal facet effect in  $\text{WO}_3$ , Wu *et al.* investigated the effect of the crystal phase of  $\text{WO}_3$ , including monoclinic (m- $\text{WO}_3$ ) and hexagonal (h- $\text{WO}_3$ ), on HMF oxidation to DFF.<sup>68</sup> m- $\text{WO}_3$  outperformed h- $\text{WO}_3$ , attributed to enhanced light absorption, improved charge separation, optimised reactant adsorption and a higher oxidation capacity of the photo-generated holes. Consequently, m- $\text{WO}_3$  exhibited a lower onset potential at 0.6 V<sub>RHE</sub> and a significant increase in photocurrent density, reaching 1.1 mA cm<sup>-2</sup> at 1.3 V<sub>RHE</sub> (a sixfold enhancement over h- $\text{WO}_3$ ). Under constant irradiation at 1.1 V<sub>RHE</sub>, m- $\text{WO}_3$  retained 50% of its initial photocurrent.

Benefiting from the enhancement of reaction rate or selectivity by tuning the preferential crystal orientation has also been demonstrated in the case of  $\text{BiVO}_4$ . Wu *et al.* synthesized textured Mo-doped  $\text{BiVO}_4$  (MBVO) with a (001) crystal orientation *via* a rapid-ramping annealing method and applied it for glycerol oxidation reaction (GOR) (Fig. 14g–i).<sup>115</sup> The (001) crystal orientation in MBVO-textured provided a substantially enhanced  $\eta_{\text{sep}}$  of 90% at 1.23 V<sub>RHE</sub>, exceeding that of randomly oriented untextured MBVO (74%). Accordingly, the textured MBVO exhibited a photocurrent density of  $7.45 \pm 0.19$  mA cm<sup>-2</sup> at 1.23 V<sub>RHE</sub>, corresponding to 99% of the  $J_{\text{max}}$  of  $\text{BiVO}_4$  (Table 2). Notably, the textured MBVO also showed promising stability of photocurrent density up to 100 h at 0.8 V<sub>RHE</sub> in GOR, originating from its high  $\eta_{\text{sep}}$  from (001) crystal orientation coupled with optimisation of photo-generated hole utilisation in glycerol oxidation. In another study, the difference in activity and selectivity toward DHA production from PEC glycerol valorisation between facets of (010) and (121) has been explored.<sup>114</sup> Their FT-IR results indicated that (010) had a much stronger absorption signal for the C–O bond vibration peak of the secondary hydroxyl group than that of the facet (121). Although the DFT calculation aligned with the FT-IR result, there was only

a subtle difference in the adsorption energy between facets of (010) and (121). This might result from the DFT used being the simplest one, without considering the solvent effect.

The above discussion on strategies related to the effect of achieving different levels of improvement on photoelectrode activity, target product selectivity, and PEC stability are summarised in Table 3.

## 5. PEC reduction for organic synthesis

PEC organic valorisation typically takes the thermodynamic benefits of organic oxidation to replace the sluggish OER. Therefore, most PEC organic valorisation studies focus on the oxidation process. Some studies still focus on organic reduction, although a cathode, rather than a photocathode, is normally employed in a PEC system. The production of BHMF from HMF using a PEC system consisting of an Ag cathode and a  $\text{BiVO}_4$  photoanode serves as a representative example.<sup>28</sup> BHMF is an essential starting agent in the polymerisation and

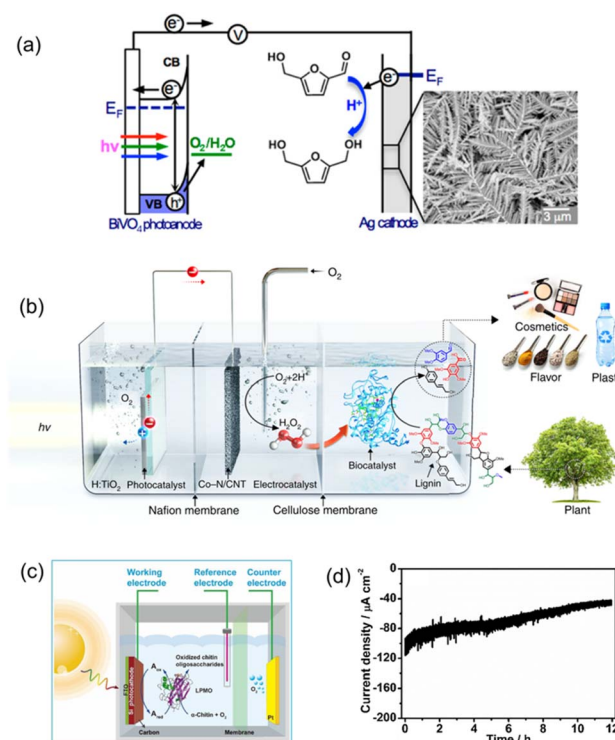


Fig. 15 Schematic of (a) the PEC cell consisting of a  $\text{BiVO}_4$  photoanode and Ag cathode for HMF reduction into BHMF. Reproduced with permission.<sup>28</sup> Copyright 2016, American Chemical Society. (b) Photo-electro-biochemical reactor with a  $\text{TiO}_2$  photoanode harvesting sunlight and a Co–N/CNT cathode to generate  $\text{H}_2\text{O}_2$ , which is provided to the biocatalyst for lignin valorisation. Reproduced with permission under the terms of a CC BY 4.0 license.<sup>155</sup> Copyright 2019, The Author(s), published by Springer Nature. (c) Inorganic-biological hybrid PEC system with a Si/C photocathode for light harvesting and a LPMO catalysing  $\alpha$ -chitin valorisation. (d) Long-term stability of the Si/C photocathode. Reproduced with permission.<sup>156</sup> Copyright 2020, Elsevier.

Table 3 Summary of various strategies for achieving different levels of improvement, where ●●● denotes pronounced enhancement and ○○○ denotes minimal impact

	Activity	Selectivity	Stability
Doping	●●○	●○○	●○○
Heterojunction	●●○	●●○	●○○
Co-catalyst modification	●●○	●●●	●○○
Nanostructuring	●●●	●○○	○○○
Crystal facet and phase engineering	●●○	●●●	●○○



etherification industries. BHMF is produced under conditions of high pressure (>28 bar) and temperature (>403 K) using H<sub>2</sub> as the hydrogen source. On the other hand, the EC reduction of HMF to BHMF can be operated under ambient conditions and utilise water as a hydrogen source, bypassing the need for H<sub>2</sub>. The authors systematically investigated HMF reduction using a dendritic fractal structured Ag cathode synthesised by galvanic displacement, denoted as Ag<sub>gd</sub>. The Ag<sub>gd</sub> exhibited an FE close to 100% toward BHMF. To reduce energy consumption, a PEC cell containing a BiVO<sub>4</sub> photoanode and an Ag cathode was then constructed. Photo-generated holes from BiVO<sub>4</sub> were used for OER, while the photoexcited electron was transferred to the Ag cathode to reduce HMF into BHMF (Fig. 15a). This PEC cell not only exhibited a comparable FE (94%) with an EC cell, but it also reduced the energy consumption required from the applied voltage.

A PEC cell integrated with an enzyme, a biocatalyst, has been recently investigated for the valorisation of lignin and  $\alpha$ -chitin (Fig. 15b). Myohwa Ko *et al.* demonstrated a PEC system consisting of a TiO<sub>2</sub> photoanode for photovoltage generation and a Co-N/carbon nanotube (Co-N/CNT) cathode for oxygen reduction reaction.<sup>155</sup> The cathodic product H<sub>2</sub>O<sub>2</sub> acted as an electron acceptor for lignin peroxidase isozyme H8, which has high activity toward selective  $\beta$ -O-4 bonds in lignin cleavage. To prevent damage to the enzyme from high concentrations of H<sub>2</sub>O<sub>2</sub>, an additional cellulose membrane was used to separate the cathode and enzyme. The enzyme-assisted PEC catalyzed the lignin dimer depolymerisation with 93.7% conversion and 98.7% selectivity for 3,4-dimethoxybenzaldehyde, a vanillin derivative.

Generation of chitin oligosaccharides from  $\alpha$ -chitin over a Si/C integrated with lytic polysaccharide monooxygenases enzyme mediator (LPMO) in the presence of a redox mediator is a rare example of using a photocathode for PEC reduction valorisation (Fig. 15c and d).<sup>156</sup> The mediator, such as 2,6-dimethyl-1,4-benzoquinone (DMBQ), was first photoelectrochemically reduced by the Si/C photocathode. The reduced DMBQ subsequently provided the reductive power to LPMO, assisted by O<sub>2</sub> activation, to convert  $\alpha$ -chitin to oligosaccharide. The PEC system can be realised under benign environmental conditions for the sustainable valorisation of  $\alpha$ -chitin. However, this system exhibited a photocurrent density decay of more than 60% after 12 h. Improving the stability of this system remains a subject for further investigation.

## 6. Integrated PEC cell for cogeneration of solar fuel and value-added chemical

This section discusses the integrated PEC systems for simultaneous solar fuel and value-added chemical production. There are many configurations of PEC systems. However, a tandem PEC cell consisting of a cathode and an anode, in which at least one of the electrodes is a photoelectrode, is focused on, as this type of PEC cell has the most concise design and is easily scalable. In addition, a review of a photovoltaic (PV) integrated with a two-electrode PEC system is also included, as this type of

design is widely applied to PEC cells that require an external bias to achieve a sufficient production rate.

### 6.1 Photoanode paired with a cathode

The pioneering work of an integrated PEC cell for the cogeneration of value-added chemicals and H<sub>2</sub> was demonstrated in 2015.<sup>70</sup> The PEC cell consists of a BiVO<sub>4</sub> photoanode connected to a Pt cathode in a tandem configuration and was used for FDCA and H<sub>2</sub> production. Additionally, TEMPO in the electrolyte is employed as a mediator and catalyst. Under light illumination, photo-generated holes from BiVO<sub>4</sub> oxidise TEMPO to TEMPO<sup>+</sup>, further catalyses HMF conversion into FDCA. Meanwhile, the photoexcited electrons were transferred to the Pt cathode for H<sub>2</sub> evolution. The authors also compared the TEMPO oxidation activity at the BiVO<sub>4</sub> photoanode under light illumination with that at an Au electrode. Compared to the Au electrode, the bare BiVO<sub>4</sub> photoanode exhibited a reduction of 0.7 V in the potential necessary for HMF oxidation due to its sufficient  $E_{VB}$  to drive the TEMPO oxidation under light illumination. TEMPO-mediated PEC HMF oxidation resulted in 93% FE of FDCA. A PEC cell consisting of a photoanode and a cathode was also employed for PET valorisation and H<sub>2</sub> co-generation. Lin *et al.* demonstrated an integrated PEC cell consisting of nickel phosphide nanoparticle-modified TiO<sub>2</sub> nanorods photoanode (nanoTiO<sub>2</sub>/nanoNiP) and carbon nanotubes/nickel phosphide nanoparticles nanocomposite (CNT/nanoNiP) cathode for the valorisation of PET lysate (EG) into FA and H<sub>2</sub> (Fig. 16a and b), respectively.<sup>106</sup> PET bottles were pre-treated by cutting into flakes, followed by alkaline hydrolysis in 2 M KOH at 80 °C for 24 h to get EG. CV activation was beneficial in the surface reconstruction of nano-NiP into  $\beta$ -NiOOH active site of EG oxidation. Furthermore, P in nanoNiP was critical in suppressing further transformation of  $\beta$ -NiOOH into  $\gamma$ -NiOOH. Meanwhile, the pristine nanoNiP was found to be active as an HER catalyst. In the 4-h photoelectrolysis, the PEC cell containing nanoTiO<sub>2</sub>/nanoNiP photoanode and CNT/nanoNiP cathode exhibited an FE of 57.1%  $\pm$  1.7% toward FA and an FE of 76.8%  $\pm$  7.8% toward H<sub>2</sub> at an external bias of 0.5 V.

As revealed in the last example, a PEC system might still need an external bias supply, although the required external bias is generally much less than in an EC system. A PV cell is typically further connected and stacked with a PEC cell to form an integrated, standalone PV-PEC system. For instance, a PV-PEC system has been applied to water splitting and glycerol valorisation over a CuWO<sub>4</sub> photoanode (Fig. 16c–e).<sup>54</sup> The PV-PEC cell exhibited a significantly higher operating photocurrent for glycerol valorisation than for water splitting. Product analyses also confirmed that the production rate of H<sub>2</sub> in glycerol valorisation was approximately double that of water splitting. This corresponding finding supports that PEC valorisation can generate more valuable chemicals than water splitting and accelerate the H<sub>2</sub> production rate.

### 6.2 Photocathode paired with an anode

The majority of cathodic reactions, including HER, CO<sub>2</sub>RR, and NH<sub>3</sub> production, have been demonstrated to couple with



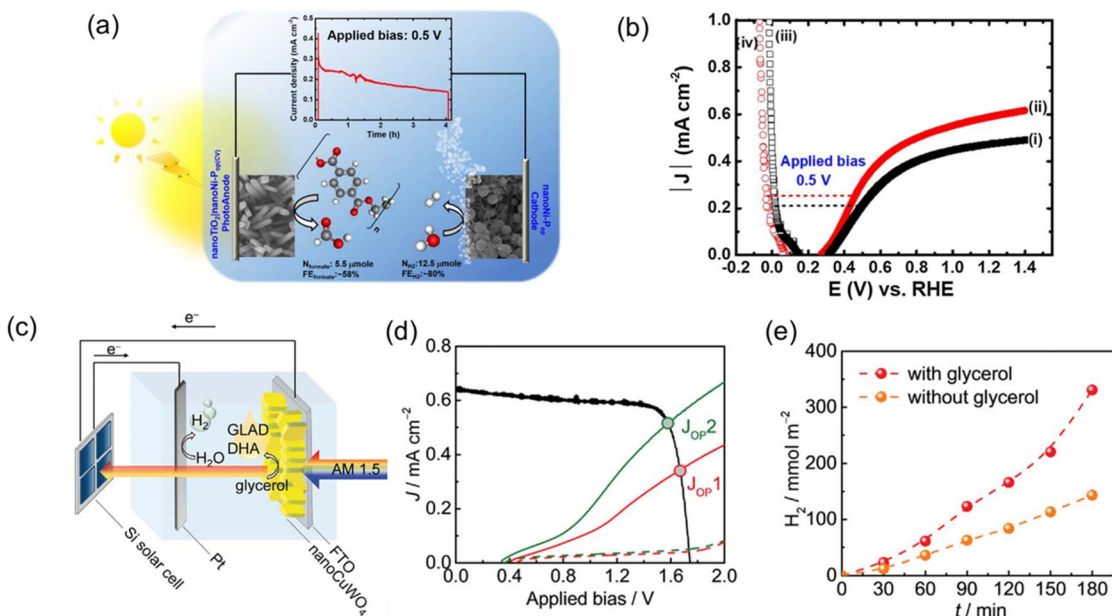


Fig. 16 (a) Schematic of an integrated PEC cell comprising a nanoTiO<sub>2</sub>/nanoNiP photoanode paired with a CNT/nanoNiP cathode, and the chronoamperometric curve under light illumination of the PEC cell. (b) LSVs of (i) bare nanoTiO<sub>2</sub>, (ii) nanoTiO<sub>2</sub>|nanoNi-P<sub>op</sub>(CV), (iii) Pt foil, and (iv) CNT/nanoNi-P<sub>op</sub>. A solid line was recorded under light illumination in the deaerated PET lysate, whereas a dashed line was obtained in the dark in the deaerated KOH solution. Reproduced with permission under the terms of a CC BY 4.0 license.<sup>106</sup> Copyright 2021, The Author(s), published by Elsevier. (c) Schematic representation of a photovoltaic device (Si solar cell) connected to the nanoCuWO<sub>4</sub>-based PEC cell for simultaneous glycerol valorisation and H<sub>2</sub> production. (d) Overlaid J-V curves of the Si solar cell and nanoCuWO<sub>4</sub>-based PEC cell either for glycerol oxidation (green) or water oxidation (red). Solid and dash lines represent the J-V curves measured in the light and dark, respectively. (e) Amount of H<sub>2</sub> generated by the nanoCuWO<sub>4</sub>-based PV-PEC cell from glycerol valorisation and water splitting. Reproduced with permission.<sup>54</sup> Copyright 2024, John Wiley and Sons.

organic oxidation in the configuration of a photocathode paired with an anode. Bhattacharjee *et al.* demonstrated a PEC cell to valorise organic waste into valuable chemicals and co-generate H<sub>2</sub>.<sup>157</sup> The PEC cell consisted of a Pt-decorated lead-halide perovskite (perovskite|Pt) photocathode for PEC HER and Cu<sub>30</sub>Pd<sub>70</sub> alloy micro-flowers for oxidation of organic waste such as PET and cellulose (Fig. 17a–e). The PET bottle was first cut and ground into a smaller pieces, followed by alkaline hydrolysis in 1 M KOH at 80 °C for 120 h to obtain monomer EG. Under 10 h bias-free photoelectrolysis, Cu<sub>30</sub>Pd<sub>70</sub>||perovskite|Pt PEC cell, both in two-compartment and “artificial leaf” configurations, exhibited photocurrent density of 4–9 mA cm<sup>-2</sup> from valorisation of plastic, biomass, and glycerol. Product selectivity from the oxidation of organic wastes ranged from 60% to 90%, while H<sub>2</sub> was co-generated with FEs of exceeding 90% during the valorisation of different organic waste.

CO<sub>2</sub>RR, coupled with organic waste valorisation, was further demonstrated by the same group using a similar perovskite photocathode-based PEC system. A zero-bias PEC cell consisting of a CO<sub>2</sub> reduction catalyst (CO<sub>2</sub>R<sub>cat</sub>)-modified lead-halide perovskite (PVK) photocathode and a Ni foam|Cu<sub>27</sub>Pd<sub>73</sub> micro-flower anode was used for PEC CO<sub>2</sub>RR and plastic valorisation.<sup>158</sup> Three different CO<sub>2</sub>R<sub>cat</sub>, including cobalt porphyrin (CoP<sub>L</sub>), Cu<sub>91</sub>In<sub>9</sub> alloy, and tungsten-formate dehydrogenase (FDH) biocatalyst, were incorporated onto the perovskite surface, and their CO<sub>2</sub>RR performance was investigated. PEC reduction products at the photocathode part were CO (FE of

90%), syngas (CO/H<sub>2</sub> = 1/1, FE of 43% (CO) and 49% (H<sub>2</sub>)), and FA (95%) using PVK|COP<sub>L</sub>, PVK|Cu<sub>91</sub>In<sub>9</sub>, and PVK|FDH photocathodes, respectively. On the other hand, the Cu<sub>27</sub>Pd<sub>73</sub>-based anode exhibited high selectivity with an FE exceeding 90% toward GLA from PET plastics. In addition, the PEC cells consisting of Ni foam|Cu<sub>27</sub>Pd<sub>73</sub> anode and either a PVK|Cu<sub>91</sub>In<sub>9</sub> or PVK|FDH photocathode also demonstrated stable photocurrent densities for up to 10 h. Meanwhile, a slight decay in the photocurrent density was observed when PVK|COP<sub>L</sub> was employed as the photocathode. This system is significant for developing high-value chemicals from the CO<sub>2</sub>RR platform, as conventional PEC CO<sub>2</sub>RR is limited by the high thermodynamic barrier associated with the OER.

PEC nitrate reduction (NO<sub>3</sub>RR) to form ammonia (NH<sub>3</sub>) has recently attracted considerable attention, as it generates green NH<sub>3</sub> from nitrate-contaminated solutions. Furthermore, NH<sub>3</sub> is a promising H<sub>2</sub> carrier due to its safer and more efficient transportation. Tayyebi *et al.* recently demonstrated a bias-free PEC cell for co-generating NH<sub>3</sub> and glyceric acid from NO<sub>3</sub><sup>-</sup> and glycerol, respectively.<sup>159</sup> The PEC cell was composed of a Ru-loaded titanate nanosheet loaded on a Ni-modified Pb-perovskite (Ru@TiNS/Ni/perovskite) photocathode and a Pt-decorated TiNS electrocatalyst, and could be operated bias-free. The bias-free PEC full cell achieved a stable photocurrent density of 21.2 ± 0.7 mA cm<sup>-2</sup> over 24 h, which was attributed to the effective Ni coating that acted as a protecting layer over the perovskite photoelectrode, along with strong bonding between



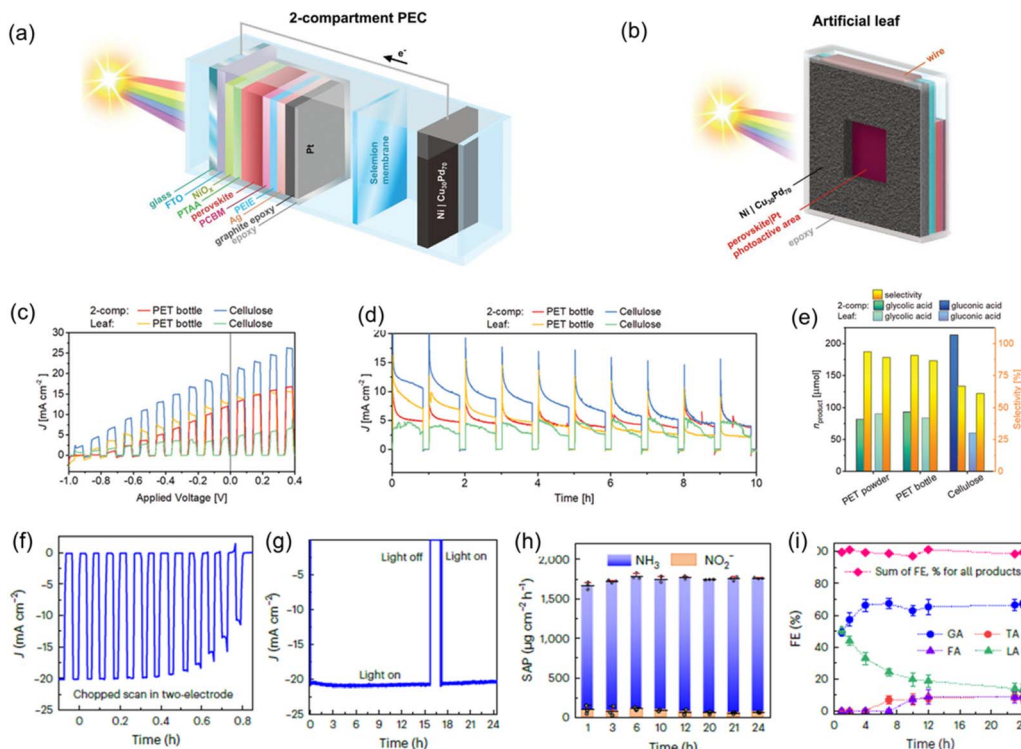


**Fig. 17** Illustration of the  $\text{Cu}_{30}\text{Pd}_{60}$ |perovskite|Pt PEC system in (a) the two-compartment and (b) artificial leaf. PEC analyses using the two-compartment system or the artificial leaf in a solution containing pre-treated polymeric and real-world substrates in (c) chopped scans and (d) bias-free chronoamperometry. (e) Amount of oxidation product along with the corresponding selectivity generated from different substrates after 10 h of bias-free PEC reactions using the two-compartment system or the artificial leaf. Reproduced with permission under the terms of a CC BY 4.0 license.<sup>157</sup> Copyright 2021, The Author(s), published by John Wiley and Sons. (f) Chopped scan and (g) bias-free chronoamperometry of the Ru@TiNS/Ni|perovskite photocathode in a two-electrode integrated system. (h) SAP, the amount of reduction product produced from under AM 1.5 G simulated one-sun condition per hour over an area of  $1\text{ cm}^2$ , of  $\text{NH}_3$  and  $\text{NO}_2^-$ , and (i) FE of the oxidation products from glycerol using the two-electrode system under bias-free condition. Ru@TiNS/Ni|perovskite and Pt@TiNS electrocatalysts were used as the photocathode and the anode in the two-electrode system, respectively. Reproduced with permission.<sup>159</sup> Copyright 2024, Springer Nature.

the Pt and TiNS at the anode (Fig. 17f and g). The reduction product was  $\text{NH}_3$ , with a high yield of  $1744.9\text{ }\mu\text{g NH}_3\text{ cm}^{-2}\text{ h}^{-1}$ , corresponding to an FE of  $99.5\% \pm 0.8\%$ . Meanwhile, the major oxidation products were glyceric acid and lactic acid, which has a combined FE of  $98.1\% \pm 2.4\%$  (Fig. 17h and i).

### 6.3 Photocathode paired with a photoanode

There is relatively limited research on using two photoelectrodes in a PEC cell. Recently, PEC  $\text{CO}_2\text{RR}$  coupled with PEC biomass oxidation for concurrent FA production has been demonstrated by Pan *et al.* A dual-photoelectrode PEC cell consisting of Bi/GaN/Si and NiOOH/ $\alpha$ - $\text{Fe}_2\text{O}_3$  wafers was used for  $\text{CO}_2\text{RR}$  and biomass valorisation, respectively (Fig. 18a–c).<sup>18</sup> For the single photoelectrode performance in a three-electrode system, the NiOOH/ $\alpha$ - $\text{Fe}_2\text{O}_3$  photoanode outperformed other  $\alpha$ - $\text{Fe}_2\text{O}_3$ -based photoanodes, including  $\alpha$ - $\text{Fe}_2\text{O}_3$ , CoOOH/ $\alpha$ - $\text{Fe}_2\text{O}_3$ , and FeOOH/ $\alpha$ - $\text{Fe}_2\text{O}_3$ , with the  $\text{FE}_{\text{FA}}$  of approximate 97% and stable performance for 10 h. This was due to NiOOH enhancing the hole separation and charge transfer kinetics of  $\alpha$ - $\text{Fe}_2\text{O}_3$ , as evident from its lowest charge transfer resistance and the smallest calculated Gibbs free energy barrier for converting glucose into FA. The NiOOH/ $\alpha$ - $\text{Fe}_2\text{O}_3$  photoanode was also able to oxidise real-world biomass to FA with an FE of over 90% and

remain stable for 100 h. Shifting the focus to the cathodic side, the Bi/GaN/Si photocathode exhibited an FE of 85.2% toward FA at  $-0.2\text{ V}$  and stable for 10 h. The Bi/GaN/Si and NiOOH/ $\alpha$ - $\text{Fe}_2\text{O}_3$  were subsequently integrated into a two-electrode tandem configuration. The top electrode of NiOOH/ $\alpha$ - $\text{Fe}_2\text{O}_3$  first absorbed the simulated solar light, and the attenuated light was absorbed by the bottom electrode of Bi/GaN/Si. The energy consumption from external voltage was significantly reduced by over 300 mV in the biomass oxidation- $\text{CO}_2\text{RR}$  system compared to the conventional OER- $\text{CO}_2\text{RR}$  system. By integrating commercial crystalline Si solar cells with the tandem PEC cell, the system produced FA at  $1044\text{ }\mu\text{mol cm}^{-2}$  and  $817\text{ }\mu\text{mol cm}^{-2}$  at the photoanode and photocathode, respectively, and worked stably for 80 h.

A  $\text{Cu}_2\text{O}$  photocathode paired with a  $\text{BiVO}_4$  photoanode in a two-electrode tandem configuration ( $\text{Cu}_2\text{O}/\text{BiVO}_4$ ) has been demonstrated as a state-of-the-art PEC system for solar water splitting.<sup>160</sup> The two-electrode  $\text{Cu}_2\text{O}/\text{BiVO}_4$  tandem cell, with the assistance of a co-catalyst, generated a photocurrent of  $1\text{ mA cm}^{-2}$  under one-sun illumination. However, the  $\text{Cu}_2\text{O}/\text{BiVO}_4$  tandem cell exhibited significant instability for water splitting, losing the majority of its photocurrent within 1 min. Most recently, Kang *et al.* synthesized and demonstrated  $\text{BiVO}_4/\text{NiCo}$



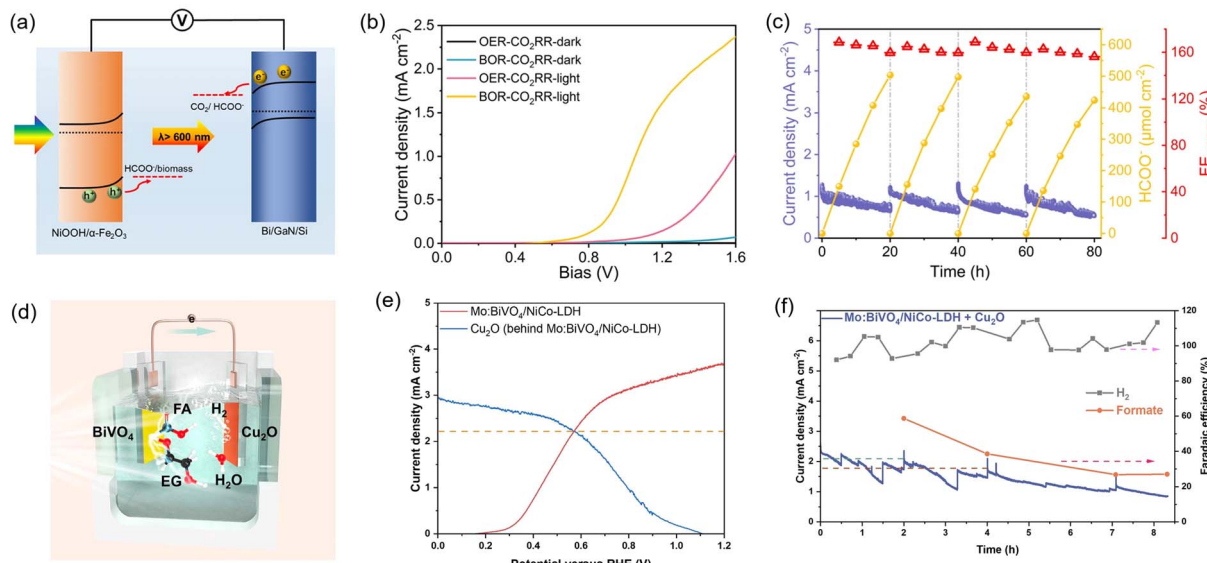


**Fig. 18** (a) Schematic representation of the two-photoelectrode tandem PEC cell consisting of NiOOH/α-Fe<sub>2</sub>O<sub>3</sub> paired with Bi/GaN/Si for FA production from biomass and CO<sub>2</sub>. (b) LSV curves of the tandem PEC cell with (BOR) and without (OER) the addition of biomass. (c) Chronoamperometric curve and corresponding productivity and FEs of FA from biomass and CO<sub>2</sub> using the tandem PEC cell integrated with a Si solar cell under AM 1.5 G one-sun illumination. Reproduced with permission under the terms of a CC BY 4.0 license.<sup>18</sup> Copyright 2023, The Author(s), published by Springer Nature. (d) Schematic of the two-photoelectrode tandem PEC cell for EGOR coupled with HER. PEC cell consists of a BiVO<sub>4</sub>-based photoanode (Mo:BiVO<sub>4</sub>/NiCo-LDH) and a Cu<sub>2</sub>O-based photocathode (Au/Cu<sub>2</sub>O/Ga<sub>2</sub>O<sub>3</sub>/TiO<sub>2</sub>/RuO<sub>x</sub>) and can be operated without bias. (e) LSV curves and (f) unbiased stability investigation along with the corresponding FE of FA and H<sub>2</sub> of the BiVO<sub>4</sub>-based photoanode and the Cu<sub>2</sub>O-based photocathode placed behind the BiVO<sub>4</sub>-based photoanode under simulated AM 1.5 G illumination in buffer solution containing EG at pH 9.0. Reproduced with permission.<sup>111</sup> Copyright 2024, John Wiley and Sons.

LDH photoanodes for EG oxidation reaction (EGOR), subsequently coupled with Cu<sub>2</sub>O photocathode for H<sub>2</sub> production (Fig. 18d-f).<sup>111</sup> In the photoanode, NiCo-LDH significantly improved the photostability of BiVO<sub>4</sub> by accepting the photo-generated holes from BiVO<sub>4</sub> and thereby facilitating the formation of Ni<sup>3+</sup>/Co<sup>3+</sup> active sites for EGOR. Furthermore, they also found that Ni(OH)<sub>x</sub> in NiCo-LDH controlled the selectivity toward EG oxidation into FA, whereas Co(OH)<sub>x</sub> enhanced the photostability by creating a protective layer and passivating surface defects to promote hole transfer to the electrolyte. The synergistic effect between BiVO<sub>4</sub> and NiCo-LDH resulted in a high photocurrent density of 2.3 mA cm<sup>-2</sup> at 1.23 V<sub>RHE</sub>, stable operation up to 200 min, and FE<sub>FA</sub> above 85% in 0.1 M KOH, which outperformed BiVO<sub>4</sub>, BiVO<sub>4</sub>/Ni(OH)<sub>x</sub>, and BiVO<sub>4</sub>/Co(OH)<sub>x</sub>. Additionally, an unassisted PEC device for EGOR and HER by coupling the Mo:BiVO<sub>4</sub>/NiCo-LDH photoanode with a Cu<sub>2</sub>O photocathode resulted in a maximum photocurrent density of 2.3 mA cm<sup>-2</sup> and stable operation up to 2 h with FE<sub>FA</sub> of ~60% and FE<sub>H<sub>2</sub></sub> of ~100%. However, degradation began at 4 h, with photocurrent density decreasing to 1.7 mA cm<sup>-2</sup> (74% of the initial photocurrent density), reducing FE<sub>FA</sub> by ~40%, and finally stabilising at ~30% after 8.3 h. This decline might be attributed to unfavourable product generation from the peroxidation of EG into CO<sub>2</sub>.

## 7. Conclusions and perspectives

PEC organic waste valorisation is an advantageous technique that simultaneously produces value-added chemicals and solar fuels,

thereby supporting the goals of a circular economy and sustainable energy systems. This work provides a comprehensive review of the PEC working principle, the properties of state-of-the-art earth-abundant photoelectrodes, the organic waste pre-treatment process, and strategies for enhancing PEC performance. By taking advantage of its intrinsic photovoltage and fixed hole-oxidising ability (determined by the *E<sub>VB</sub>* of a photoanode) or electron reduction ability (determined by the *E<sub>CB</sub>* of a photocathode), a PEC system potentially offers greater energy savings with improved selectivity control compared to an EC system. Significant progress has been made in tuning the photocurrent and selectivity of photoelectrodes through strategies such as doping, heterojunction formation, co-catalyst modification, nanostructuring, and crystal facet engineering. Each strategy offers specific advantages for improving PEC performance. However, significant challenges remain before PEC organic waste valorisation can become commercially viable. These challenges include, but are not limited to, the need for cost-effective pre-treatment processes, integrated and rational photoelectrode design, the development of selective and compatible co-catalysts, the exploration of novel, earth-abundant photoelectrodes, the investigation of PEC organic reduction pathways, and the development and design of large-scale flow systems. These aspects are discussed in detail in the subsequent text.

### 7.1 Cost-effective pre-treatment process

An alkaline pre-treatment process is commonly reported for PEC valorisation of polymeric waste such as cellulose and



plastics. However, alkaline pre-treatment processes are unlikely to be suitable for system scale-up due to their adverse impact on both cost and the environment. Previous analyses indicate that the pre-treatment process dominates the economic viability of a solar-driven organic waste valorisation plant on a pilot scale.<sup>132</sup> The alkaline pre-treatment process also limits the selection of photoelectrodes to mostly  $\text{TiO}_2$  and  $\text{Fe}_2\text{O}_3$  for polymeric waste valorisation (Table 2). Biological pre-treatment using enzymes is an alternative strategy to depolymerise polymeric waste under benign conditions. However, the accessibility and scalability of some enzymes remain a challenge. Developing catalysts made of earth-abundant elements that can depolymerise polymeric waste in neutral or near-neutral conditions is a possible strategy for alleviating current limitations in the selection of photoelectrodes for PEC polymeric waste valorisation.

## 7.2 Integrated rational design of photoelectrodes

Optimising the photocurrent and stability of photoelectrodes is necessary to realise high-performance PEC organic waste conversion. The indicator of  $\varphi_{\text{PE}}$  is suggested to evaluate the intrinsic performance of a photoelectrode, as it only considers the factors of light harvesting and the charge separation ability of a photoelectrode. However, as shown in Table 2, many studies still have a  $\varphi_{\text{PE}}$  much below 1, especially for  $\text{Fe}_2\text{O}_3$ ,  $\text{Bi}_2\text{WO}_6$ ,  $\text{TaON}$ ,  $\text{CuWO}_4$ , etc. Integrating multiple strategies, such as doping, heterojunction formation, nanostructuring, and crystal facet modulation, might further enhance the  $\varphi_{\text{PE}}$  of these photoelectrodes.  $\text{Mo:BiVO}_4(001)$  serves as an inspiring example of integrating multiple strategies of doping, nanostructuring, and crystal facet modulation, which achieves a  $\varphi_{\text{PE}}$  of close to 1.<sup>115</sup> Persistent fundamental investigation of the material properties and electronic structure is also particularly essential for those photoelectrode with low  $\varphi_{\text{PE}}$ . For example, the kinetic study using *operando* spectroelectrochemical PIA coupled with TPC provides a comprehensive understanding of why  $\alpha\text{-Fe}_2\text{O}_3$  exhibits selective aldehyde production from PEC alcohol oxidation. However, such relative studies remain limited in PEC organic valorisation using other photoelectrodes and substrates. In addition to thermodynamic research, kinetic studies are also undeniably necessary for the development of efficient and selective photoelectrodes for organic waste valorisation.

On the other hand, stability is a crucial parameter for assessing the performance and practicality of a PEC system. Nonetheless, stability continues to be neglected in PEC organic waste valorisation, although 100 h operation has been demonstrated in the studies of  $\text{Mo:BiVO}_4(001)$  for PEC glycerol valorisation<sup>115</sup> and  $\text{NiOOH}/\alpha\text{-Fe}_2\text{O}_3$  for sawdust-derived sugar solution.<sup>18</sup> Strategies such as doping and heterojunction formation, widely applied in the current PEC valorisation studies, offer only modest enhancements to stability (Table 3). Other strategies to improve the stability of PEC systems, such as surface modification with a stable passivation layer, are suggested to be emphasised in future research. However, several requirements must be met to design a stable and efficient passivation layer for a photoelectrode. For example, the

passivation layer should be thin enough to avoid charge transfer inhibition and parasitic light absorption,<sup>161</sup> and the passivation process must be compatible with the photoelectrode.

## 7.3 Selective and compatible co-catalyst development

Most PEC organic waste valorisation involves an inner-sphere electron transfer process, and the interaction between the electrode interface and the reactant/product determines the reaction kinetics and selectivity. As reviewed in this work, co-catalyst modification is a widely used approach to enhance the selectivity of the target product. However, for PEC polymeric waste valorisation, the co-catalyst was mainly limited to enhancing the FE of the  $\text{C}_1$  product, *i.e.*, FA. As an illustration, Ni-Pi in  $\text{Ni-Pi}/\alpha\text{-Fe}_2\text{O}_3$  enhances the FE of FA to 87% for PEC valorisation of PET hydrolysate,<sup>9</sup> and  $\text{NiOOH}$  in  $\text{NiOOH}/\alpha\text{-Fe}_2\text{O}_3$  enhances the FE of FA to 90% for PEC valorisation of sawdust-derived sugar.<sup>18</sup> On the other hand, the co-catalysts for enhancing the FE of  $\text{C}_{2+}$  are significantly lacking, which restricts the development of PEC organic valorisation from an economic value perspective. It is known that many  $\text{C}_{2+}$  products have a higher economic value than FA. For example, GLA has a market value five times higher than that of FA.<sup>9</sup> Although research on the production of  $\text{C}_{2+}$  compounds from EC organic waste valorisation is abundant,<sup>162,163</sup> most of the electrocatalyst synthetic processes are not readily deposited on or compatible with photoelectrode deposition. Research into electrocatalysts for  $\text{C}_{2+}$  products from organic waste, which can be readily applied to a photoelectrode, would help alleviate the constraints imposed by the limited selection of target products in PEC polymeric waste valorisation.

## 7.4 Novel earth-abundant photoelectrodes exploration

The reported research on PEC organic waste valorisation is mainly limited to using state-of-the-art photoanodes ( $\text{TiO}_2$ ,  $\text{WO}_3$ ,  $\text{BiVO}_4$ , and  $\text{Fe}_2\text{O}_3$ ). These photoanodes have an  $E_{\text{VB}}$  at  $>2.5$  eV, providing sufficient driving force even for water oxidation. However, the strong oxidative power of the photo-generated holes from these photoanodes may result in parasitic OER and  $\text{CO}_2$  formation during the PEC oxidation of organics. A wide bandgap also limits the utilisation of higher wavelength photons in the solar spectrum. Since organic oxidation requires much less oxidative force than water oxidation, a narrower bandgap helps maximise the utilisation of solar light. Exploring other novel earth-abundant semiconductors with narrower bandgaps would significantly impact the progress of PEC organic waste valorisation. Recently, lead halide-based perovskites have attracted immense attention in this area due to their narrow and tunable bandgaps and high light absorption coefficients. Nonetheless, research into robust and lead-free perovskite remains a fundamental challenge in using perovskite-based photoelectrodes for PEC reactions. On the other hand,  $\text{CuWO}_4$  has recently been demonstrated to utilise wavelengths up to 550 nm to perform selective and stable PEC biomass valorisation.<sup>54</sup> However, exploring and investigating other earth-abundant and robust photoelectrodes that can utilise broader visible light or near-infrared light to perform organic valorisation still requires considerable future effort.



## 7.5 PEC organic reduction investigation

Fabricating an integrated PEC cell that generates value-added chemicals or fuels at both half-cells is crucial for fully leveraging incident solar energy. Several breakthroughs have been achieved by pairing organic oxidation with a reduction reaction of HER, CO<sub>2</sub>RR, or NO<sub>3</sub>RR,<sup>111,157–159</sup> in which HER is the most prevalent paired reduction reaction. Unfortunately, many state-of-the-art photocathodes, such as Cu<sub>2</sub>O, undergo severe photocorrosion during HER. Albeit passivating a protective layer partially alleviates the instability issue, the passivation layer often requires arduous or non-scalable procedures, such as atomic layer deposition. An alternative is to replace HER with another reduction reaction with a more positive redox potential than ( $E_{(H^+/H_2)}$ ) and  $E_{red}$  of the photocathode. In particular, given the greater energy savings, some electroreduction reactions of organics, such as the hydrogenation of biomass derivatives, are more suitable for pairing with organic oxidation reactions.<sup>164,165</sup> Although paired organic reduction and oxidation have been recently highlighted in EC systems,<sup>166–168</sup> the relative research on a PEC system is still absent. Research into PEC organic reduction may offer a sought-after solution for photocathodes that easily undergo photocorrosion during HER, with the potential for greater energy savings.

## 7.6 Large-scale flow system development and design

Large-scale development is critical for PEC devices to harvest solar light over a wide area due to the decentralised property of solar light.<sup>169</sup> Therefore, investigating large-scale PEC or PC cells has drawn increasing attention to water splitting.<sup>170–172</sup> An illuminated area of a minimum of 50 cm<sup>2</sup> is typically considered the first phase of large-scale applications.<sup>173,174</sup> However, most of the PEC organic waste valorisation research is still limited to laboratory-scale investigations using small areas of photoelectrodes. Limitations at the laboratory scale are generally attributed to arduous synthetic procedures, manufacturing equipment, and the electronic resistance of electrode substrates. Integrating module units of smaller dimensions to achieve large-scale production is an alternative approach. However, regardless of the design, the need for photoelectrode scale-up must be considered in material selection, engineering, and manufacturing.

In contrast to water splitting, which has an endless supply of substrate, *i.e.*, water, the amount of substrate is limited by the solubility of organic waste in water for organic valorisation reaction. The effects of reactant consumption and mass transfer on product selectivity in organics valorisation must be carefully considered. Current research mainly performs the PEC valorisation reaction in a batch system. However, continuous reactant consumption and product accumulation in a batch system result in the unfavourable overoxidation of the target products. Examples can be easily found in the reported research.<sup>6,54</sup> In addition, product accumulation might lead to altered solution pH and, thereby, affect product selectivity. Shifting the batch design to a flow reactor powered by a peristaltic pump, which can provide a continuous reactant supply, is necessary to the maintain stable production of the target product. Alternatively,

the microfluidic effect could be applied to the reactor design to enhance mass transfer and, thereby, improve selectivity. As shown in Fig. 3, other system parameters beyond photoelectrodes, such as substrate concentration, solution pH, temperature, applied potential, and substrate absorption model, also contribute to the performance of a PEC organic valorisation reaction. Research into the optimisation and investigation of its mechanism is also essential to maximise the efficiency of a PEC system. Additionally, a techno-economic analysis helps assess the technical feasibility of PEC organic waste valorisation.

In conclusion, PEC valorisation of organic waste could be a promising route for not only waste mitigation but also the cogeneration of value-added chemicals and solar fuels. However, research into cost-effective pretreatment processes and the maximisation of the operational efficiency of robust PEC systems in a manner that allows for scalability is required for a commercially viable technology. To meet this demand, research directions are suggested to focus on investigating cost-effective catalysts for polymer waste depolymerisation in neutral or near-neutral conditions, integrating rational design strategies for the existing state-of-the-art photoelectrodes, developing compatible co-catalysts that can target C<sub>2+</sub> products, and exploring novel photoelectrodes that meet high PEC performance and stability requirements. Additionally, integrating PEC oxidation with PEC reduction or cathodic reaction for value-added chemical production and advanced PEC reactor design could facilitate a circular carbon economy while addressing the energy crisis and environmental pollution.

## Data availability

No primary research results, software or code have been included and no new data were generated or analysed as part of this review.

## Author contributions

Fitri Nur Indah Sari: conceptualisation, investigation, writing – original draft (lead), review and editing. Ping-Chang Chuang: writing – original draft (supporting). Shih-Ching Huang: writing – original draft (supporting). Chia-Yu Lin: supervision and funding acquisition. Yi-Hsuan Lai: conceptualisation, investigation, writing – original draft (lead), review and editing, supervision and funding acquisition.

## Conflicts of interest

There are no conflicts to declare.

## Acknowledgements

Financial support from the National Science and Technology Council of Taiwan (NSTC 111-2221-E-006-019-MY3 and NSTC 113-2221-E-006-085-MY3) is gratefully acknowledged. The authors also acknowledge the support from the Hierarchical Green-Energy Materials (Hi-GEM) Research Center at National



Cheng Kung University by the Featured Areas Research Center Program within the framework of the Higher Education Sprout Project by the Ministry of Education in Taiwan.

## References

- 1 S. Bhattacharjee, S. Linley and E. Reisner, *Nat. Rev. Chem.*, 2024, **8**, 87–105.
- 2 K. de Kleijne, M. A. J. Huijbregts, F. Knobloch, R. van Zelm, J. P. Hilbers, H. de Coninck and S. V. Hanssen, *Nat. Energy*, 2024, **9**, 1139–1152.
- 3 H. Song, S. Luo, H. Huang, B. Deng and J. Ye, *ACS Energy Lett.*, 2022, **7**, 1043–1065.
- 4 P. Stegmann, V. Daioglou, M. Londo, D. P. van Vuuren and M. Junginger, *Nature*, 2022, **612**, 272–276.
- 5 S. Kaza, L. Yao, P. Bhada-Tata and F. Van Woerden, *What a Waste 2.0: A Global Snapshot of Solid Waste Management to 2050*, World Bank Publications, 2018.
- 6 Y. Yang and T. Mu, *Green Chem.*, 2021, **23**, 4228–4254.
- 7 Y.-H. Lai, P.-W. Yeh, M.-J. Jhong and P.-C. Chuang, *Chem. Eng. J.*, 2023, **475**, 146413.
- 8 T.-K. Liu, G. Y. Jang, S. Kim, K. Zhang, X. Zheng and J. H. Park, *Small Methods*, 2024, **8**, 2300315.
- 9 B. Zhang, H. Zhang, Y. Pan, J. Shao, X. Wang, Y. Jiang, X. Xu and S. Chu, *Chem. Eng. J.*, 2023, **462**, 142247.
- 10 T.-R. Ko, C.-Y. Lin and Y.-H. Lai, *Chem. Eng. J.*, 2022, **433**, 133607.
- 11 Q. Shi and H. Duan, *Chem. Catal.*, 2022, **2**, 3471–3496.
- 12 Y. Liu, C. W. S. Yeung and E. Reisner, *Energy Environ. Sci.*, 2025, DOI: [10.1039/D5EE00689A](https://doi.org/10.1039/D5EE00689A).
- 13 D. Sajwan, A. Sharma, M. Sharma and V. Krishnan, *ACS Catal.*, 2024, **14**, 4865–4926.
- 14 Alibaba product search: formic acid 85%, category: organic acid, min order: 1 metric ton, [https://www.alibaba.com/products/formic\\_acid\\_85%2525.html](https://www.alibaba.com/products/formic_acid_85%2525.html), accessed April, 2025.
- 15 A. Fujishima and K. Honda, *Nature*, 1972, **238**, 37–38.
- 16 B. M. Hunter, H. B. Gray and A. M. Müller, *Chem. Rev.*, 2016, **116**, 14120–14136.
- 17 M. G. Walter, E. L. Warren, J. R. McKone, S. W. Boettcher, Q. Mi, E. A. Santori and N. S. Lewis, *Chem. Rev.*, 2010, **110**, 6446–6473.
- 18 Y. Pan, H. Zhang, B. Zhang, F. Gong, J. Feng, H. Huang, S. Vanka, R. Fan, Q. Cao, M. Shen, Z. Li, Z. Zou, R. Xiao and S. Chu, *Nat. Commun.*, 2023, **14**, 1013.
- 19 S. Chen and L.-W. Wang, *Chem. Mater.*, 2012, **24**, 3659–3666.
- 20 J. R. McKone, N. S. Lewis and H. B. Gray, *Chem. Mater.*, 2014, **26**, 407–414.
- 21 M. Zhang, J. Wang, H. Xue, J. Zhang, S. Peng, X. Han, Y. Deng and W. Hu, *Angew. Chem. Int. Ed. Engl.*, 2020, **59**, 18463–18467.
- 22 L. Pan, J. H. Kim, M. T. Mayer, M.-K. Son, A. Ummadisingu, J. S. Lee, A. Hagfeldt, J. Luo and M. Grätzel, *Nat. Catal.*, 2018, **1**, 412–420.
- 23 L. Pan, Y. Liu, L. Yao, R. Dan, K. Sivula, M. Grätzel and A. Hagfeldt, *Nat. Commun.*, 2020, **11**, 318.
- 24 S. P. Berglund, F. F. Abdi, P. Bogdanoff, A. Chemseddine, D. Friedrich and R. van de Krol, *Chem. Mater.*, 2016, **28**, 4231–4242.
- 25 L. Qu, R. Tan, A. Sivanantham, M. J. Kang, Y. J. Jeong, D. H. Seo, S. Kim and I. S. Cho, *J. Energy Chem.*, 2022, **71**, 201–209.
- 26 C. Li, J. He, Y. Xiao, Y. Li and J.-J. Delaunay, *Energy Environ. Sci.*, 2020, **13**, 3269–3306.
- 27 Y. J. Jang, Y. B. Park, H. E. Kim, Y. H. Choi, S. H. Choi and J. S. Lee, *Chem. Mater.*, 2016, **28**, 6054–6061.
- 28 J. J. Roylance, T. W. Kim and K.-S. Choi, *ACS Catal.*, 2016, **6**, 1840–1847.
- 29 C. Y. Toe, C. Tsounis, J. Zhang, H. Masood, D. Gunawan, J. Scott and R. Amal, *Energy Environ. Sci.*, 2021, **14**, 1140–1175.
- 30 M. Ashraf, N. Ullah, I. Khan, W. Tremel, S. Ahmad and M. N. Tahir, *Chem. Rev.*, 2023, **123**, 4443–4509.
- 31 M. Han, S. Zhu, C. Xia and B. Yang, *Appl. Catal., B*, 2022, **316**, 121662.
- 32 T. Uekert, M. F. Kuehnel, D. W. Wakerley and E. Reisner, *Energy Environ. Sci.*, 2018, **11**, 2853–2857.
- 33 G. Wang, H. Wang, Y. Ling, Y. Tang, X. Yang, R. C. Fitzmorris, C. Wang, J. Z. Zhang and Y. Li, *Nano Lett.*, 2011, **11**, 3026–3033.
- 34 X. Yan, K. Sakai and H. Ozawa, *ACS Catal.*, 2023, **13**, 13456–13465.
- 35 T. Zhou, J. Wang, S. Chen, J. Bai, J. Li, Y. Zhang, L. Li, L. Xia, M. Rahim, Q. Xu and B. Zhou, *Appl. Catal., B*, 2020, **267**, 118599.
- 36 L. Li, H. Shi, H. Yu, X. Tan, Y. Wang, S. Ge, A. Wang, K. Cui, L. Zhang and J. Yu, *Appl. Catal., B*, 2021, **292**, 120184.
- 37 S. Cao, X. Yan, Z. Kang, Q. Liang, X. Liao and Y. Zhang, *Nano Energy*, 2016, **24**, 25–31.
- 38 Y. Pihosh, I. Turkevych, K. Mawatari, T. Asai, T. Hisatomi, J. Uemura, M. Tosa, K. Shimamura, J. Kubota, K. Domen and T. Kitamori, *Small*, 2014, **10**, 3692–3699.
- 39 J. Liu, J. Li, Y. Li, J. Guo, S.-M. Xu, R. Zhang and M. Shao, *Appl. Catal., B*, 2020, **278**, 119268.
- 40 Y. Li, Q. Mei, Z. Liu, X. Hu, Z. Zhou, J. Huang, B. Bai, H. Liu, F. Ding and Q. Wang, *Appl. Catal., B*, 2022, **304**, 120995.
- 41 M. Ma, K. Zhang, P. Li, M. S. Jung, M. J. Jeong and J. H. Park, *Angew. Chem. Int. Ed. Engl.*, 2016, **55**, 11819–11823.
- 42 M. B. Costa, M. A. de Araújo, M. V. d. L. Tinoco, J. F. d. Brito and L. H. Mascaro, *J. Energy Chem.*, 2022, **73**, 88–113.
- 43 C. Loka, D. Gelija, S. V. P. Vattikuti and K.-S. Lee, *ACS Sustain. Chem. Eng.*, 2023, **11**, 11978–11990.
- 44 Y. Li, Q. Wu, Y. Chen, R. Zhang, C. Li, K. Zhang, M. Li, Y. Lin, D. Wang, X. Zou and T. Xie, *Appl. Catal., B*, 2021, **290**, 120058.
- 45 Z.-Y. Wang, H.-M. Li, S.-S. Yi, M.-Z. You, H.-J. Jing, X.-Z. Yue, Z.-T. Zhang and D.-L. Chen, *Appl. Catal., B*, 2021, **297**, 120406.
- 46 L. Liccardo, E. Lushaj, L. Dal Compare, E. Moretti and A. Vomiero, *Small Sci.*, 2022, **2**, 2100104.
- 47 J. Schneidewind, *Adv. Energy Mater.*, 2022, **12**, 2200342.
- 48 M. E. Aguirre, R. Zhou, A. J. Eugene, M. I. Guzman and M. A. Grela, *Appl. Catal., B*, 2017, **217**, 485–493.



49 C.-Y. Lin, Y.-H. Lai, D. Mersch and E. Reisner, *Chem. Sci.*, 2012, **3**, 3482–3487.

50 D. S. Kim, S. Y. Oh, H. H. Lee and H. K. Cho, *Adv. Energy Mater.*, 2024, **14**, 2304239.

51 Y. Liu, H. Tan, Y. Wei, M. Liu, J. Hong, W. Gao, S. Zhao, S. Zhang and S. Guo, *ACS Nano*, 2023, **17**, 5994–6001.

52 R. S. Lillard, G. S. Kanner and D. P. Butt, *J. Electrochem. Soc.*, 1998, **145**, 2718.

53 Y.-H. Lai, Y.-J. Lai, C.-Y. Yen and P.-C. Chuang, *Sustainable Energy Fuels*, 2020, **4**, 5005–5008.

54 P.-C. Chuang, C.-Y. Lin, S.-T. Ye and Y.-H. Lai, *Small*, 2024, **20**, 2404478.

55 Y.-H. Wu, D. A. Kuznetsov, N. C. Pflug, A. Fedorov and C. R. Müller, *J. Mater. Chem. A*, 2021, **9**, 6252–6260.

56 L. Luo, W. Chen, S.-M. Xu, J. Yang, M. Li, H. Zhou, M. Xu, M. Shao, X. Kong, Z. Li and H. Duan, *J. Am. Chem. Soc.*, 2022, **144**, 7720–7730.

57 W. Septina and S. D. Tilley, *Curr. Opin. Electrochem.*, 2017, **2**, 120–127.

58 I. Roger, M. A. Shipman and M. D. Symes, *Nat. Rev. Chem.*, 2017, **1**, 0003.

59 K. S. Egorova and V. P. Ananikov, *Angew. Chem., Int. Ed.*, 2016, **55**, 12150–12162.

60 K. M. P. Wheelhouse, R. L. Webster and G. L. Beutner, *Org. Process Res. Dev.*, 2023, **27**, 1157–1159.

61 R. M. Bullock, *Science*, 2013, **342**, 1054–1055.

62 G. Gunn, in *Critical Metals Handbook*, 2014, pp. 284–311, DOI: [10.1002/9781118755341.ch12](https://doi.org/10.1002/9781118755341.ch12).

63 Q. Shi, J. Li, Y. Liu, K. Kong, A.-Z. Li and H. Duan, *ACS Catal.*, 2024, **14**, 10728–10736.

64 N. Le Duy, P.-C. Chuang, C.-Y. Lin and Y.-H. Lai, *J. Photochem. Photobiol., A*, 2025, **458**, 115932.

65 H. Tateno, S. Iguchi, Y. Miseki and K. Sayama, *Angew. Chem., Int. Ed.*, 2018, **57**, 11238–11241.

66 J. Yu, J. González-Cobos, F. Dappozze, F. J. López-Tenllado, J. Hidalgo-Carrillo, A. Marinas, P. Vernoux, A. Caravaca and C. Guillard, *Appl. Catal., B*, 2022, **318**, 121843.

67 C. R. Lhermitte, N. Plainpan, P. Canjura, F. Boudoire and K. Sivula, *RSC Adv.*, 2021, **11**, 198–202.

68 C.-C. Wu, T.-G. Vo, M. B. Sullivan, K. P. Ong, H. Jin, A. Chuang, M.-T. Huynh Pham and C.-Y. Chiang, *Inorg. Chem.*, 2025, **64**, 1579–1586.

69 J. Ouyang, X. Liu, B.-H. Wang, J.-B. Pan, S. Shen, L. Chen, C.-T. Au and S.-F. Yin, *ACS Appl. Mater. Interfaces*, 2022, **14**, 23536–23545.

70 H. G. Cha and K.-S. Choi, *Nat. Chem.*, 2015, **7**, 328–333.

71 D. Wang, S. H. Lee, S. Han, J. Kim, N. V. T. Trang, K. Kim, E.-G. Choi, P. Boonmongkolras, Y. W. Lee, B. Shin, Y. H. Kim and C. B. Park, *Green Chem.*, 2020, **22**, 5151–5160.

72 T. Li, J. Y. Mo, D. M. Weekes, K. E. Dettelbach, R. P. Jansonius, G. M. Sammis and C. P. Berlinguette, *ChemSusChem*, 2020, **13**, 3622–3626.

73 S. Li, F. Chen, T. Ma and H. Huang, *Chem. Eng. J.*, 2023, **467**, 143421.

74 C. Lin, C. Dong, S. Kim, Y. Lu, Y. Wang, Z. Yu, Y. Gu, Z. Gu, D. K. Lee, K. Zhang and J. H. Park, *Adv. Mater.*, 2023, **35**, 2209955.

75 D. Liu, J.-C. Liu, W. Cai, J. Ma, H. B. Yang, H. Xiao, J. Li, Y. Xiong, Y. Huang and B. Liu, *Nat. Commun.*, 2019, **10**, 1779.

76 L.-W. Huang, T.-G. Vo and C.-Y. Chiang, *Electrochim. Acta*, 2019, **322**, 134725.

77 I. Grigioni, A. Polo, C. Nomellini, L. Vigni, A. Poma, M. V. Dozzi and E. Sell, *ACS Appl. Energy Mater.*, 2023, **6**, 10020–10029.

78 C. M. Tian, M. Jiang, D. Tang, L. Qiao, H. Y. Xiao, F. E. Oropeza, J. P. Hofmann, E. J. M. Hensen, A. Tadich, W. Li, D. C. Qi and K. H. L. Zhang, *J. Mater. Chem. A*, 2019, **7**, 11895–11907.

79 C. R. Lhermitte and B. M. Bartlett, *Acc. Chem. Res.*, 2016, **49**, 1121–1129.

80 L. Wang, X. Zhou, N. T. Nguyen, I. Hwang and P. Schmuki, *Adv. Mater.*, 2016, **28**, 2432–2438.

81 Y. Li, T. Takata, D. Cha, K. Takanabe, T. Minegishi, J. Kubota and K. Domen, *Adv. Mater.*, 2013, **25**, 125–131.

82 C. Feng, Z. Liu, H. Ju, A. Mavrić, M. Valant, J. Fu, B. Zhang and Y. Li, *Nat. Commun.*, 2024, **15**, 6436.

83 M. J. Kenney, M. Gong, Y. Li, J. Z. Wu, J. Feng, M. Lanza and H. Dai, *Science*, 2013, **342**, 836–840.

84 J. Kegel, I. M. Povey and M. E. Pemble, *Nano Energy*, 2018, **54**, 409–428.

85 Y.-H. Lai, K.-C. Lin, C.-Y. Yen and B.-J. Jiang, *Faraday Discuss.*, 2019, **215**, 297–312.

86 C.-Y. Lin, S.-Y. Lin, M.-C. Tsai and C.-H. Wu, *Sustainable Energy Fuels*, 2020, **4**, 625–632.

87 O. C. Olatunde, W. Lei, H. Ferjani and D. C. Onwudiwe, *Mater. Today Sustain.*, 2024, **26**, 100747.

88 J. E. Yourey and B. M. Bartlett, *J. Mater. Chem. A*, 2011, **21**, 7651–7660.

89 J. E. Yourey, K. J. Pyper, J. B. Kurtz and B. M. Bartlett, *J. Phys. Chem. C*, 2013, **117**, 8708–8718.

90 R. H. Coridan, A. C. Nielander, S. A. Francis, M. T. McDowell, V. Dix, S. M. Chatman and N. S. Lewis, *Energy Environ. Sci.*, 2015, **8**, 2886–2901.

91 H. Zhou, Y. Ren, Z. Li, M. Xu, Y. Wang, R. Ge, X. Kong, L. Zheng and H. Duan, *Nat. Commun.*, 2021, **12**, 4679.

92 F. Kang, Q. Wang, D. Du, L. Wu, D. W. F. Cheung and J. Luo, *Angew. Chem., Int. Ed.*, 2025, **64**, e202417648.

93 I. Holmes-Gentle, F. E. Bedoya-Lora, L. Aimone and S. Haussener, *J. Mater. Chem. A*, 2023, **11**, 23895–23908.

94 C. Pornrungroj, V. Andrei and E. Reisner, *J. Am. Chem. Soc.*, 2023, **145**, 13709–13714.

95 Á. Balog, E. Kecsenovity, G. F. Samu, J. He, D. Fekete and C. Janáky, *Nat. Catal.*, 2024, **7**, 522–535.

96 F. Le Formal, E. Pastor, S. D. Tilley, C. A. Mesa, S. R. Pendlebury, M. Grätzel and J. R. Durrant, *J. Am. Chem. Soc.*, 2015, **137**, 6629–6637.

97 Y. Zhang, H. Zhang, A. Liu, C. Chen, W. Song and J. Zhao, *J. Am. Chem. Soc.*, 2018, **140**, 3264–3269.

98 C. A. Mesa, L. Francàs, K. R. Yang, P. Garrido-Barros, E. Pastor, Y. Ma, A. Kafizas, T. E. Rosser, M. T. Mayer, E. Reisner, M. Grätzel, V. S. Batista and J. R. Durrant, *Nat. Chem.*, 2020, **12**, 82–89.



99 C. A. Mesa, A. Kafizas, L. Francàs, S. R. Pendlebury, E. Pastor, Y. Ma, F. Le Formal, M. T. Mayer, M. Grätzel and J. R. Durrant, *J. Am. Chem. Soc.*, 2017, **139**, 11537–11543.

100 J. Yuan, Y. Yuan, J. Zhang, H. Xu, Z. Mao and Y. Ma, *ChemSusChem*, 2022, **15**, e202102313.

101 Z. Ma, X. Guo, Y. Yuan, Y. Wu, Y. Hai, J. Wu, W. Wu and Y. Ma, *J. Catal.*, 2024, **437**, 115661.

102 M. S. Martí Molera, C. Fàbrega and T. Andreu, *J. Electrochem. Soc.*, 2024, **171**, 086503.

103 Y. Kageshima, H. Wada, K. Teshima and H. Nishikiori, *Appl. Catal., B*, 2023, **327**, 122431.

104 Y. Lu, T.-K. Liu, C. Lin, K. H. Kim, E. Kim, Y. Yang, X. Fan, K. Zhang and J. H. Park, *Nano Lett.*, 2024, **24**, 4633–4640.

105 Y. Liu, M. Wang, B. Zhang, D. Yan and X. Xiang, *ACS Catal.*, 2022, **12**, 6946–6957.

106 C.-Y. Lin, S.-C. Huang, Y.-G. Lin, L.-C. Hsu and C.-T. Yi, *Appl. Catal., B*, 2021, **296**, 120351.

107 K. Jakubow-Piotrowska, B. Witkowski and J. Augustynski, *Commun. Chem.*, 2022, **5**, 125.

108 J. Ma, K. Mao, J. Low, Z. Wang, D. Xi, W. Zhang, H. Ju, Z. Qi, R. Long, X. Wu, L. Song and Y. Xiong, *Angew. Chem., Int. Ed.*, 2021, **60**, 9357–9361.

109 Z. Gu, X. An, R. Liu, L. Xiong, J. Tang, C. Hu, H. Liu and J. Qu, *Appl. Catal., B*, 2021, **282**, 119541.

110 F. Kong, H. Zhou, Z. Chen, Z. Dou and M. Wang, *Angew. Chem., Int. Ed.*, 2022, **61**, e202210745.

111 F. Kang, Q. Wang, D. Du, L. Wu, D. W. F. Cheung and J. Luo, *Angew. Chem. Int. Ed. Engl.*, 2025, **64**, e202417648.

112 H. Tateno, S.-Y. Chen, Y. Miseki, T. Nakajima, T. Mochizuki and K. Sayama, *ACS Sustain. Chem. Eng.*, 2022, **10**, 7586–7594.

113 Y. Lu, B. G. Lee, C. Lin, T.-K. Liu, Z. Wang, J. Miao, S. H. Oh, K. C. Kim, K. Zhang and J. H. Park, *Nat. Commun.*, 2024, **15**, 5475.

114 T.-G. Vo, C.-C. Kao, J.-L. Kuo, C.-c. Chiu and C.-Y. Chiang, *Appl. Catal., B*, 2020, **278**, 119303.

115 Z. Wu, K. Ren, J. Zhou, Y. Zhang and L. Qi, *Adv. Funct. Mater.*, 2025, **35**, 2418294.

116 M. Tayebi, Z. Masoumi, A. Tayyebi, J.-H. Kim, H. Lee, B. Seo, C.-S. Lim and H.-G. Kim, *ACS Appl. Mater. Interfaces*, 2023, **15**, 20053–20063.

117 S. Kim, D. Oh and J.-W. Jang, *Nano Lett.*, 2024, **24**, 5146–5153.

118 X. Li, J. Wang, T. Zhang, T. Wang and Y. Zhao, *ACS Sustain. Chem. Eng.*, 2022, **10**, 9546–9552.

119 P.-C. Chuang and Y.-H. Lai, *Catal. Sci. Technol.*, 2022, **12**, 6375–6383.

120 H. Zhao, X. Zhao, J. Zhang, S. Anandita, W. Liu, S. W. Koh, S. Yu, C. Li, Z. Chen, R. Xu, Z. Zou, W. Tu and H. Li, *Adv. Energy Mater.*, 2024, **14**, 2400037.

121 L. L. Nascimento, J. Z. Marinho, A. L. R. dos Santos, A. M. de Faria, R. A. C. Souza, C. Wang and A. O. T. Patrocínio, *Appl. Catal., A*, 2022, **646**, 118867.

122 Q. Wang, X. Ma, P. Wu, B. Li, L. Zhang and J. Shi, *Nano Energy*, 2021, **89**, 106326.

123 F. W. S. Lucas, R. G. Grim, S. A. Tacey, C. A. Downes, J. Hasse, A. M. Roman, C. A. Farberow, J. A. Schaidle and A. Holewinski, *ACS Energy Lett.*, 2021, **6**, 1205–1270.

124 E. J. Cho, L. T. P. Trinh, Y. Song, Y. G. Lee and H.-J. Bae, *Bioresour. Technol.*, 2020, **298**, 122386.

125 A. Yousuf, *Waste Manage.*, 2012, **32**, 2061–2067.

126 S. Paul and A. Dutta, *Resour., Conserv. Recycl.*, 2018, **130**, 164–174.

127 D. Klemm, B. Heublein, H.-P. Fink and A. Bohn, *Angew. Chem., Int. Ed.*, 2005, **44**, 3358–3393.

128 S.-J. Jung, S.-H. Kim and I.-M. Chung, *Biomass Bioenergy*, 2015, **83**, 322–327.

129 O. Lanzalunga and M. Bietti, *J. Photochem. Photobiol., B*, 2000, **56**, 85–108.

130 <https://plasticseurope.org/knowledge-hub/plastics-the-facts-2022-2/>, 2022.

131 R. Geyer, J. R. Jambeck and K. L. Law, *Sci. Adv.*, 2017, **3**, e1700782.

132 T. Uekert, C. M. Pichler, T. Schubert and E. Reisner, *Nat. Sustain.*, 2021, **4**, 383–391.

133 A. W. Bhutto, K. Qureshi, K. Harijan, R. Abro, T. Abbas, A. A. Bazmi, S. Karim and G. Yu, *Energy*, 2017, **122**, 724–745.

134 Y. You, S. Chen, J. Zhao, J. Lin, D. Wen, P. Sha, L. Li, D. Bu and S. Huang, *Adv. Mater.*, 2024, **36**, 2307962.

135 T. Uekert, H. Kasap and E. Reisner, *J. Am. Chem. Soc.*, 2019, **141**, 15201–15210.

136 M. Du, Y. Zhang, S. Kang, X. Guo, Y. Ma, M. Xing, Y. Zhu, Y. Chai and B. Qiu, *ACS Catal.*, 2022, **12**, 12823–12832.

137 M. Li and S. Zhang, *ACS Catal.*, 2024, **14**, 2949–2958.

138 E. Lam and E. Reisner, *Angew. Chem. Int. Ed. Engl.*, 2021, **60**, 23306–23312.

139 S. Linley and E. Reisner, *Adv. Sci.*, 2023, **10**, 2207314.

140 E. Lam, M. Miller, S. Linley, R. R. Manuel, I. A. C. Pereira and E. Reisner, *Angew. Chem. Int. Ed. Engl.*, 2023, **62**, e202215894.

141 S. Bhattacharjee, C. Guo, E. Lam, J. M. Holstein, M. Rangel Pereira, C. M. Pichler, C. Pornrungroj, M. Rahaman, T. Uekert, F. Hollfelder and E. Reisner, *J. Am. Chem. Soc.*, 2023, **145**, 20355–20364.

142 D. K. Zhong, S. Choi and D. R. Gamelin, *J. Am. Chem. Soc.*, 2011, **133**, 18370–18377.

143 M. Z. Rahman, T. Edvinsson and J. Gascon, *Nat. Rev. Chem.*, 2022, **6**, 243–258.

144 J. Wang, X. Li, T. Zhang, X. Qian, T. Wang and Y. Zhao, *Appl. Catal., B*, 2023, **332**, 122744.

145 F. Amano, M. Nakata, A. Yamamoto and T. Tanaka, *J. Phys. Chem. C*, 2016, **120**, 6467–6474.

146 J. Kim, J. Jang, T. Hilberath, F. Hollmann and C. B. Park, *Nat. Synth.*, 2022, **1**, 776–786.

147 H. Zhao, C.-F. Li, L.-Y. Liu, B. Palma, Z.-Y. Hu, S. Renneckar, S. Larter, Y. Li, M. G. Kibria, J. Hu and B.-L. Su, *J. Colloid Interface Sci.*, 2021, **585**, 694–704.

148 S. Guo, Y. Huang, D. Li, Z. Xie, Y. Jia, X. Wu, D. Xu and W. Shi, *Chem. Commun.*, 2023, **59**, 7791–7794.

149 J. Low, J. Yu, M. Jaroniec, S. Wageh and A. A. Al-Ghamdi, *Adv. Mater.*, 2017, **29**, 1601694.



150 S. Li, W. Xu, L. Meng, W. Tian and L. Li, *Small Sci.*, 2022, **2**, 2100112.

151 H. Zhou, Z. Li, L. Ma and H. Duan, *Chem. Commun.*, 2022, **58**, 897–907.

152 A. J. Bard, *J. Am. Chem. Soc.*, 2010, **132**, 7559–7567.

153 J. Ran, J. Zhang, J. Yu, M. Jaroniec and S. Z. Qiao, *Chem. Soc. Rev.*, 2014, **43**, 7787–7812.

154 S.-C. Huang, C.-C. Cheng, Y.-H. Lai and C.-Y. Lin, *Chem. Eng. J.*, 2020, **395**, 125176.

155 M. Ko, L. T. M. Pham, Y. J. Sa, J. Woo, T. V. T. Nguyen, J. H. Kim, D. Oh, P. Sharma, J. Ryu, T. J. Shin, S. H. Joo, Y. H. Kim and J.-W. Jang, *Nat. Commun.*, 2019, **10**, 5123.

156 H. Zhang, Y. Zhao, H. Zhang, H. Zhou, H. Wang, X. Zong, H. Yin and C. Li, *Appl. Catal., B*, 2020, **265**, 118558.

157 S. Bhattacharjee, V. Andrei, C. Pornrungroj, M. Rahaman, C. M. Pichler and E. Reisner, *Adv. Funct. Mater.*, 2022, **32**, 2109313.

158 S. Bhattacharjee, M. Rahaman, V. Andrei, M. Miller, S. Rodríguez-Jiménez, E. Lam, C. Pornrungroj and E. Reisner, *Nat. Synth.*, 2023, **2**, 182–192.

159 A. Tayyebi, R. Mehrotra, M. A. Mubarok, J. Kim, M. Zafari, M. Tayyebi, D. Oh, S.-h. Lee, J. E. Matthews, S.-W. Lee, T. J. Shin, G. Lee, T. F. Jaramillo, S.-Y. Jang and J.-W. Jang, *Nat. Catal.*, 2024, **7**, 510–521.

160 P. Bornoz, F. F. Abdi, S. D. Tilley, B. Dam, R. van de Krol, M. Graetzel and K. Sivula, *J. Phys. Chem. C*, 2014, **118**, 16959–16966.

161 R. Liu, Z. Zheng, J. Spurgeon and X. Yang, *Energy Environ. Sci.*, 2014, **7**, 2504–2517.

162 D. Si, B. Xiong, L. Chen and J. Shi, *Chem Catal.*, 2021, **1**, 941–955.

163 X. Liu, X. He, D. Xiong, G. Wang, Z. Tu, D. Wu, J. Wang, J. Gu and Z. Chen, *ACS Catal.*, 2024, **14**, 5366–5376.

164 G. Yang, Y. Jiao, H. Yan, Y. Xie, C. Tian, A. Wu, Y. Wang and H. Fu, *Nat. Commun.*, 2022, **13**, 3125.

165 S. A. Akhade, N. Singh, O. Y. Gutiérrez, J. Lopez-Ruiz, H. Wang, J. D. Holladay, Y. Liu, A. Karkamkar, R. S. Weber, A. B. Padmaperuma, M.-S. Lee, G. A. Whyatt, M. Elliott, J. E. Holladay, J. L. Male, J. A. Lercher, R. Rousseau and V.-A. Glezakou, *Chem. Rev.*, 2020, **120**, 11370–11419.

166 M. Zhang, Z. Zheng, X. Zhang, Z. Jiang, X. Yong, K. Li, X. Tu and K. Yan, *JACS Au*, 2025, **5**, 937–947.

167 L. Xiao, W. Dai, S. Mou, X. Wang, Q. Cheng and F. Dong, *Energy Environ. Sci.*, 2023, **16**, 2696–2704.

168 A. Chaturvedi, S. Gaber, S. Kaur, K. C. Ranjeesh, T. C. Nagaiah and D. Shetty, *ACS Energy Lett.*, 2024, **9**, 2484–2491.

169 Y. Goto, T. Hisatomi, Q. Wang, T. Higashi, K. Ishikiriyama, T. Maeda, Y. Sakata, S. Okunaka, H. Tokudome, M. Katayama, S. Akiyama, H. Nishiyama, Y. Inoue, T. Takewaki, T. Setoyama, T. Minegishi, T. Takata, T. Yamada and K. Domen, *Joule*, 2018, **2**, 509–520.

170 A. Vilanova, P. Dias, T. Lopes and A. Mendes, *Chem. Soc. Rev.*, 2024, **53**, 2388–2434.

171 V. Andrei, Y.-H. Chiang, M. Rahaman, M. Anaya, T. Kang, E. Ruggeri, S. D. Stranks and E. Reisner, *Energy Environ. Sci.*, 2025, **18**, 3623–3632.

172 T. Hisatomi, Q. Wang, F. Zhang, S. Ardo, E. Reisner, H. Nishiyama, A. Kudo, T. Yamada and K. Domen, *Front. Sci. Energy Storage Mater.*, 2024, **2**, 1411644.

173 I. Y. Ahmet, Y. Ma, J.-W. Jang, T. Henschel, B. Stannowski, T. Lopes, A. Vilanova, A. Mendes, F. F. Abdi and R. van de Krol, *Sustainable Energy Fuels*, 2019, **3**, 2366–2379.

174 A. Vilanova, T. Lopes, C. Spenke, M. Wullenkord and A. Mendes, *Energy Storage Mater.*, 2018, **13**, 175–188.

